Advancing Applications of IMUs in Sports Training and Biomechanics

by

Ryan S. McGinnis

A dissertation submitted in partial fulfillment
of the requirements for the degree of
Doctor of Philosophy
(Mechanical Engineering)
in the University of Michigan
2013

Doctoral Committee:

Professor Noel C. Perkins, Chair
Professor James A. Ashton-Miller
Professor Mont Hubbard, University of California, Davis
Professor Arthur D. Kuo
Assistant Professor Scott G. McLean

Dedication

To my parents and my wife.

Acknowledgements

This dissertation could not have been completed without the assistance of many people. Unfortunately, I am only able to thank some of them here. I begin, rightly, with my advisor Noel Perkins. This work would not have been possible without his unyielding support and friendship. His guidance and insight has helped to shape this dissertation, my development as a researcher, and my future career aspirations. I can't possibly put into words everything his support has meant to me, but he should know that I am truly thankful.

As with my advisor, it is important that I thank my dissertation committee. Professors James Ashton-Miller, Art Kuo, and Scott Mclean of the University of Michigan and Professor Mont Hubbard of UC Davis have helped to shape the direction and scope of this dissertation. Their probing questions and frank comments have helped to improve my work and the way I think as a researcher. Thank you all for your support and guidance.

Beyond these select individuals, I must also thank the National Science Foundation Graduate Research Fellowship Program and the University of Michigan department of mechanical engineering for providing funding for my graduate studies and this work.

Each of the studies included in this dissertation have required help from a number of individuals either through use of their equipment, dedication of their time, or advice in their areas of expertise. Along these lines, I specifically would like to thank my lab mates Kevin King, Steve Cain, Jessandra Hough, and Andy Hirsch for helping me develop my understanding of IMU technology and some of its possible applications. I've also noted individual contributions as well as additional sources of funding for each chapter below. In the likely event that I missed someone below, I am sorry, and know that I am truly thankful.

Chapter 2:

Thanks to Professors Kathleen Sienko and Scott McLean for providing access to their motion capture systems. Thanks are also due to Brian Orr for providing insight into metrics useful for baseball pitching coaches as well as to Brian Yost and Marggie Otero for acting as subjects for this study. Additional thanks are due to Steve Cain, Jessandra Hough, and Ramiro Pinon for help in collecting motion capture data.

Chapter 3:

I gratefully acknowledge past support from the University of Michigan Graduate Medical Education Innovations Fund and from Ebonite International for the development of the wireless IMU used in this study. Many thanks are also due to Peter Curran for manufacturing the experimental rigid body.

Chapter 4:

I extend my sincerest thanks to Steve Davidson and Grant Goulet for their aid in collecting/processing the motion capture data for this study, and to the University of Michigan Bone and Joint Injury Prevention and Rehabilitation Center for providing access to its motion capture laboratory.

Chapter 5:

Thanks to Jessandra Hough for the design and manufacturing of the double pendulum considered in this experiment. Thanks are also due to Art Kuo for his critical analysis of this work. His questions helped to shape its focus.

Chapter 6:

I sincerely thank James Ashton-Miller for his insightful comments throughout the duration of this work.

Beyond these specific contributions to the research, I must thank those who have helped with my mental health during my PhD studies. I have been lucky to share my moments away from the lab with some amazing friends and family. I would like to thank

you all for helping me maintain sanity during this process. I won't name you all here, but thank you for memorable times spent in NC, VT, and especially in MI camping at Dead Bear Dunes, Cabrewing down the Huron River, playing pool at Circus, and eating pizza with double mushrooms.

I would also like to thank Detroit Yoga, the Bull Schlitz of the Ann Arbor Ice Cube's men's B hockey league, the Red Lighter's of the Arctic Coliseum's men's B hockey league, and the NCRB for providing a legitimate excuse to take a break from work and get some exercise.

Thanks are most certainly due to my parents. Their tireless support of my goals has helped motivate me from a young age and has ultimate led to the completion of this dissertation. Despite your best wishes, it looks like I followed in your footsteps and became an engineer☺

Finally, I thank my wife. This would not have been possible without you. You're the best.

Table of Contents

Dedication ..... **ii**

Acknowledgements ..... **iii**

List of Figures ..... **viii**

List of Tables ..... **xii**

Abstract ..... **xiv**

Chapter 1: Introduction **1**

1.1. Motivation 1

1.2. Methods for Quantifying Human Motion 1

1.3. Research Objective and Scope 3

1.3.1. Chapter 2: Dynamics of Pitched Baseballs and Softballs Revealed via Ball-Embedded IMU. 4

1.3.2. Chapter 3: Rotational Dynamics and Stability of Rigid Bodies in Free-Flight 5

1.3.3. Chapter 4: The Velocity of a Running Athlete 6

1.3.4. Chapter 5: Joint Reactions Deduced from IMU Data 7

1.3.5. Chapter 6: Accurate Estimation of Joint Centers 8

Chapter 2: Dynamics of Pitched Baseballs and Softballs Revealed via Ball-Embedded IMU **10**

2.1. Introduction 10

2.2. Sensor Design and Experimental Methods 12

2.3. Results and Discussion 19

2.4. Conclusions/Outlook 24

Chapter 3: Rotational Dynamics and Stability of Rigid Bodies in Free-Flight **25**

3.1. Introduction 25

3.2. Methods 28

3.2.1. Wireless IMU and Experimental Procedure 28

3.2.2. Classical Analysis of Rigid Body Rotation during Free-Flight 31

3.3. Results and Discussion 33

3.3.1. Comparison of Experimental versus Predicted Rigid Body Rotation 34
3.3.2. Angular Velocity Reconstructed from a Single Tri-axial Accelerometer 41
3.4. Summary and Conclusions 46
Chapter 4: The Velocity of a Running Athlete 48
4.1. Introduction 48
4.2. Methods 49
4.3. Results and Discussion 56
4.4. Conclusions 61
4.5. Appendix 62
Chapter 5: Joint Reactions Deduced from IMU Data 64
5.1. Introduction 64
5.2. Methods 66
5.3. Results and Discussion 73
5.3.1. IMU Data and Link Orientation 74
5.3.2. IMU-Derived Estimates of Joint Reactions 76
5.3.3. Sensitivity of Joint Reactions to Mass Center Location 80
5.4. Conclusion 84
5.5. Appendix 85
Chapter 6: Accurate Estimation of Joint Centers 86
6.1. Introduction 86
6.2. Methods 88
6.3. Results & Discussion 93
6.3.1. Ideal Joint Behavior 93
6.3.2. Simulated Soft-Tissue Effects 95
Chapter 7: Contributions, Conclusions and Future Directions 100
7.1. Contributions and Conclusions 100
7.2. Limitations and Future Directions 102
References 105

List of Figures

Figure 2.1: Highly miniaturized wireless IMU design used in this study was approximately the size of a quarter. The IMU provides three-axis sensing of acceleration and angular velocity with wireless data transmission to a host computer. 12

Figure 2.2: (a) The miniaturized IMU shown as it would be embedded in a baseball. (b) Final version of the ball including a small jack (switch/recharging) which is removed prior to the throw. 13

Figure 2.3: (a) Magnitude of acceleration as measured by the embedded IMU during a representative softball pitch. Major phases of the throwing motion are labeled 1–5. (b) Flow chart of major steps to calculate ball-center velocity during the throw..... 15

Figure 2.4: (a) Ball-fixed reference frame with origin at the center of the accelerometer (*P*). (b) Field-fixed reference frame with origin at location of the ball center in tee (*O*) at the start of the trial. 16

Figure 2.5: (a) Uncorrected and (b) Corrected ball-center velocity (m/s) components as determined by IMU (thick) and motion capture (thin) data for a representative softball pitch..... 20

Figure 2.6: Linear (blue arrow denoted V) and angular (green arrow denoted W) velocity directions, and ball orientation at release for four typical baseball pitches: (a) fastball (four seam), (b) changeup, (c) curveball, and (d) slider. 23

Figure 3.1: Photographs of highly miniaturized, wireless IMU. (a) analog circuit side with MEMS angular rate gyros and accelerometer, (b) digital circuit side with microprocessor, wireless transceiver, surface mount antenna, and connectors for battery power and firmware programming. 28

Figure 3.2: Photograph of example rigid body employed in experiments..... 30

Figure 3.3: Example time histories of the measured (a) magnitude of the acceleration of point P, (b) magnitude of the angular velocity, (c) the rotational kinetic energy, and (d) magnitude of angular momentum about center of mass. The throw, free-flight and catch phases are noted. Example trial for rotation initiated nearly about minor axis. 35

Figure 3.4: Measured (solid) and calculated (dashed) angular velocity vector magnitude (black) and components for rotations initiated about the major (a), intermediate (b), and

minor (c) axes. The blue, green, and red curves correspond to components about the major (ω_1), intermediate (ω_2), and minor axes (ω_3), respectively. 37

Figure 3.5: Experimental demonstration of the polhode for rotations initiated close to the major (a), intermediate (b), and minor (c) principal axes. The measured angular velocity during the entire free-flight phase (black, scale in deg/s), closely follows the polhode defined by the intersection of the ellipsoids. 39

Figure 3.6: Measured (solid) and reconstructed (dashed) angular velocity magnitude (black) and components for rotations initiated nearly about the major (a), intermediate (b), and minor (c) axes. The blue, green, and red curves correspond to components about the major (ω_1), intermediate (ω_2), and minor axes (ω_3), respectively. 45

Figure 4.1: MOCAP marker trajectory during a straight-line running trial (A) and a zig-zag running trial (B). 50

Figure 4.2: (A) The IMU (YEI 3-space) is held against the lumbar portion of the subject's spine by a tension strap. A maker mounted to the IMU casing is simultaneously employed for MOCAP measurements. (B) The filtered components of acceleration measured by the IMU over two periods of motion during an example "Run" trial. Components: $\hat{e}_1$=blue, $\hat{e}_2$=green, and $\hat{e}_3$=red. 51

Figure 4.3: (A) Uncorrected velocity components ($\hat{E}_1$=blue, $\hat{E}_2$=green, $\hat{E}_3$=red) determined from IMU data (solid curves) and their respective drift error correction functions (dotted curves) for an example "Walk" trial with four identified velocity updates ($q=4$). (B) Corrected velocity components ($\hat{E}_1$=blue, $\hat{E}_2$=green, $\hat{E}_3$=red) determined from IMU data. The start and end times of the motion period are labeled t_s and t_e, respectively. The four intervening times when the torso velocity is close to zero ($q=4$) are labeled t_1, t_2, t_3 and t_4. 57

Figure 4.4: (A) IMU (blue) and MOCAP (red) horizontal speed as functions of time during the example walking trial over two motion periods. The correlation plot (B) also includes a best fit line to the data (red) and a line with unit slope (black). 58

Figure 4.5: (A) RMSE and (B) correlation coefficient (r) between IMU and MOCAP estimated speed versus integration time. RMSE increases and r decreases with integration time. 60

Figure 5.1: Schematic of the instrumented double pendulum with definitions of reference frames defined. Refer also to photograph shown in Fig. 1 of [105]. 67

Figure 5.2: Free body diagrams for the bottom (A) and top (B) link of the double pendulum. 69

Figure 5.3: IMU acceleration (A) and angular velocity (B) history for an example trial sampled from the bottom link IMU. The pendulum begins at rest in its stable equilibrium position ($t < t_1$), is perturbed from this position by hand ($t_1 < t < t_2$) and then released ($t = t_3$)..... 74

Figure 5.4: Drift polluted (gray) and corrected (colored) Euler parameters defining the orientation of the bottom link up until 10 seconds after t_3 during the example trial. 75

Figure 5.5: Reaction force (A) and moment (B) at j_2 as measured by the load cells (dashed) and estimated using IMU data (solid). The three colors distinguish components resolved in frame G: blue= $\hat{E}_1^G$, green= $\hat{E}_2^G$, and red= $\hat{E}_3^G$ 77

Figure 5.6: Three components of normalized force (A) and moment (B) acting at j_2 as predicted by IMU-enabled inverse dynamic modeling plotted against those measured directly by the load cell. The three colors distinguish components resolved in frame G: blue= $\hat{E}_1^G$, green= $\hat{E}_2^G$, and red= $\hat{E}_3^G$ 78

Figure 5.7: Force (A) and moment (B) components at j_1 and force (C) and moment (D) components at j_2 for updated mass center positions. Solid curves correspond to IMU-predicted reactions while dashed curves correspond to load cell measurements. 81

Figure 5.8: Force (A) and moment (B) at j_1 and force (C) and moment (D) at j_2 for updated mass center positions..... 82

Figure 6.1: Two faces of the miniaturized, wireless IMU used in this study. Major components are labeled..... 88

Figure 6.2: A mechanical approximation of a human “hip joint” (A) composed of a ball bearing (38 mm dia.) seated between two shallow spherical cavities. One cavity is machined in the proximal side of the joint (black) and the other is machined into the distal side (white). Stretched o-rings provide joint pre-loading. The extension of the distal side (B) supports a machined calibration jig (black) with the embedded wireless IMU.. 90

Figure 6.3: Three components of angular velocity (A) and three components of acceleration (B) data for an example 60-second trial. Trial consists of two phases of circumduction motion (“Cir” annotation, gray box) followed by two phases of rotation motion (“Rot” annotation, yellow box). Components of angular velocity and acceleration resolved along the IMU-fixed frame are distinguished by the following colors: x axis = blue, y axis = green, z axis = red 93

Figure 6.4: The magnitude of the measured acceleration (blue) from Fig. 6.3B once gravity is removed and the magnitude after adding the simulated noise due to soft-tissue motion (red). 96

Figure 6.5: The effect of soft-tissue acceleration on the predicted components of the position vector $\vec{r}_{c/a}$. Correlations (A, C, E) plot components predicted from randomly polluted data versus original values for each trial and relative to a line having unit slope. Bland-Altman plots (B, D, F) further illustrate difference in results. 98

List of Tables

Table 2.1: Summary of velocity (V) and position (P) constraints used to determine drift correction polynomials in each of the three field-fixed directions. 19

Table 2.2: Summary of differences, mean (standard deviation), between IMU- and motion capture-derived velocity components during the throwing motion and at the instant of release. All values are reported as a percentage. 21

Table 3.1: Closed-form solution to Euler's equation (3.1) as determined by the constants of the motion H and T 33

Table 3.2: Quantitative comparison of theoretical and experimental angular velocity components. Relative root-means-square error for each angular velocity component averaged over all 16 trials. The error measure is given by eq. (7) and reported in this table as a percentage. 41

Table 3.3: Relative root-mean-square error for angular velocity components reconstructed using a single, tri-axial accelerometer as compared to those measured directly from the angular rate gyros. 46

Table 4.1: Mean (and standard deviation) of RMS error (RMSE), RMSE relative to peak speed estimated by MOCAP (% RMSE), correlation coefficient (r), and slope of IMU-predicted speed compared to MOCAP for 10 trials of each of the four motion types. 59

Table 4.2: Mean (standard deviation) of RMSE correlation coefficient (r), and slope of IMU-estimated speed compared to MOCAP-estimated speed for all 40 trials (80 motion periods total, where n is the number included in each group). Separately considered are motion periods with integration times less than versus greater than 10 seconds. 61

Table 5.1: Summary of dimensions, mass and principal moments of inertia for each link. 70

Table 5.2: Mean and standard deviation of root mean square error (RMSE) and correlation coefficient (r) between IMU-calculated link angles and encoder-measured link angles for all ten trials. 76

Table 5.3: Mean (standard deviation) of RMS difference (RMSE) and correlation coefficient (r) for IMU-derived force and moment components compared to those measured by the load cells at j_1 and j_2 for the 10 trials of pendulum data considered and collocated link geometric and mass centers. 79

Table 5.4: Mean (standard deviation) of RMS difference (RMSE) and correlation coefficient (r) for IMU-derived force and moment components compared to those measured by the load cells at j_1 and j_2 for the 10 trials of pendulum data considered and updated mass center location. 83

Table 6.1: Summary of benchmarking experiment, mean (standard deviation) of each component of the joint center position $\vec{r}_{c/a}$ (in mm) for 14 trials of CMM data and 28 trials of IMU data. Third row reports difference in the averages (in mm). Fourth column reports vector sum of the components (in mm). 94

Table 6.2: Summary of benchmarking experiment, mean (standard deviation) of each component of the joint center position for 14 trials of CMM data and 28 trials of IMU data in mm. Least-squares estimate employing the fully polluted set of data is denoted method "IMU+P." 96

Abstract

Miniature inertial measurement units (IMUs) have become popular in the field of biomechanics as an alternative to expensive and cumbersome video-based motion capture (MOCAP). IMUs provide three-axis sensing of angular velocity and linear acceleration in lieu of position data provided by MOCAP. The research presented herein further explores the use of IMUs in five applications for sports training and clinical biomechanics.

The first study focuses on the sports of baseball and softball and yields estimates of the release velocity of a pitched ball within 4.6% of MOCAP measurements. The ball angular velocity further distinguishes and quantifies different types of pitches. The second study enables estimates of angular velocity during free-flight based solely on data from an embedded tri-axial accelerometer. Doing so eliminates angular rate gyros, which are often range limited, yet yields angular velocity estimates accurate to within 2%. We further exploit this technique to reveal the rotational stability of rigid bodies in free-flight. The third study extends the use of IMUs to assess the speed of an athlete estimated from a torso-mounted IMU. The speed estimates remain highly correlated with those obtained by MOCAP ($r=0.96$, slope=0.99) for motions characteristic of explosive sports (e.g., basketball). Moreover, the accurate speed estimation algorithm (mean RMSE=0.35 m/s) does not require data from GPS or magnetometers rendering it valuable and usable in any environment (indoor or outdoor).

The remaining studies advance the use of IMU arrays to estimate joint reactions in multibody systems. The fourth study establishes the accuracy of this method using experiments on an instrumented double pendulum. Estimated reaction forces and moments remain within 5.0% and 5.9% RMS respectively of values measured via load cells. The final study addresses the companion need to measure the location of joint centers. A method employing a single IMU yields the center of rotation (CoR) of a spherical joint to within 3 mm as established by a coordinate measuring machine. The

simplicity and accuracy of this method may render it attractive for broad use in field, laboratory or clinical applications requiring non-invasive, rapid estimates of joint CoR.

Chapter 1: Introduction

1.1. Motivation

Research questions regarding human movement, especially those probing ways to prevent injury or to improve athletic performance, have been explored for decades [1–4]. While most of this research is motivated by clinical applications, the techniques used to collect the requisite kinematic data are largely restricted to the laboratory [1–6]. While there is no debating the value of laboratory studies in understanding human motion, injury mechanisms, and athletic performance, the space constraints and contrived nature of testing may diminish the conclusions that are drawn and hamper the translation of results into practice [5,7]. Fortunately, rapid development in MEMS sensors and wireless technology combine to yield new approaches for measuring human motion which provide a potential solution to these limitations. In particular, the combination of MEMS inertial sensors and low power RF chipsets enable the development of highly miniaturized, wireless inertial measurement units (IMUs) for human motion tracking. This technology, which enables human motion analysis outside the laboratory, is still in its infancy and fundamental studies are needed to fully exploit its potential in far-reaching applications.

1.2. Methods for Quantifying Human Motion

The state of the art for quantifying human motion is video-based motion capture (MOCAP). MOCAP is essentially a lab-based method for tracking human motion which, unfortunately, is difficult to utilize in the clinic or on the field of play. MOCAP is also an expensive technology that employs an array of high-speed cameras arranged around the perimeter of a measurement volume. The cameras are calibrated to yield the three-

dimensional position coordinates of a set of markers which are often reflective targets or infrared LEDs, see for example [1,8–10]. In human biomechanics studies, markers are often attached to the skin via adhesive tape in locations that define bony anatomical landmarks [11]. They can also be attached to form fitting suits, combined to form clusters strapped to the body, or in rare instances, screwed directly to bone [12]. Measurements are often performed in a dedicated motion-capture laboratory, are restricted to a limited capture volume, and require an operator skilled in marker placement, calibration, and the collection and analysis of marker position data.

Human biomechanical analyses seek to understand the underlying kinematics and/or kinetics governing human motion. MOCAP provides position data for both purposes. In particular, MOCAP provides the marker position data that defines the three-dimensional kinematics of the major body segments. The same marker position data can also be employed to estimate joint reactions via inverse dynamics, often with the companion use of force plates to measure ground reactions. Doing so requires knowledge of the angular velocity and angular acceleration of each segment, segmental mass center acceleration, and segmental geometric and inertial properties [13]. Computation of velocity and acceleration from marker position data requires a sequence of differencing operations. In particular, differencing position data yields segment orientation and subsequent numerical differentiations yield angular velocity and angular acceleration. Successive numerical differentiations are also required to compute segmental mass center velocity and acceleration. It is well established that numerical differentiations may significantly amplify errors in the sampled position data (due to measurement error, marker occlusion, skin motion, etc.), resulting in potentially large errors in the very kinematic quantities required for the inverse dynamic estimates of joint reactions [3,14].

In an effort to minimize the effect of skin motion in particular, researchers have proposed optimized marker positions to limit the number of markers over large areas of soft tissue (e.g. muscle and/or body fat) [8]. Methods that avoid the use of markers completely include stereo radiography [4] and real-time MRIs [15] which both yield accurate descriptions of bone movement. However, they also expose subjects to radiation (radiography) and confine motion to highly constrained volumes (radiography and

MRIs). As an alternative, "markerless" video motion capture methods have also been developed [12,16–18]. These methods employ one or more high-speed video cameras to record a subject's motion and fit a model of the human form to the recorded images/frames. While similar to tracking marker positions, markerless motion capture is computationally intensive and requires significant assumptions for estimating bone position and orientation. It also suffers from the same constraints on measurement volume of all video-based techniques.

The shortcomings imposed by accuracy, cost, portability and measurement volume prevent widespread adoption of MOCAP as a clinically viable method for quantifying human motion. However, some or all of these shortcomings may be addressable by advancing an alternative technology, namely miniaturized inertial measurement units (IMUs). Miniature IMUs, which incorporate MEMS accelerometers and angular rate gyros, measure the angular velocity and linear acceleration of any rigid body to which they are attached. When deployed as a body worn sensor array, miniature IMUs directly provide the angular velocity and linear acceleration of body segments needed for many biomechanical analyses. For the purpose of inverse dynamics, only a single derivative operation and a single integral operation are required to yield the angular acceleration and orientation data, respectively that are also required. Thus, miniature IMUs have the potential to provide far more accurate kinematic data than (position-based) MOCAP for inverse dynamics. Perhaps even more attractive, miniature IMUs remain highly portable and can be deployed in the clinic, in the workplace, or on field of play and for a very small fraction of the cost of MOCAP [19,20]. These advantages provide substantial motivation for advancing this promising technology for applications in sports training and clinical biomechanics.

1.3. Research Objective and Scope

The overall objective of this dissertation research is to advance the use of miniature IMUs for novel applications in sports training and clinical biomechanics. Doing so requires advances both in algorithms and experimental procedures to yield accurate estimates of kinematical variables. In concert, we validate the accuracy of IMU-

derived kinematical variables through carefully designed benchmark experiments. We bring this approach to bear on five applications that span: 1) the motion of pitched baseballs and softballs, 2) the rotational dynamics and stability of rigid bodies in free-flight, 3) the velocity of a running athlete, 4) the joint reactions deduced from IMU data, and 5) the accurate estimation of joint centers. The motivation, background, methods and results for each of these applications is described in a separate chapter which also represent independent publications. A synopsis of all five chapters is provided below which further highlights the principal contributions of each study.

1.3.1. Chapter 2: Dynamics of Pitched Baseballs and Softballs Revealed via Ball-Embedded IMU.

The first study advances the use of IMUs to understand the dynamics of human throwing in the sports of baseball and softball. In particular, we examine the dynamics of pitched baseballs and softballs using a highly miniaturized, ball-embedded, wireless IMU.

The aerodynamic forces responsible for the "break" (or curve) in the path of a pitched ball trace to the release conditions of the ball from the pitcher's hand including the orientation, spin, and velocity of the ball [21,22]. These release conditions ultimately differentiate one pitch type from another. For example, the fastball and changeup are released with substantial backspin in relation to the ball center velocity. By contrast, the curveball largely spins in the opposite direction; that is, it has substantial topspin. The slider has a combination of topspin and sidespin [23,24].

The majority of studies on the biomechanics of pitching utilize video-based motion capture to quantify the athlete's pitching motion or standard high-speed video to quantify the dynamics of the pitched ball [21,24–26]. As noted above, these techniques are limited by constrained capture volumes, special lighting conditions, and, in the case of MOCAP, the significant amount of time to apply/adjust markers. Two recent studies explore the use of wireless IMUs for baseball pitcher training [27,28] where the IMUs are mounted to the throwing arm. Unfortunately, the size and mass of these selected IMU

designs [27,28] preclude their use for directly measuring the motion of the pitched baseball or softball.

To address these physical shortcomings, we introduce a highly miniaturized IMU that is directly embedded within the small confines of a baseball/softball. This design yields a low cost, highly portable and minimally intrusive technology for measuring the kinematics of a pitched ball right on the field of play. In particular, this technology yields a quantitative means for characterizing pitch type and consistency by resolving both the ball velocity and angular velocity at release, as well as throughout the pitching motion (for pitches that remain within the measurement range of the associated angular rate gyros). The computational methods described in this chapter estimate and correct for sensor drift errors in arriving at superior estimates of the ball center velocity. Results are validated by benchmarking IMU-derived ball velocity against that obtained using a Vicon^{TM} (Los Angeles, CA, USA) motion capture system. IMU-based estimates of the release velocity of the ball remain within 4.6% of the MOCAP measurements. Promising ways that this technology can support pitcher training are also emphasized.

1.3.2. Chapter 3: Rotational Dynamics and Stability of Rigid Bodies in Free-Flight

A major limitation noted in the previous study is that highly skilled pitchers release the ball at spin rates that may fall outside the measurement range of most angular rate gyros. In answer to this challenge, Chapter 3 presents a novel method for identifying the free-flight angular velocity of a rigid body using data solely from a tri-axial accelerometer. The chapter opens by reviewing the theory governing the torque-free motion of a rigid body, which is a classical topic in rigid body dynamics; see, for example, [29–31]. An elegant experimental method reveals the free-flight dynamics of a rigid body. At the heart of the method is a highly miniaturized wireless IMU which is used to directly measure acceleration and angular velocity during free-flight for direct comparison with theory. The precession of the angular velocity vector in a body fixed frame is observed through the construction of experimental polhodes. Rotations initiated close to the major, minor and intermediate principal axes closely obey predictions from classical theory. This experimental verification of classical free-flight dynamics further

enables the reconstruction of the angular velocity vector from measurements made with a single, tri-axial accelerometer. Doing so leads to angular velocity predictions that remain within 2% of the angular rates directly measured by the rate gyro. This simplification, which has practical use in resolving the spin of a pitched baseball or softball, provides an inexpensive alternative to using angular rate gyros. Moreover, the angular velocity reconstruction method herein runs counter to prior claims that a minimum of six independent accelerometer outputs are required for this purpose [32,33].

1.3.3. Chapter 4: The Velocity of a Running Athlete

Chapter 4 extends the algorithms for estimating ball velocity presented in Chapter 2 to estimating the velocity of an athlete directly and non-invasively on the field of play. Doing so complements the growing interest in employing MEMS inertial sensors and GPS technology to monitor and assess athletic performance [34–37]. Several products have recently come to market which exploit these technologies to identify performance metrics (e.g., speed, acceleration, load, etc.) useful for training and coaching [34,38–41]. Two designs in particular incorporate sensor modules into clothing, holding them tightly against the athlete's torso and removed from the extremities (hands and feet) used for play [38,40]. Both of these designs specifically target outdoor sports, like soccer, rugby and Australian football, where the fusion of IMU and GPS data is used to estimate athlete speed [40]. However, the lack of GPS signals in indoor arenas renders these sensor fusion methods useless for sports such as basketball [42]. Moreover, existing GPS-free techniques require subject-specific calibration, lower-limb mounted IMUs, or even an array of IMUs to provide accurate speed estimates [43–48].

We address these limitations by introducing a new method for estimating athlete speed which utilizes a single, torso-mounted IMU, and does not require subject-specific calibration. The key to this method is correcting velocity drift errors by exploiting identified periods of time when the athlete is momentarily at rest. The resulting estimates of instantaneous and average speed are compared to those determined from a Vicon™ motion capture system for numerous trials representative of athlete motion in explosive sports like basketball. These comparisons demonstrate that this technique predicts

instantaneous athlete speed that is accurate (mean RMSE = 0.35 m/s) and highly correlated with MOCAP speed estimates (r = 0.96, slope = 0.99). Moreover, we show that the method predicts average speed to within an absolute mean error of 0.03 m/s, and an RMS error of 0.18 m/s which is 4.3% of the average MOCAP speed.

1.3.4. Chapter 5: Joint Reactions Deduced from IMU Data

The studies presented in Chapters 2 through 4 explore one major category of uses for IMUs in sports training where the focus is the accurate determination of kinematical variables that define athletic performance. Doing so opens the door to real-time and on-the-field assessment of athletes. Another major category of uses for IMUs is to estimate kinetic variables for human motion, and particularly the reactions at the major skeletal joints by combining the kinematic data offered by IMUs with inverse dynamic modeling of the major body segments. Motivation for doing so extends well beyond sports and sports injury applications. Consider, for example, the aging US population and the predicted enormous increases in musculoskeletal injuries. For example, the annual number of total hip and knee replacement surgeries are predicted to increase by over 170% (to 572,000) and 670% (to 3.48 million) respectively by the year 2030 [49]. This alarming increase in joint replacements supports the need for non-invasive, clinically viable methods to identify pathological lower extremity motion before joint injuries occur. One of these potential methods, inverse dynamic modeling, begins by approximating the human body as a collection of rigid segments connected by joints. Knowledge of the segmental kinematics, namely the angular velocity and angular acceleration of each segment and the linear acceleration of the segment's mass center, enables a solution for the reactions (i.e. forces and moments) acting at the joints provided segmental inertial properties (e.g. mass center location, mass, inertia, etc.) are also known [13].

Typically, MOCAP is used to provide the segmental kinematic information necessary for inverse dynamic modeling, but this approach is not possible in clinical settings due to the many limitations described above (e.g., accuracy, cost, portability and measurement volume) [5,6,19,20]. In contrast, IMUs enable accurate measurement and

calculation of the kinematic quantities necessary for inverse dynamic modeling without the constraints of MOCAP. Before IMUs can be employed as a clinically viable tool, the accuracy of joint reactions estimated by IMU data needs to be verified against precise gold standards. To this end, Chapter 5 presents a benchmarking study where the reaction forces and moments acting at the joints of a well characterized mechanical system are estimated from IMU kinematic data and compared to reactions directly measured by highly precise six degree-of-freedom force and torque sensors. Doing so reveals that predicted reaction forces and moments remain within 5.0% and 5.9% RMS, respectively, of load cell measurements and with correlation coefficients greater than 0.95 and 0.88, respectively.

1.3.5. Chapter 6: Accurate Estimation of Joint Centers

The inverse dynamic modeling technique of Chapter 5 requires knowledge of both mass and joint center (defined as the joint center of rotation, CoR) location to form the Newton and Euler equations of motion. Specifically, mass center location is required to calculate mass center acceleration for Newton's second law, while both mass and joint center locations are required for Euler's second law. Marker positions and anthropometric data are used to define these locations when MOCAP is used to estimate body-segment kinematics. However, when deploying a segment-mounted IMU, this marker position information is no longer available. Moreover, a segment-fixed IMU measures the acceleration at the location of the accelerometer (not necessarily the mass center) and the angular velocity of the segment. One can use this data to calculate the mass center acceleration needed for Newton's second law (the solution of which is required for the Euler equations of motion) provided the location of the mass center is known relative to the accelerometer. This position, while generally unknown and inaccessible, can be deduced from anthropometric data if the location of a joint CoR is known relative to the accelerometer.

Existing (non-IMU) methods for determining joint CoR either estimate CoR position based on the location of bony anatomical landmarks [50–53] or by the relative 3-D position of adjacent body segments [54–59]. One method that exploits a segment-

mounted IMU computes CoR position using algorithms similar to those presented in [54–58]. However, the algorithms all rely on IMU-derived velocity and position estimates [60]. These estimates, obtained by successive integrations of the IMU-measured acceleration, are subject to error due to sensor drift [61] leading to potentially inaccurate estimates of joint CoR.

The final study presented in Chapter 6, introduces a new IMU-based algorithm for estimating the CoR of a spherical joint that avoids the need for (error-prone) velocity and position estimates. This method utilizes solely the acceleration and angular velocity data directly measured by the IMU. The CoR location for a mechanical device approximating the human hip joint is predicted by the proposed algorithm and is then benchmarked against the CoR location measured directly via a precise digital coordinate measuring machine. The results confirm that this new method resolves the position of the CoR to within a 3 mm sphere of the true CoR.

Chapter 2: Dynamics of Pitched Baseballs and Softballs Revealed via Ball-Embedded IMU

2.1. Introduction

Baseball and softball pitching demand highly dynamic full body movements with precise neuromuscular control. This control begins with the way the pitcher grips the ball, continues through the windup and delivery, and culminates in the ball's release. This instant in the sequence of the pitching motion is integral for the execution of different types of pitches; for instance, a fastball versus a breaking ball in baseball, or a rise ball versus a drop ball in fast pitch softball. Considerable research has addressed the flight path of the pitched ball after release and the governing aerodynamic forces [21,22,62]. Despite these advances, pitching coaches largely rely on qualitative assessments of pitching mechanics and outcomes in the form of visual inspection of the throwing motion, radar gun measurements, ball and strike counts, and ERA (earned run average) for training and skill assessment [7].

An important subset of studies focuses on "breaking" ball pitches, including the curveball [21,22,62]. The aerodynamic forces responsible for the "break" (or curve) in the flight path trace to the release conditions from the pitcher's hand including the orientation, spin, and velocity of the ball. In particular, experiments reveal that the total break of the flight path (1) is proportional to the ball's aerodynamic lift coefficient [21], (2) is dependent on the seam orientation [21], and (3) is a function of the magnitude and direction of the ball's angular velocity with respect to the velocity of its mass center [22]. The release conditions ultimately differentiate one pitch type from another. The fastball and changeup are released with substantial backspin in relation to the ball center velocity. By contrast, the curveball largely spins in the opposite direction; that is, it has substantial topspin. The slider has a combination of topspin and sidespin [23,63].

Studies of pitching mechanics largely rely on positional data obtained via high-speed cameras [1,7,10,23,25,63–65]. However, video-based motion capture is expensive, time consuming, and often requires measurements in the lab made by an operator skilled in both the collection and analysis of the data. Furthermore, baseball and softball angular velocity is very difficult to resolve using video based systems due to marker occlusion while the ball is in the pitcher's hand, and the high angular rates. Nevertheless, the angular velocity of the ball at release has an overriding influence on the subsequent ball flight path as noted above. For these reasons, it is quite challenging to use high speed motion capture to support pitcher training on the field of play.

The advent of MEMS inertial sensors and MEMS-scale wireless transceivers provide an attractive alternative to video-based motion capture for this application. Recent studies explore the use of wireless inertial measurement units (IMUs) for baseball pitcher training [27,28] among other sports training applications [66–70]. However, the size and mass of the IMUs employed in [27,28](and those commercially available from companies like Xsens^{TM}, Culver City, CA, USA) preclude their use in measuring the motion of a baseball or softball.

To address these physical shortcomings, we introduce a highly miniaturized IMU that is directly embedded within the small confines of a baseball/softball. Doing so provides a low cost, highly portable and minimally intrusive technology for measuring the kinematics of a pitched ball right on the field of play. In particular, this technology provides a quantitative means for characterizing pitch type and consistency by resolving both the ball velocity and angular velocity at release, as well as throughout the pitching motion. We open this paper below with a description of the IMU hardware and the computational methods used to deduce ball-center velocity. We validate this method by benchmarking IMU-derived results with those obtained using a VICON (Los Angeles, CA, USA) motion capture system. In the process, we emphasize the probable ways that IMU-derived kinematical results can support pitcher training.

2.2. Sensor Design and Experimental Methods

Figure 2.1 illustrates the IMU hardware employed in this study. This design was developed at the University of Michigan following a lineage of other multi- and single-board designs used for sports training, biomechanics, and rigid-body dynamics applications [66,67,69–71].

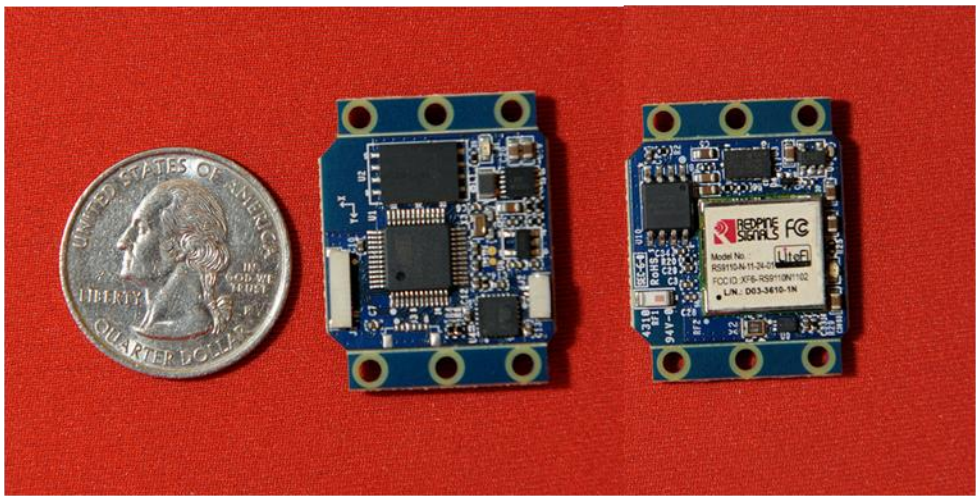

Figure 2.1: Highly miniaturized wireless IMU design used in this study was approximately the size of a quarter. The IMU provides three-axis sensing of acceleration and angular velocity with wireless data transmission to a host computer.

The design includes two sensing components. One is a digital tri-axial angular rate gyro, which performs internal 16-bit A/D conversion, with a measurement range of 2,000 deg/s, noise magnitude of 0.38 deg/s-rms for each axis (at 100 Hz output), and sampling frequency of 512 Hz. The other is a digital tri-axial accelerometer, which performs internal 13-bit A/D conversion, with a measurement range of 16 g, noise magnitude of 0.004 g-rms for each axis (at 100 Hz output), and sampling frequency of 800 Hz. Data from the IMU is low-pass filtered, with a cutoff frequency of 100 Hz before use. The IMU includes 8 Mbytes of onboard flash memory enabling operation in a data logging mode during trials after which the data can be downloaded to a host computer over a standard Wi-Fi network. The board measures a mere 30.1 × 23.7 × 5.1 mm and, when packaged with a switch and small lithium-ion battery, has a total mass of 12 g.

Prior to use, the IMU is calibrated following the procedure detailed in [68]. This procedure, which consists of two rotations about each of the three orthogonal sense axes,

ultimately determines 24 calibration parameters (including scale factors, cross-axis sensitivity scale factors, and biases) for the IMU components. Doing so ensures that the acceleration and angular rate measurements are accurately resolved along a common orthogonal triad of sensor-fixed unit vectors. Bias values for the rate gyro are updated during each trial to ensure that changes due to temperature, battery voltage, or other external factors are captured.

The IMU, battery, and switch are embedded in regulation softballs and baseballs enabling the measurement of ball dynamics during the throw. Figure 2.2 provides a "before" and "after" image of the instrumented baseball.

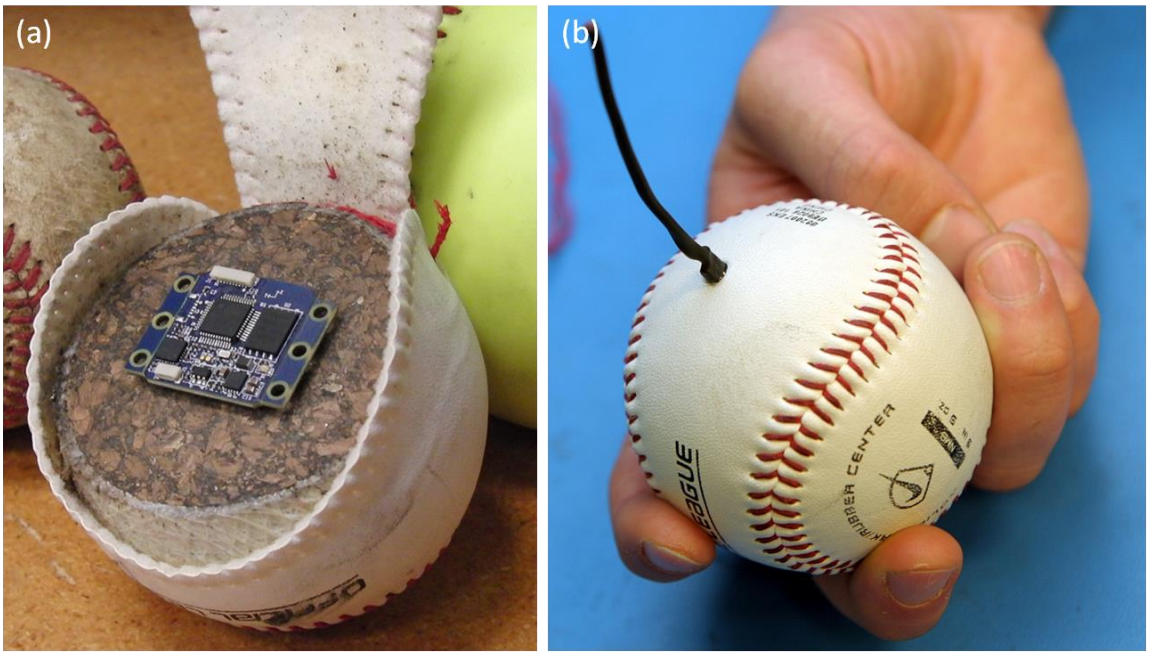

Figure 2.2: (a) The miniaturized IMU shown as it would be embedded in a baseball. (b) Final version of the ball including a small jack (switch/recharging) which is removed prior to the throw.

For both baseballs and softballs, the miniaturized IMU, battery, and switch are embedded in the ball (Figure 2.2(a)). Installation begins by unstitching half of the cover, after which the cork and rubber core is cut into two halves. Two small pockets are machined in the core, one to accommodate the battery and IMU and another for a switch which is accessible from the exterior via a hole in the cover large enough to

accommodate a 2.5 mm phone plug. The IMU, battery, and switch are captured in these pockets with epoxy, and the two halves of the core are glued together prior to re-stitching the cover. The result is an instrumented baseball (Figure 2.2(b)) or softball. The mass of the instrumented baseball is within 0.1 g of its original (uninstrumented) mass (the softball is within 1.3 g). For either, this represents less than a 0.7% perturbation to the mass of the ball. For comparison, the official rules of baseball and softball dictate that the mass of a baseball may vary by as much as 7.1 g and the mass of a softball by as much as 20.4 g. It is important to mention that while the instrumented ball is able to survive repeated impacts with a catcher's mitt, it would not withstand an impact with a bat.

As emphasized above, a major use of this technology is to measure the release conditions of the ball, that is, the velocity of the ball center and the angular velocity of the ball at release from the pitcher's hand. The angular velocity is measured directly from the angular rate gyro for pitches that remain within its measurement range. Unfortunately, the average MLB fastball rotates at about 15,000 deg/s which is considerably outside the range of the gyro used in this IMU [72]. Until recently, the best solution would be to estimate the angular velocity during free flight based on data from the tri-axial accelerometer following the methods discussed in [71]. However, subsequent to our study, MEMS device manufacturers (e.g., Analog Devices), released angular rate gyros capable of measuring angular rates up to 20,000 deg/s thus enabling application of the methods presented herein to potentially all baseball and softball pitches. In contrast, the velocity of the ball center must be computed (using data from both the gyro and the accelerometer) following the steps outlined in Figure 2.3(b) and as summarized below.

The following testing protocol was used. Each pitcher was instructed to pick the ball off of a tee, come to their natural "set" position, and then pitch the ball to the catcher. In addition, the subjects threw each pitch in a way to keep the ball angular velocity within the present measurement range of the gyro (2,000 deg/s). In this study data was collected from five pitches thrown by one baseball and one softball pitcher, both between 21 and 23 years of age. Both pitchers had previously competed at the high school level. Each pitcher was instructed to warm-up for as long as they determined was sufficient. They then threw 10 pitches to a catcher yielding five pitches with sufficient data from motion capture to enable benchmarking with this alternative measurement method. The vector

magnitude of the measured acceleration for a representative softball pitch is reported in Figure 2.3(a), which also illustrates the major phases of the throwing motion.

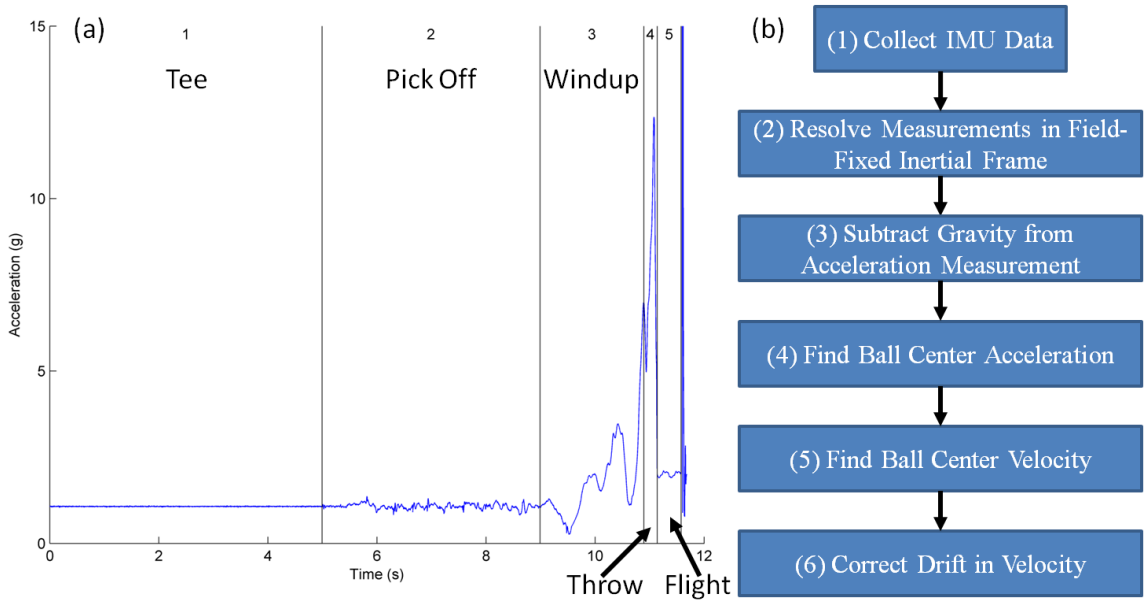

Figure 2.3: (a) Magnitude of acceleration as measured by the embedded IMU during a representative softball pitch. Major phases of the throwing motion are labeled 1–5. (b) Flow chart of major steps to calculate ball-center velocity during the throw.

Phase 1 corresponds to the time where the ball is in the tee prior to the throw. Phase 2 extends from the time where the pitcher picks the ball off of the tee to the instant she begins her windup (end of "set position"). Phase 3 begins at the start of the windup and extends to the instant when the pitcher's hand is furthest away from the catcher prior to release. Phase 4 extends from the end of Phase 3 to release. Finally, Phase 5 is the free-flight phase of the ball en-route to the catcher. The measured acceleration shown in Figure 2.3(a), combined with the measured angular velocity enable the calculation of ball-center velocity according to the steps outlined in Figure 2.3(b) and summarized next.

The acceleration and angular velocity data, measured in the non-inertial or "ball-fixed" frame, are transmitted to and stored on the host computer. This data must ultimately be resolved into components associated with an inertial (field-fixed) frame; refer to Step 2 in Figure 2.3(b) and to Figure 2.4. The ball-fixed reference frame is denoted by the mutually orthogonal triad of unit vectors ($\hat{x}, \hat{y}, \hat{z}$) with origin p at the

center of the accelerometer; refer to Figure 2.4(a). The inertial, or "field-fixed" frame is denoted by the triad of unit vectors ($\hat{X},\hat{Y},\hat{Z}$) with origin located at the ball center when placed in the tee (point *O*; Figure 2.4(b)).

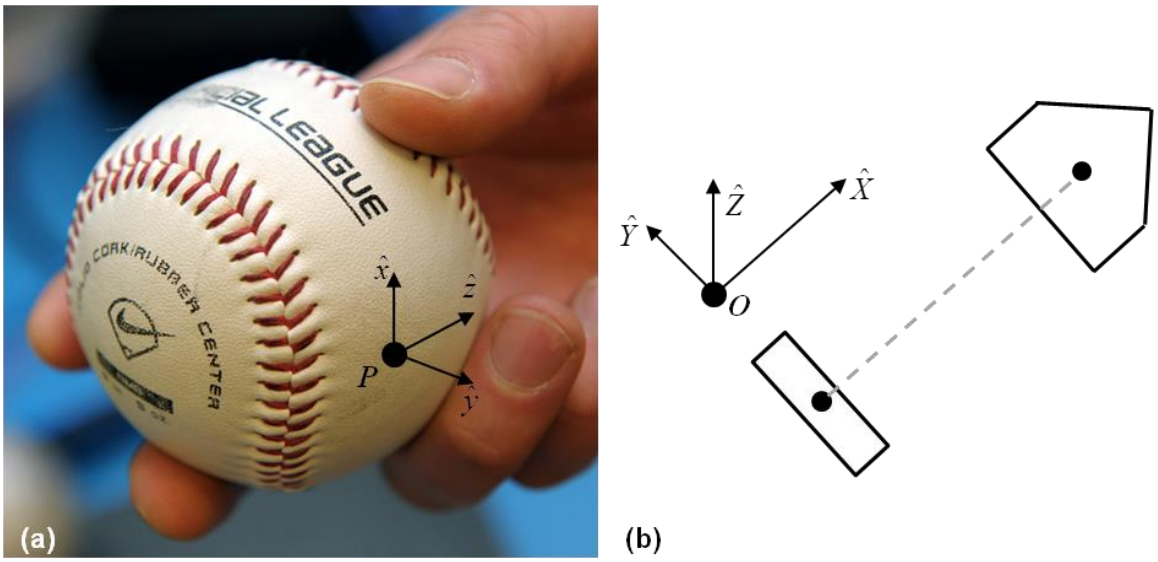

Figure 2.4: (a) Ball-fixed reference frame with origin at the center of the accelerometer (*P*). (b) Field-fixed reference frame with origin at location of the ball center in tee (*O*) at the start of the trial.

The transformation (direction cosine matrix) that relates these two frames and the differential equation which governs its evolution over time are:

$$\vec{x}\big|_{\hat{X},\hat{Y},\hat{Z}} = \Lambda\, \vec{x}\big|_{\hat{x},\hat{y},\hat{z}} \tag{2.1}$$

$$\dot{\Lambda} = \Lambda\hat{\tilde{\omega}} \tag{2.2}$$

where Λ is the standard definition of a direction cosine matrix (DCM) [73], $\vec{x}\big|_{\hat{x},\hat{y},\hat{z}}$ denotes the components of a vector $\vec{x}$ resolved in the ball-fixed frame, and $\vec{x}\big|_{\hat{X},\hat{Y},\hat{Z}}$ denotes the components of the same vector resolved in the field-fixed frame. During the throwing motion, the ball-fixed frame is both translating and rotating with respect to the field-fixed frame. As described below, the DCM is a function of the angular velocity of the ball, and is computed upon integrating (2.2) following an adaptation of the algorithm in [74]. The adapted algorithm employs a numerical approximation to (2.2) in which $\dot{\Lambda}$

denotes the time derivative of the DCM and $\hat{\bar{\omega}}$ denotes the ball-fixed angular velocity vector in skew-symmetric form. The midpoint approximation to the solution of (2.2) yields the DCM at time step n+1 in terms of its value at time step n per:

$$\Lambda_{n+1} = \Lambda_n \left[\mathrm{I} + \frac{1}{2}\hat{\bar{\theta}} \right] \left[\mathrm{I} - \frac{1}{2}\hat{\bar{\theta}} \right]^{-1} \tag{2.3}$$

In Equation (2.3), $\hat{\bar{\theta}}$ denotes the midpoint approximation of the change in orientation from time step n to n+1 in skew-symmetric form defined by:

$$\hat{\bar{\theta}} = \frac{1}{2}\Delta t \left(\hat{\bar{\omega}}_{n+1} + \hat{\bar{\omega}}_n \right) \tag{2.4}$$

where $\hat{\bar{\omega}}_{n+1}$ and $\hat{\bar{\omega}}_n$ are the (measured) ball-fixed angular velocities at time steps n+1 and n respectively in skew-symmetric form, and $\Delta(t)$ is the time interval between time steps n and n+1. Thus, the IMU provides the ball-fixed angular velocity needed to solve for the time-varying DCM, $\Lambda(t)$, via Equation (2.3) provided an initial value, $\Lambda(0)$, is also known. This initial value is determined by employing the accelerometer as an inclinometer during Phase 1 while the ball remains at rest in the tee following the procedure detailed in [67]. Thus, the acceleration vector can now be resolved in the field-fixed reference frame completing Step 2 in Figure 2.3(b).

Since the accelerometer measures signals down to 0 Hz, the resulting measurement also includes the acceleration due to gravity which must now be subtracted. Removal of gravity and computation of the ball-center acceleration (Steps 3 and 4 in Figure 2.3(b)) follows from:

$$\vec{a}_c(t) = \Lambda(t)\left[\vec{a}_m(t) + \dot{\bar{\omega}}(t) \times \vec{r}_{c/p} + \bar{\omega}(t) \times (\bar{\omega}(t) \times \vec{r}_{c/p}) \right] - g\hat{K} \tag{2.5}$$

in which $\vec{a}_c$ is the ball-center acceleration resolved in the field-fixed frame, $\vec{a}_m$ is the measured acceleration in the ball-fixed frame, $\bar{\omega}$ and $\dot{\bar{\omega}}$ are the measured angular velocity and calculated angular acceleration (finite difference method), respectively, and $\vec{r}_{c/p}$ is a position vector which locates the ball center relative to the center of the accelerometer. Direct integration of the ball-center acceleration (numerically using the trapezoidal method) yields the ball-center velocity per Step 5 of Figure 2.3(b) subject to the initial condition that this velocity starts from zero as the ball is held still in the tee.

It is well established that integration of the IMU-measured acceleration introduces significant error in the velocity due to drift [61,75]. This drift error is approximately identified and removed per Step 6 of Figure 2.3(b). We do so by splitting the throw into three parts: Part 1 spans Phases 1 and 2, Part 2 spans Phases 3 and 4, and Part 3 corresponds to Phase 5. Each Part is characterized by qualitatively distinct ball dynamics and thus distinct error correction. To this end, we introduce polynomial approximations to the drift error for each field-fixed component of velocity during each Part per:

$$V_j(t) = V_{uc,j}(t) - \left(C0_j + C1_j t + C2_j t^2 + C3_j t^3\right) \text{ where } j = x,\ y,\ z \qquad (2.6)$$

where V_j and $V_{uc,j}$ are the corrected and uncorrected *j*-components of velocity respectively. The right-hand side of (2.6) contains the *j*-component of the polynomial drift error function with constant coefficients $C0$-$C3$ defined separately for Parts 1, 2 and 3. In some sections the coefficients of the higher order terms (*i.e.*, $C2$ and/or $C3$) are identically zero resulting in a lower-order drift error polynomial. Specifically, all three components have cubic drift error functions during Part 1. During Parts 2 and 3 the $\hat{Y}$-component is linear while the $\hat{X}$- and $\hat{Z}$-components are quadratic in time. The zeroth order term in (2.6) enforces continuity of the corrected velocity component across the parts. The remaining coefficients are found by simultaneous solution of known velocity and position constraints on the ball as summarized in Table 2.1 where the phases noted refer to those defined in Figure 2.3(a). The positions reported in Table 2.1 are the measured (or estimated) height of the ball center (P_z) at the pitcher's set position (end of Phase 2), the height of the center of the strike zone (end of Phase 5), and the horizontal distance (Δx_5) the pitch is thrown. Also required are the acceleration due to gravity ($a_{gravity}$), the acceleration due to air drag (a_{drag}, estimated according to [22]) and the time duration of Phase 5 (Δt_5). These latter quantities are used to estimate the change in each of the three velocity components during Phase 5 ($\Delta V_{x,5}$, $\Delta V_{y,5}$, $\Delta V_{z,5}$).

$\hat{X}$	$\hat{Y}$	$\hat{Z}$
$V_x = 0$ during Phase 1	$V_y = 0$ during Phase 1	$V_z = 0$ during Phase 1
$V_x = 0$ end Phase 2	$V_y = 0$ end Phase 2	$V_z = 0$ end Phase 2
$V_x = 0$ end Phase 3	$V_y = 0$ end Phase 4	P_z = measured end Phase 2
$V_x = \triangle x_5 / \triangle t_5$ end Phase 4	$\triangle V_{y,5} = 0$	P_z = strike end Phase 5
$\triangle V_{x,5} = a_{drag} \triangle t_5$		$\triangle V_{z,5} = a_{gravity} \triangle t_5$

Table 2.1: Summary of velocity (V) and position (P) constraints used to determine drift correction polynomials in each of the three field-fixed directions.

The accuracy of the IMU-derived ball velocity is established by comparing it to that measured using a 10-camera high speed motion analysis system (VICON). The baseball/softball, with embedded IMU, was coated in reflective tape and its 3-D positions were measured by the VICON system at a frequency of 100 Hz and with calibrated position errors less than 0.25 mm. The ball's position data was low-pass filtered with a cutoff of 8.33 Hz and then numerically differentiated to determine the ball-center velocity as reported next.

2.3. Results and Discussion

We illustrate the promise of this sensor technology in this application by comparing ball-center velocities determined from IMU and motion capture (VICON) data. For experiments conducted on both baseball and softball pitching, we examine pitches thrown so that the angular rates do not exceed the measurement range of the IMU (2,000 deg/s). We open with an example that exposes the velocity drift error that is then corrected by the algorithm described above.

Figure 2.5(a) shows the ball-center velocity components in the field-fixed reference frame where the three field-fixed directions are distinguished as $\hat{X} = \text{blue}$, $\hat{Y} = \text{green}$, and $\hat{Z} = \text{red}$. The thick lines designate the three uncorrected velocity components calculated from IMU data while the thin lines designate the same quantities calculated using motion capture data. Comparison of these two data sets reveals obvious drift error resulting from the integration of Equation (2.5). Figure 2.5(b) reports the same

quantities but following the application of the drift error correction algorithm for the IMU data as described above. Inspection of this result shows excellent qualitative agreement between the IMU- and motion capture-derived results and in all major phases of the ball motion.

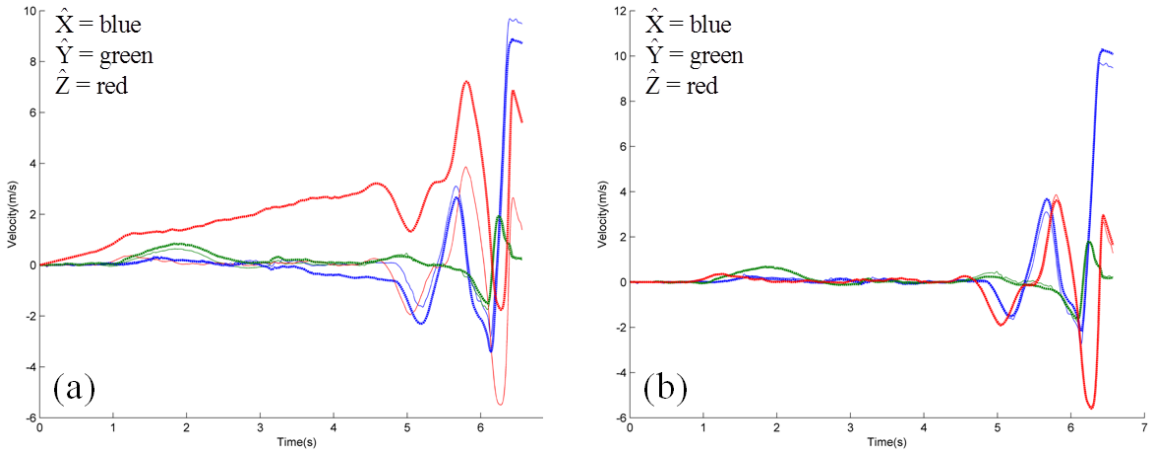

Figure 2.5: (a) Uncorrected and (b) Corrected ball-center velocity (m/s) components as determined by IMU (thick) and motion capture (thin) data for a representative softball pitch.

To now quantify this agreement, we introduce two metrics of the remaining small differences between the (drift corrected) velocity components based on the IMU data versus those measured using the motion capture data. The first metric is the normalized RMS difference between IMU-derived and motion capture-derived velocity components for the entire throwing motion:

$$\varepsilon_{cj} = \frac{\sqrt{(1/N)\sum_{i=1}^{N}(V_{cj,i} - \tilde{V}_{cj,i})^2}}{\left|MAX\left[V_{cj}(i \le i_{release})\right]\right|}, \text{ for } j = x,\ y,\ z, \qquad (2.7)$$

where V_{cj} is the motion capture-derived *j*-component of velocity, $\tilde{V}_{cj}$ is the IMU-derived *j*-component of velocity, and *N* is the number of data samples. The numerator of Equation (2.7) is the RMS difference between the *j*-velocity components, while the denominator normalizes this difference based on the maximum value of the motion capture *j*-velocity component while the ball is in the pitcher's hand. The second error metric is the percent difference in the components of the *release* velocity with the motion capture-derived velocity components taken as the "truth data":

$$\varepsilon_{cj,rel} = \sqrt{\frac{(V_{cj,rel} - \tilde{V}_{cj,rel})^2}{V_{cj,rel}{}^2}}, \text{ where } j = x,\ y,\ z \tag{2.8}$$

This second metric directly measures the accuracy of this sensor technology for determining the velocity of a pitched baseball/softball at release based on motion capture as the standard. A summary of these metrics for each velocity component, including mean and standard deviations, is reported in Table 2.2 for a sample of five baseball and five softball pitches.

The results of Table 2.2 for the first metric ε_c demonstrate that the ball-center velocity obtained using the sensor technology recreates that obtained by standard motion capture to within 10% for baseball and 6% for softball over the entire range of the throwing motion. Considering the velocity of the ball-center at release, results for the second metric $\varepsilon_{c,rel}$ demonstrate agreement to within 4% for baseball and 4.6% for softball.

	Baseball			**Softball**		
Error	$\hat{X}$ (%)	$\hat{Y}$ (%)	$\hat{Z}$ (%)	$\hat{X}$ (%)	$\hat{Y}$ (%)	$\hat{Z}$ (%)
ε_c	2.5 (0.3)	10.0 (1.6)	7.7 (2.0)	2.2 (0.6)	5.9 (1.3)	3.3 (0.6)
$\varepsilon_{c,rel}$	3.5 (2.4)	1.9 (2.1)	4.0 (3.6)	4.6 (2.3)	1.0 (0.5)	3.6 (1.3)

Table 2.2: Summary of differences, mean (standard deviation), between IMU- and motion capture-derived velocity components during the throwing motion and at the instant of release. All values are reported as a percentage.

This latter result is particularly important given the overall influence of the release velocity (and angular velocity) in determining pitch type and quality. In understanding these comparisons, it is important to mention that the motion capture system, treated as yielding "truth data" here, is also susceptible to measurement errors. These errors in position largely arise from replacing data points lost due to marker occlusion and are then magnified when that position data is differentiated to determine velocity. Thus, the reported differences include contributions due to errors in the motion capture method as well.

As emphasized above, the sensor technology provides the data essential to resolving the release conditions of the ball including the ball orientation, ball center

velocity (vector), and ball angular velocity (vector). These variables distinguish the types of pitches and they also provide a quantitative means for assessing the quality of each pitch type. By way of example, these potential uses are highlighted by the images of Figure 2.6 which illustrate the distinct release conditions for four common baseball pitches as measured by an embedded IMU (similar results were also obtained for the various types of softball pitches).

The images of baseball release conditions reported in Figure 2.6, for pitches thrown with modest linear and angular speed, confirm trends presented in [23,63]. Figure 2.6(a,b) illustrates the release conditions for a fastball and changeup, respectively. These two pitches are thrown largely with backspin which contributes to positive aerodynamic lift. This large backspin manifests as a large component of the angular velocity vector along the $-\hat{Y}$ direction. Additionally, a small amount of lateral break develops due to the small but noticeable side spin component of the angular velocity; *i.e.*, the small component of $\vec{\omega}$ along the $\hat{Z}$ direction. By contrast, Figure 2.6(c) shows that a curveball is released largely with top spin (note large component of $\vec{\omega}$ about $\hat{Y}$) which contributes to negative aerodynamic lift. Like the fastball and changeup, the small but readily visible side-spin component creates additional but small lateral break. Finally, Figure 2.6(d) shows the release conditions for a slider which is dominated by side spin (note large component of $\vec{\omega}$ about $\hat{Z}$) but also includes a small top spin component. The side spin induces a large lateral break, while the topspin induces a small drop. The position of the spin axis of the ball relative to the velocity of the ball center at release provides the essential information needed to evaluate whether the desired type of pitch is thrown correctly, to what degree the pitcher achieves that type of pitch, and (with multiple trials and measurements) how consistently it is being thrown. These measurement capabilities provide powerful information for evaluating pitching performance.

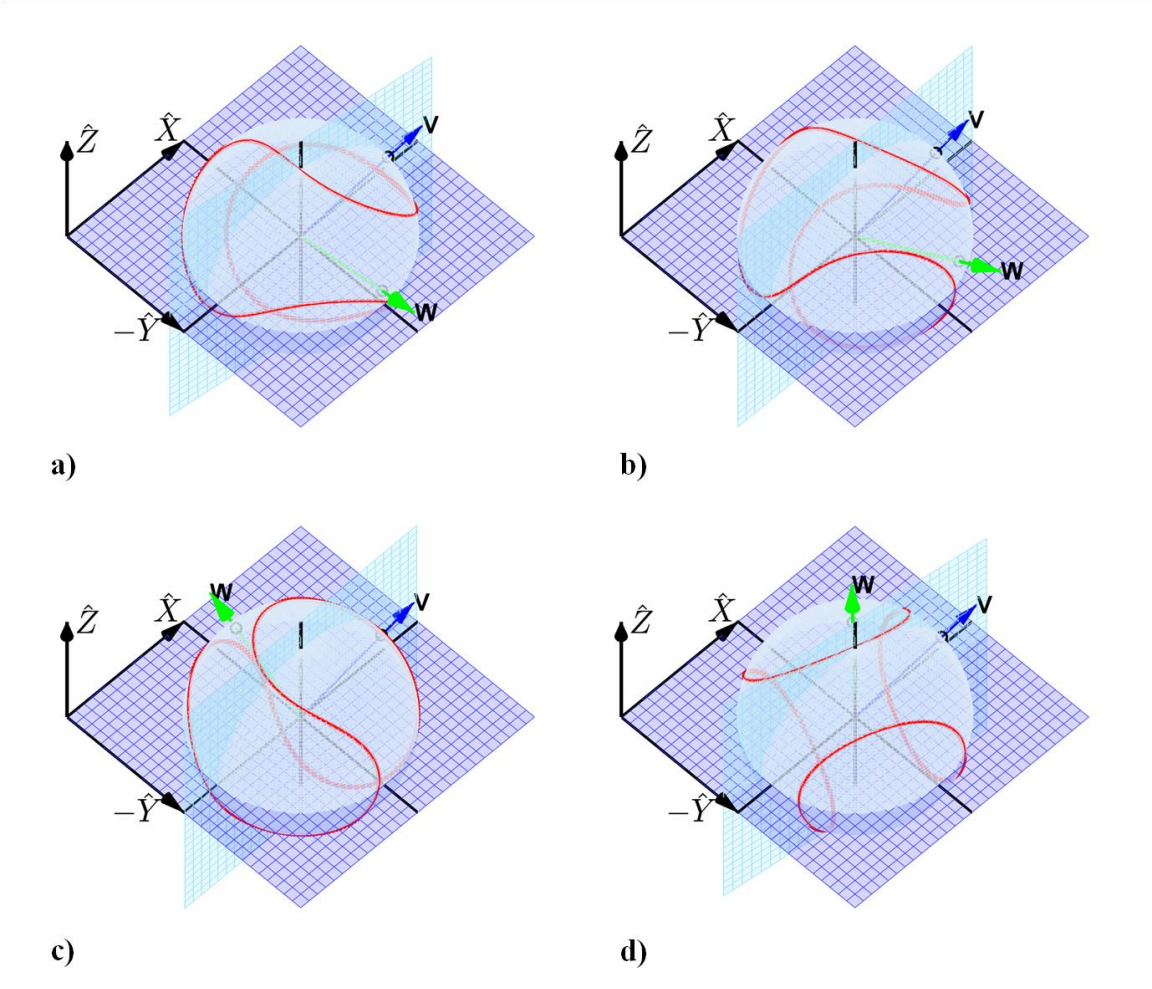

Figure 2.6: Linear (blue arrow denoted V) and angular (green arrow denoted W) velocity directions, and ball orientation at release for four typical baseball pitches: (a) fastball (four seam), (b) changeup, (c) curveball, and (d) slider.

These results demonstrate the potential of a promising new sensor technology for use in baseball and softball pitcher training applications. However, it is important to emphasize the fact that most baseball and softball pitchers will generate ball angular velocities that exceed the measurement range of the MEMS angular rate gyros used in this study. Luckily MEMS sensor manufacturers have recently recognized the need for gyros with extended measurement ranges (20,000 deg/s) and these devices are now available (e.g., Analog Devices ADXRS649, Norwood, MA, USA) thus enabling the methods presented herein to be used for pitcher training at all levels of baseball and softball.

2.4. Conclusions/Outlook

The miniaturized wireless IMU technology presented herein has the potential to provide a low cost, highly portable measurement system to support pitcher training right on the field of play. The IMU-embedded baseball and softball faithfully reproduce the release velocity of the ball compared to measurements made by motion capture methods for the speed ranges considered. In particular, the difference between the IMU-derived release velocity and the motion capture-derived velocity remains less than 5%. Moreover, the IMU directly measures the angular velocity of the ball at release for pitches that remain within the measurement range of the angular rate sensors. Finally, subsequent to completion of this study, high range angular rate gyros have now entered the marketplace (e.g., Analog Devices ADXRS649). The velocity and angular velocity at release enable one to easily distinguish pitch types and the degree to which that pitch type is thrown. This quick visual and quantitative feedback will allow pitching coaches to accurately measure, and thereby improve, pitching performance.

Chapter 3: Rotational Dynamics and Stability of Rigid Bodies in Free-Flight

3.1. Introduction

As noted in Chapter 2, the major obstacle preventing the use of inertial sensors for baseball and softball pitcher training is that highly skilled pitchers are able to spin the ball at rates outside the range measurable by most angular rate gyroscopes. With this as motivation, this chapter presents a method for identifying the free-flight angular velocity of a rigid body using just data from a tri-axial accelerometer. We begin by considering the theory governing the torque-free motion of a rigid body, which is a classical topic in rigid body dynamics; see, for example, [29–31]. Under torque-free conditions, the solution to Euler's equations for the angular velocity, expressible by Jacobi elliptic functions, satisfies two first integrals; namely constant rotational kinetic energy and constant magnitude of angular momentum. Rotations initiated close to the major or the minor principal axis generates a stable periodic precession about that axis. By contrast, unstable precession results from rotations initiated close to the intermediate axis. These results are elegantly revealed using the geometrical construction due to Poinsot [29–31,73], which considers the rolling without slipping of the inertia ellipsoid on the invariable plane. The path traced on the inertia ellipsoid by its contact point on the invariable plane, referred to as the polhode, describes the precession of the angular velocity vector in a body-fixed frame. The polhode may also be constructed from the intersection of the rotational kinetic energy ellipsoid and the angular momentum ellipsoid in angular velocity space [76]. This latter method will be demonstrated experimentally later in this paper.

In contrast to the well-established theory, direct experimental measurements of the dynamics of rigid bodies during torque-free or "free-flight" motion remain scarce.

This is not surprising given the significant experimental challenges in measuring free-flight dynamics in the laboratory in a non-invasive manner. One means to accomplish this is through camera-based motion analysis as used, for example, in optical motion tracking; see [77–84]. Bhat *et al.* [83] deduce the motion of a rigid body using single-camera optical motion tracking paired with global optimization techniques to minimize the error between video- and simulation-derived silhouettes. The algorithm, designed to converge to optimum values for initial position, orientation, velocity, and angular velocity, is especially sensitive to initial guesses due to many local minima in the error space. A variant of camera-based measurement introduced by Masutani *et al.* [84] estimates the free rotational motion of a rigid body from a sequence of gray-scale or distance images. This method, which relies heavily on the aforementioned closed-form solutions to Euler's equations, was evaluated using simulated motions in lieu of experiments. Fundamentally, camera-based motion analysis begins with noisy position data that must be differentiated numerous times to yield velocity, angular velocity, acceleration and angular acceleration data for the purpose of comparing with the equations of rigid body motion. The successive differentiation of real (i.e. noisy) position data leads to noise amplification and yields potentially error-prone comparisons with theory. Additionally, to avoid problems with aliasing, a camera must also capture images (and without occlusions) at frame rates well in excess of the angular velocity of the rigid body. These challenges fundamentally limit the utility of camera-based methods for analyzing the dynamics of a rigid body.

The use of MEMS inertial sensors to directly measure rigid body dynamics presents an attractive alternative to camera-based motion detection. Inertial sensors, consisting of accelerometers and angular rate gyros, directly measure the kinematic quantities governed by the Newton-Euler differential equations of motion. As one example, Lorenz [85] investigated the flight and attitude dynamics of a Frisbee ™ using a body-fixed instrumentation package containing two dual-axis MEMS accelerometers (among other sensors) to deduce the aerodynamic coefficients of the disk. Of keen interest in free-flight dynamics is the rotation of the rigid body as manifested in the angular velocity. Extending the measurement design in [85] to include three-axis angular rate sensing as well as three-axis acceleration sensing requires a complete inertial

measurement unit (IMU) for measuring the six degrees of freedom (6 dof) of a rigid body; see, for example, [75]. However, the added cost and the limited dynamic range and resolution of MEMS rate gyros have motivated numerous alternative "gyro free" IMU's for deducing the 6 dof [32,33,86–89]. The consensus is that twelve uni-axial accelerometers are required to form an over-determined set of acceleration data for the robust reconstruction of the angular velocity of a rigid body [86,87]. Special configurations of nine [88,89] and even six [32,33] uni-axial accelerometers can also succeed. Following [87] and [33], the optimal configuration of the six, nine, and twelve uni-axial accelerometers places them on the faces and/or the corners of a cube. The accuracy of the reconstructed angular velocity increases with cube dimension leading to dimensionally large, and thereby potentially invasive, sensor arrays. A significantly more compact solution follows from collocating angular rate gyros and accelerometers as achieved in the highly miniaturized IMU described herein.

In this paper, we contribute an elegant experimental method that reveals the free-flight dynamics of a rigid body. At the heart of our method is a highly miniaturized wireless IMU that incorporates three-axis sensing of acceleration and three axis sensing of angular velocity with a microcontroller and a low-power RF transceiver for wireless data transmission to a host computer. This IMU is used to directly measure acceleration and angular velocity during free-flight of a rigid body for comparison with theory. We directly observe the precession of the angular velocity vector in a body fixed frame through the construction of experimental polhodes. Rotations initiated close to the major, minor and intermediate principal axes closely obey predictions from classical theory. This experimental verification of classical free-flight dynamics enables us to demonstrate that the angular velocity vector of a body in force- and torque-free flight can be reconstructed via measurements from a single, tri-axial accelerometer. This simplification, which provides an inexpensive alternative to using angular rate gyros, runs counter to prior claims that a minimum of six independent accelerometer outputs are required for this purpose [32,33]. We open next with a description of the wireless IMU and the experimental procedure.

3.2. Methods

3.2.1. Wireless IMU and Experimental Procedure

Figure 3.1 illustrates what is believed to be the world's smallest wireless IMU enabling peer-to-peer communication to a host computer. This single-board design follows a lineage of larger, multi-board IMU designs [68,69,90,91] developed recently for novel sports training systems [92].

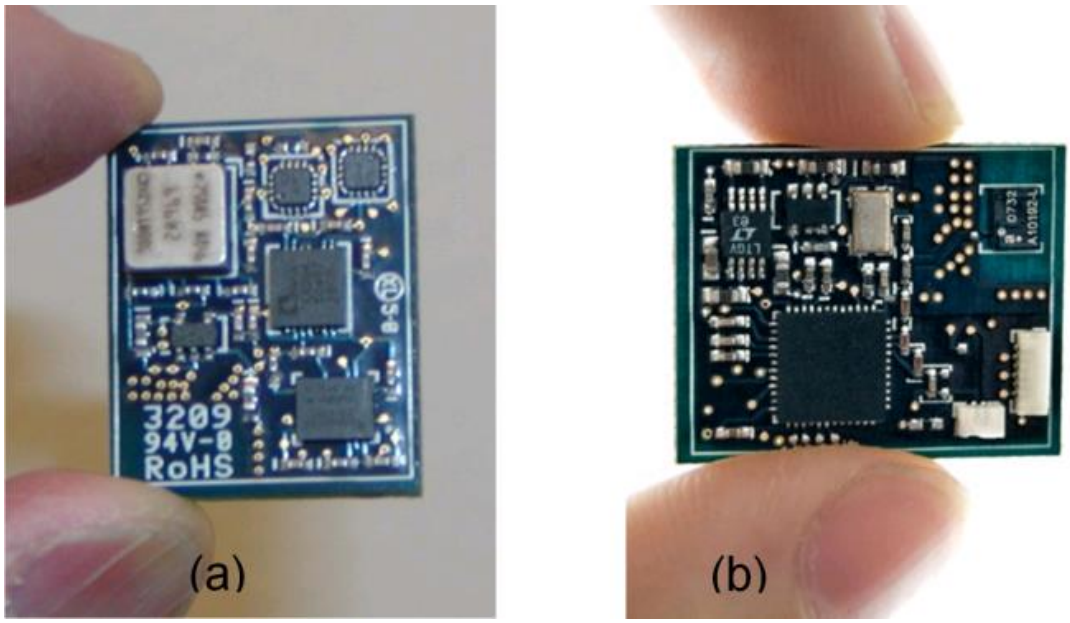

Figure 3.1: Photographs of highly miniaturized, wireless IMU. (a) analog circuit side with MEMS angular rate gyros and accelerometer, (b) digital circuit side with microprocessor, wireless transceiver, surface mount antenna, and connectors for battery power and firmware programming.

The two faces of the design separate analog and digital circuits. The MEMS inertial sensors, mounted on the analog circuit side (Fig. 3.1a), include a three-axis accelerometer, one dual-axis and one single-axis angular rate gyro, op-amps for signal conditioning, and off-chip components for filtering. The digital circuit side (Fig. 3.1b) includes a microprocessor for AD conversion, a low power RF transceiver, and a small surface mount antenna. Also visible are two small connectors (white, lower right) that

provide battery connection and the (one-time) connection to a host computer for uploading the firmware program to the microprocessor.

The minimized footprint (0.019 X 0.024 m) is achieved using a six-layer board containing two internal planes for interconnects and separate planes for power and ground. The assembled IMU board has a mass of 0.003 kg and the associated miniature lithium-ion battery adds a mere 0.0015 kg. The power draw remains below 25 mW and the battery tank yields four hours of uninterrupted use between recharging. The microprocessor performs 12-bit A/D conversion and, with the current firmware, provides 1 kHz sampling of all sensor channels. The low power RF transceiver (Nordic nRF24LE1) uses a proprietary RF protocol to transmit over a typical open-air range of 5 m with up to 18 m being achieved in low ambient RF environments. A USB-enabled receiver (not shown) enables data collection on a host (laptop) computer via custom data collection software. The device measurement range (and noise floor) includes accelerations up to 18 g (0.1 $m\,g/\sqrt{Hz}$) and angular rates up to 2000 deg/s (0.06 $\mathrm{deg/s}/\sqrt{Hz}$) with an overall measurement bandwidth of 400 Hz. The calibration procedure detailed in [68] is used to determine 24 calibration parameters (including scale factors, cross-axis sensitivity scale factors, and biases) for the IMU. This process ensures that the acceleration and angular rate measurements are resolved along a common set of orthogonal sense axes.

This miniaturized IMU, which currently supports a wide-range of human movement studies at the University of Michigan (e.g., athlete training, gait analysis, vestibular ocular reflex, knee and elbow injury detection, and surgeon training), is used herein to experimentally analyze the dynamics of a rigid body during free-flight. This class of motions is especially meaningful in the context of sports equipment (e.g. basketballs, baseballs, footballs, soccer balls, softballs, and the like) as well as aircraft, spacecraft and smart munitions, among other applications. The IMU above enables the direct measurement of rigid-body dynamics in a non-invasive (wireless) mode in laboratory or even classroom settings.

In our experiments, we seek to measure the rotational dynamics of the example rigid body illustrated in Fig. 3.2. This body is a uniform block of plastic (Delrin™) having dimensions 0.201 x 0.147 x 0.102 m and a mass of 4.36 kg. The block has readily

computed (non-degenerate) principal moments of inertia. The miniature IMU is fastened to the surface of the block in a corner position as shown. The mass of the IMU, when enclosed in a protective plastic casing, is approximately 0.014 kg, which represents a mere 0.3% perturbation to the mass of the block. Within this casing, the MEMS accelerometer is positioned at point *P* which is located by the known position vector $\vec{r}_{p/c}$ relative to the mass center *C* of the block. The illustrated body fixed frame $(\hat{e}_1, \hat{e}_2, \hat{e}_3)$, located at *C*, is aligned with the principal axes of the block as well as the sense axes of the accelerometer and angular rate gyros of the IMU. In particular, the $\hat{e}_1$ axis (or x_1 axis), the $\hat{e}_2$ axis (or x_2 axis), and the $\hat{e}_3$ axis (or x_3 axis) is aligned with the minor, intermediate, and major principal axes, respectively.

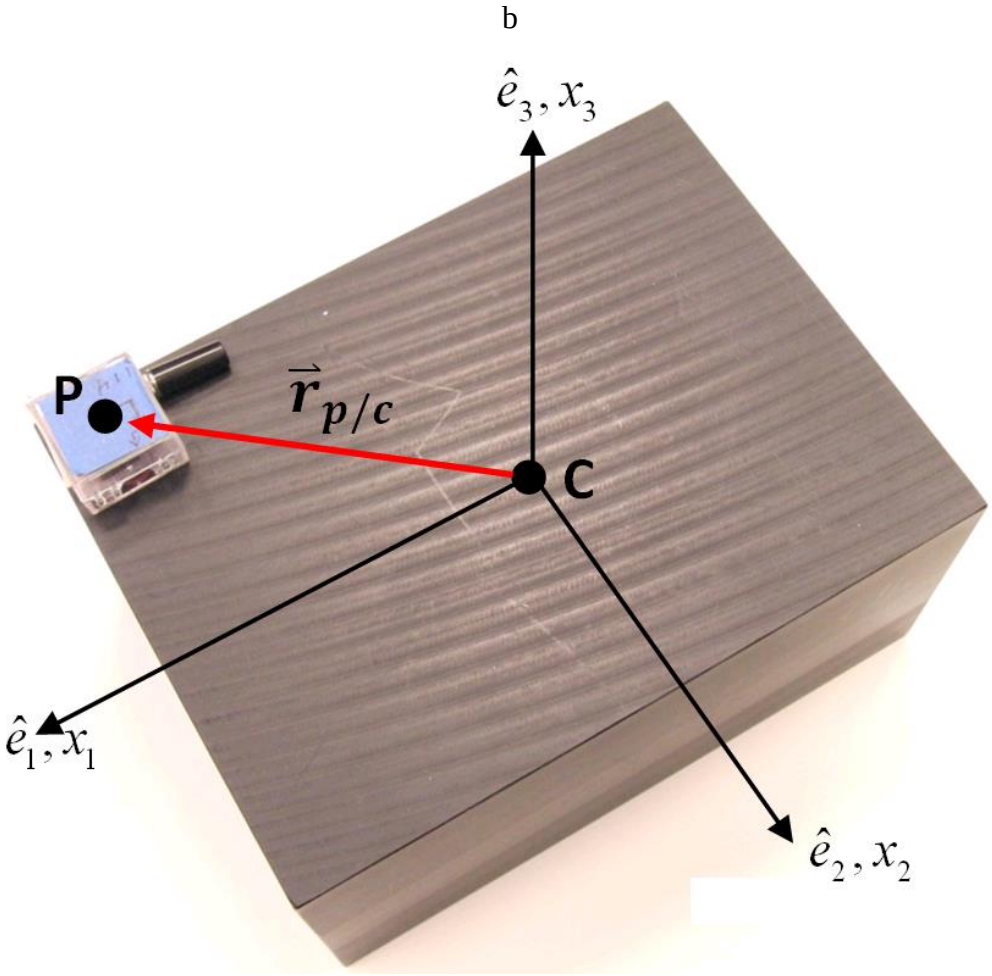

Figure 3.2: Photograph of example rigid body employed in experiments.

A simple experimental procedure is used to record the rigid body dynamics of the block during free flight. We first select the data sampling time (typically 5 seconds) via a custom data collection application. Next, we initiate data collection and then launch the block into free-flight by hand. In particular, we spin the block largely about a pre-selected axis prior to releasing it into free-flight. The IMU wirelessly transmits the acceleration data (for point *P*) and the block angular velocity data before release, during free-flight, and shortly after free-flight when the block is subsequently caught by hand.

3.2.2. Classical Analysis of Rigid Body Rotation during Free-Flight

As our interest lies in measuring rigid body rotation during free-flight, it is instructive to quickly review the classical behaviors predicted by theory. Assuming negligible aerodynamic moments, the angular momentum of the block about its center of mass remains constant as governed by Euler's equations under torque-free conditions [73]:

$$0 = I_C \dot{\vec{\omega}} + \vec{\omega} \times I_C \vec{\omega} \tag{3.1}$$

Here, I_C denotes the inertia tensor of the block about principal axes through its center of mass, and $\vec{\omega}$ denotes the angular velocity of the block resolved into components along the same (body-fixed) axes. Two constants of the motion arise (under the assumed torque-free conditions), namely the rotational kinetic energy (*T*) and the magnitude of the angular momentum ($\|\vec{H}\|$) [73] as given by

$$2T = \vec{\omega} \cdot \vec{H} = I_1 \omega_1^2 + I_2 \omega_2^2 + I_3 \omega_3^2 = const. \tag{3.2}$$

$$H^2 = \|\vec{H}\|^2 = (I_1 \omega_1)^2 + (I_2 \omega_2)^2 + (I_3 \omega_3)^2 = const. \tag{3.3}$$

where I_i and ω_i (for *i=1,2,3*) denote the principal moments of inertia and the angular velocity components, respectively.

The form of the solution to eq. (3.1), as summarized in Table 3.1, depends on the intermediate principal moment of inertia I_2 and the constants of the motion *T* and *H*; see, for example [93] or [94]. In Table 3.1, additional constants are defined by

$$z_1 = \frac{H^2 - 2T(I_2 + I_3)}{I_2 I_3} \qquad z_3 = \frac{H^2 - 2T(I_1 + I_2)}{I_1 I_2}$$
$$z_2 = \frac{H^2 - 2T(I_1 + I_3)}{I_1 I_3} \qquad s_i = \text{sign}\left[\omega_i(0)\right] \tag{3.4}$$

and cn, sn, and dn denote Jacobi elliptic functions. The constant t_0 is evaluated by satisfying the initial conditions for $\omega(0)$.

In general, the rigid body will precess during free-flight and the precession is stable for rotations initiated close to the major and minor axes and unstable for rotations initiated close to the intermediate axis. The precession and stability can also be observed geometrically using Poinsot's construction; see, for example, [29–31]. Following the development in [76], re-casting the constants of the motion defined in eqs. (3.2) and (3.3)

$$\frac{\omega_3^2}{(2T/I_3)} + \frac{\omega_2^2}{(2T/I_2)} + \frac{\omega_1^2}{(2T/I_1)} = 1 \tag{3.5}$$

$$\frac{\omega_3^2}{(H/I_3)^2} + \frac{\omega_2^2}{(H/I_2)^2} + \frac{\omega_1^2}{(H/I_1)^2} = 1 \tag{3.6}$$

yields two ellipsoidal surfaces on which the solution evolves in the space of the angular velocity components. The curve defined by their intersection is the path traced by the angular velocity vector in this space. As mentioned earlier, this curve is the polhode and it can be readily constructed directly from the IMU data as demonstrated in the following results.

$H^2/2T > I_2$	$H^2/2T < I_2$
$p = \sqrt{z_1 - z_2} \quad k = \sqrt{z_3 - z_2}\, p^{-1}$	$p = \sqrt{z_3 - z_2} \quad k = \sqrt{z_1 - z_2}\, p^{-1}$
$\omega_1 = s_1 \sqrt{\frac{H^2 - 2T \cdot I_3}{I_1(I_1 - I_3)}} \mathrm{dn}\left[p(t - t_0), k \right]$	$\omega_1 = s_1 \sqrt{\frac{H^2 - 2T \cdot I_3}{I_1(I_1 - I_3)}} \mathrm{cn}\left[p(t - t_0), k \right]$
$\omega_2 = s_2 \sqrt{\frac{H^2 - 2T \cdot I_1}{I_2(I_2 - I_1)}} \mathrm{sn}\left[p(t - t_0), k \right]$	$\omega_2 = s_2 \sqrt{\frac{H^2 - 2T \cdot I_3}{I_2(I_2 - I_3)}} \mathrm{sn}\left[p(t - t_0), k \right]$
$\omega_3 = s_3 \sqrt{\frac{H^2 - 2T \cdot I_1}{I_3(I_3 - I_1)}} \mathrm{cn}\left[p(t - t_0), k \right]$	$\omega_3 = s_3 \sqrt{\frac{H^2 - 2T \cdot I_1}{I_3(I_3 - I_1)}} \mathrm{dn}\left[p(t - t_0), k \right]$

$$H^2/2T = I_2$$

$$p = \sqrt{z_1 - z_2}$$

$$\omega_1 = s_1 \sqrt{\frac{2T(I_2 - I_3)}{I_1(I_1 - I_3)}} \operatorname{csch}\left[p(t - t_0) \right]$$

$$\omega_2 = s_2 \sqrt{\frac{2T}{I_2}} \tanh\left[p(t - t_0) \right]$$

$$\omega_3 = s_3 \sqrt{\frac{2T(I_1 - I_2)}{I_3(I_1 - I_3)}} \operatorname{csch}\left[p(t - t_0) \right]$$

Table 3.1: Closed-form solution to Euler's equation (3.1) as determined by the constants of the motion H and T.

3.3. Results and Discussion

We open our discussion with a quantitative comparison of predicted versus measured free-flight dynamics. We compare experimental and theoretical time-histories of the angular velocity components as well as their companion polhodes. We then turn attention to a much simplified design employing solely a single, tri-axial accelerometer in lieu of a complete IMU. In so doing, we demonstrate a new and accurate method to reconstruct the angular velocity of a rigid body in free-flight. We accomplish this by first presenting the measurement theory and then by comparing experimental predictions of angular velocity from the accelerometer to those obtained via the complete IMU.

3.3.1. Comparison of Experimental versus Predicted Rigid Body Rotation

As introduced in Section 3.2, the miniature wireless IMU enables the direct sensing of rigid body rotation and thereby the direct confirmation of classical rigid body behaviors. Figure 3.3 illustrates typical experimental data recorded for one trial. Figures 3.3(a) and 3.3(b) illustrate the magnitude of the acceleration of point *P* and the magnitude of the angular velocity, respectively as functions of time. Three distinct phases of the motion are clearly identifiable and they are referred to as the *throw*, *free-flight*, and *catch* phases. The block is spun up from rest during the throw, released into free-flight at the transition between the throw and free-flight, and brought back to rest during the catch. At the start of the throw, the angular velocity is zero and the magnitude of the acceleration remains 1g[1] confirming that the block is at rest. Following a substantial spin up near the end of the throw, the magnitude of the angular velocity remains near-constant (approximately 1570 deg/s) during the short (0.5 second) free-flight phase. This example trial illustrates stable rotation close to the minor axis and therefore the block exhibits a stable precession about that axis as discussed later in the context of Figs. 3.4 and 3.5. Also shown are the rotational kinetic energy *T* and the magnitude of the angular momentum about the center of mass $\left\|\vec{H}\right\|$ in Figs. 3.3(c) and 3.3(d), respectively. Note that during free-flight, *T* decreases by only 1.2 % and $\left\|\vec{H}\right\|$ decreases by a mere 0.5 % confirming the negligible influence of aerodynamic moments in the experiment.

[1] Note that the MEMS accelerometer detects acceleration down to DC and thus it also measures gravity.

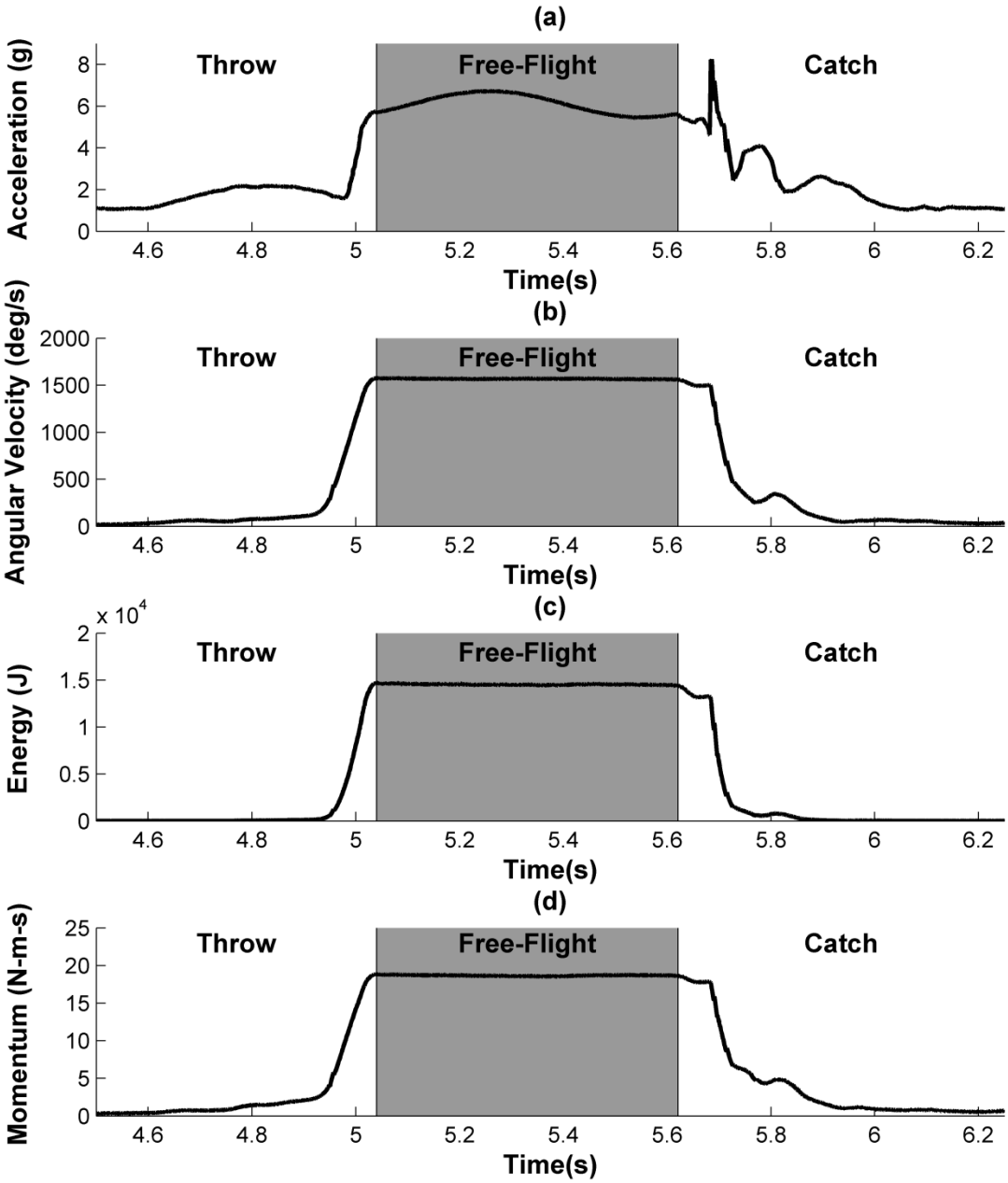

Figure 3.3: Example time histories of the measured (a) magnitude of the acceleration of point P, (b) magnitude of the angular velocity, (c) the rotational kinetic energy, and (d) magnitude of angular momentum about center of mass. The throw, free-flight and catch phases are noted. Example trial for rotation initiated nearly about minor axis.

We now turn attention to a detailed comparison of experimental and theoretical results for free-flight dynamics. Figure 3.4 illustrates results for rotation initiated close to the major axis (Fig. 3.4a), the intermediate axis (Fig. 3.4b), and the minor axis (Fig.

3.4c). In each case, experimental (solid) and theoretical (dashed) time histories are plotted for the three angular velocity components as well as their vector magnitude (black). Recall that the components ω_1 (blue), ω_2 (green) and ω_3 (red) are aligned with the major, intermediate and minor axes, respectively. The illustrated experimental data is low-pass filtered using a 100 Hz cut-off frequency to remove modest measurement noise. The theoretical results are computed from the solutions reported in Table 3.1 upon using the measured angular velocity at the start of free-flight as the initial condition for the remainder of the free-flight phase.

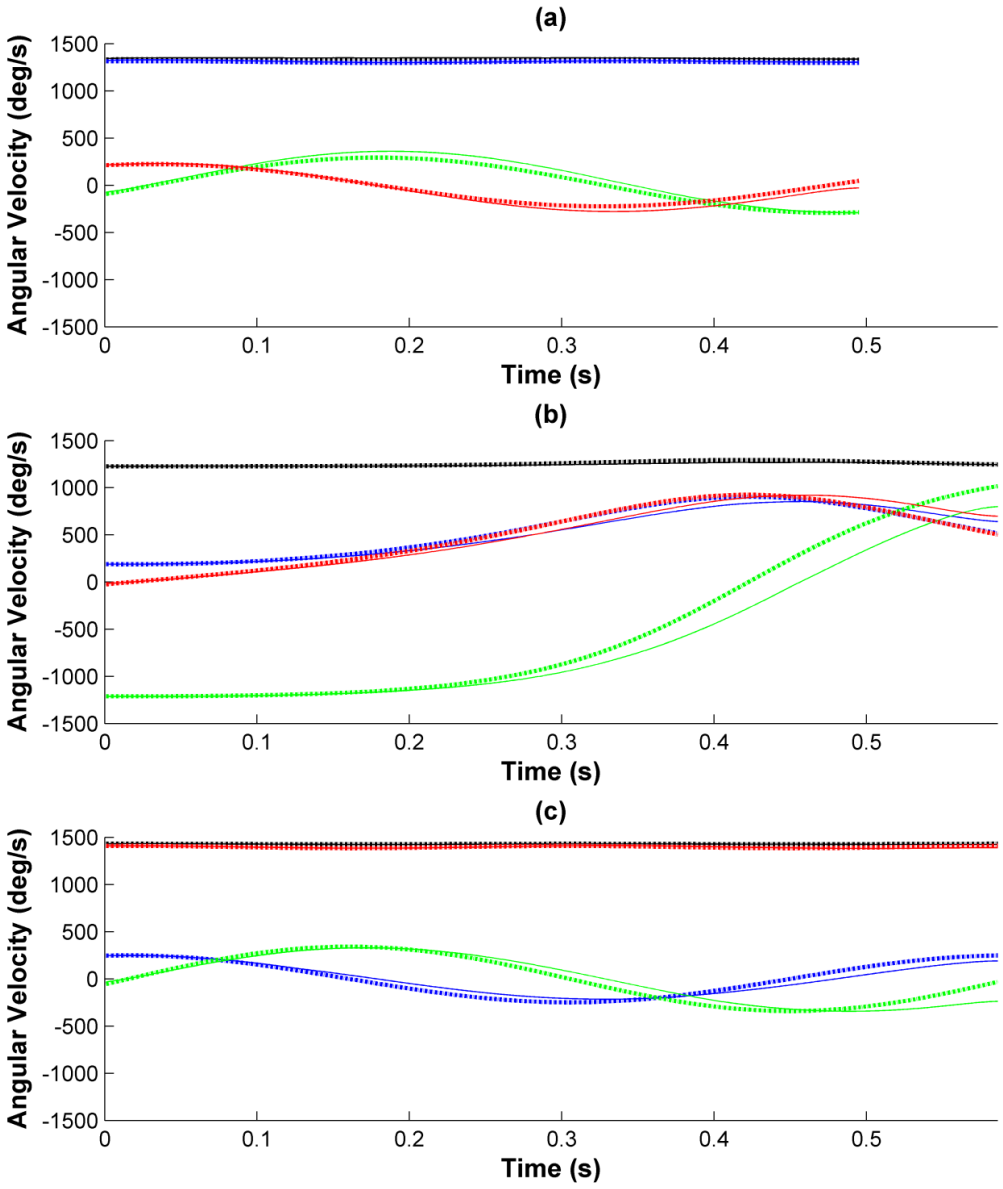

Figure 3.4: Measured (solid) and calculated (dashed) angular velocity vector magnitude (black) and components for rotations initiated about the major (a), intermediate (b), and minor (c) axes. The blue, green, and red curves correspond to components about the major (ω_1), intermediate (ω_2), and minor axes (ω_3), respectively.

The results of Fig. 3.4 clearly confirm expected free-flight behaviors. For rotation initiated near the major (minor) axis as illustrated in Fig. 3.4a (Fig. 3.4c), the block rotates in a stable manner with a large, near-steady angular velocity component about the

major (minor) axis. Moreover, the two "off-axis" components of angular velocity remain small and exhibit small periodic oscillations. The oscillation frequencies match those predicted by linear theory[2] to within 0.8% (8.3%) for the illustrated case of rotation about the major (minor) axis. In contrast, for rotation initiated near the intermediate axis as illustrated in Fig. 3.4b, the block experiences unstable rotation as evidenced by the large, diverging precession.

[2] For example, refer to [73]. This classical analysis reveals that the "off-axis" components of angular velocity will oscillate with frequency $\omega_n = \Omega\sqrt{(I_1 - I_3)(I_2 - I_1)/I_3 I_2}$ or $\omega_n = \Omega\sqrt{(I_1 - I_3)(I_3 - I_2)/I_1 I_2}$ for rotations about the major and minor axes respectively, where Ω is the magnitude of angular velocity component about the major or minor axis.

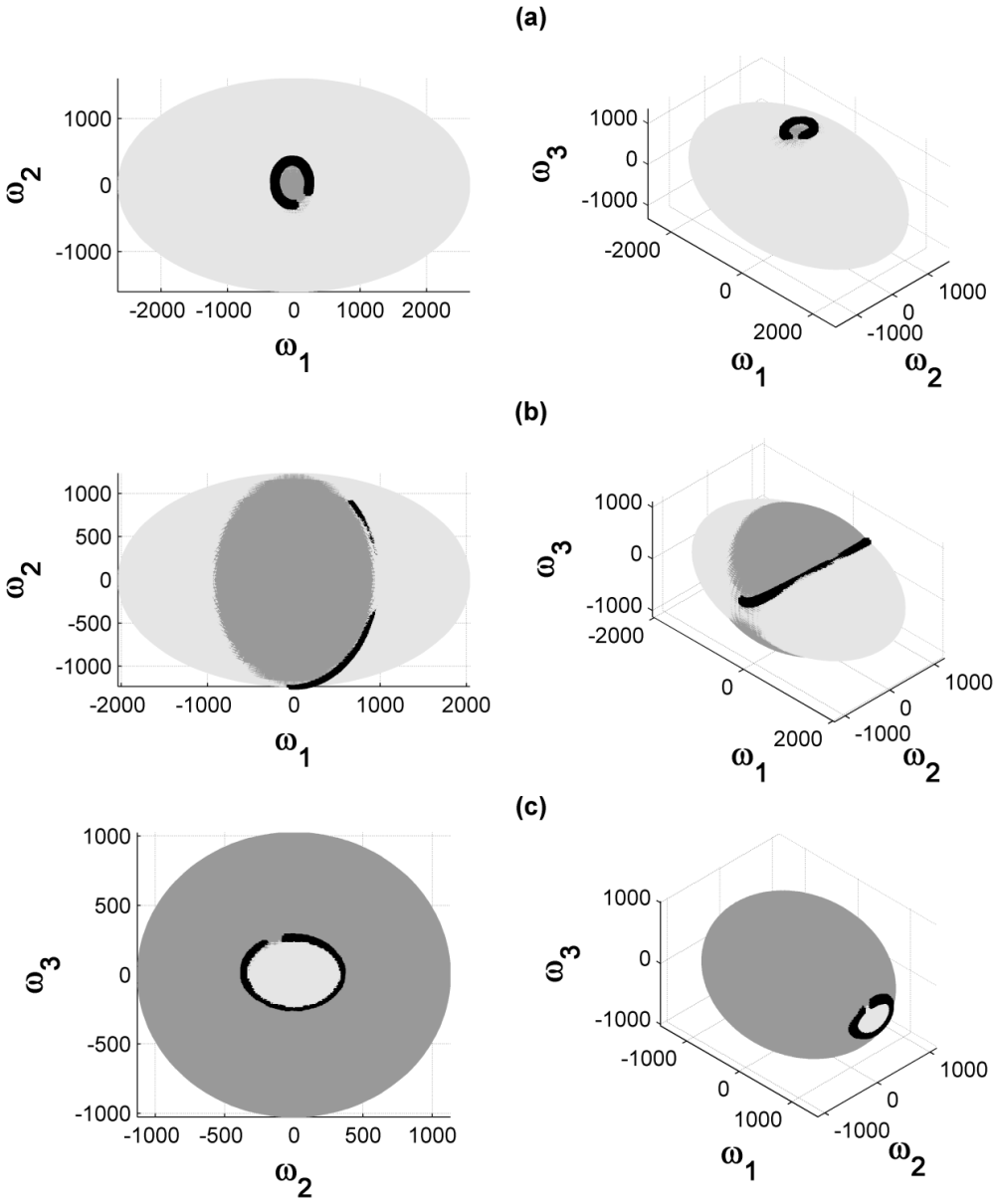

Figure 3.5: Experimental demonstration of the polhode for rotations initiated close to the major (a), intermediate (b), and minor (c) principal axes. The measured angular velocity during the entire free-flight phase (black, scale in deg/s), closely follows the polhode defined by the intersection of the ellipsoids.

The stable and unstable rotations are elegantly described geometrically upon construction of the associated polhodes as illustrated in Fig. 3.5. Shown in this figure are

the ellipsoids of constant rotational kinetic energy (dark gray surface) and constant angular momentum magnitude (light gray surface) for the case of rotation initiated near the major axis (Fig. 3.5a), the intermediate axis (Fig. 3.5b), and the minor axis (Fig. 3.5c). These ellipsoids follow from eqs. (3.5) and (3.6) upon using the measured angular velocity at the start of free-flight as the initial conditions. Following [76], the intersection of the two ellipsoids defines the curve in angular velocity space on which the free-flight dynamics evolve. This fact is confirmed upon superimposing the measured angular velocity from the wireless IMU (black curves) over the duration of the free-flight phase. For rotations initiated close to either the major or the minor axis, small-amplitude periodic precession arises and the angular velocity vector correspondingly generates a stable orbit centered about the associated principal axis; refer to Figs. 3.5a and 3.5c. In contrast, for rotation initiated near the intermediate axis, the precession describes a large and diverging (unstable) response. These results provide clear and direct support of the classical theory reviewed above.

We now establish the quantitative agreement between theory and experiment. To this end, we introduce a relative error measure for each angular velocity component ω_j

$$\varepsilon_{rms,j} = \sqrt{\frac{1/N \sum_{i=1}^{N} \left(\omega_{ji} - \tilde{\omega}_{ji}\right)^2}{1/N \sum_{i=1}^{N} \left\|\vec{\omega}_i\right\|^2}} \tag{3.7}$$

This relative error represents the root mean square error between the measured ($\tilde{\omega}_j$) and theoretical (ω_j) angular velocity components normalized by the theoretical root mean square angular velocity magnitude ($\|\vec{\omega}\|$) for all (N) samples during the free-flight phase. The theoretical angular velocity was again computed using the solutions of Table 1 upon first introducing the initial angular velocity measured by the IMU at the start of the free-flight phase. This error analysis was conducted for a total of 16 trials. The trials included two clockwise and two counter-clockwise rotations about each of the three principal axis and four additional rotations about arbitrarily selected axes. The relative error, defined in eq. (3.7), was calculated for each angular velocity component for each trial, and the average for all 16 trials is reported in Table 3.2 as a percentage.

j	1	2	3
$\varepsilon_{rms,j}(\%)$	3.0	5.8	4.6

Table 3.2: Quantitative comparison of theoretical and experimental angular velocity components. Relative root-means-square error for each angular velocity component averaged over all 16 trials. The error measure is given by eq. (7) and reported in this table as a percentage.

Reflecting on the results of Table 2 and the three example trials of Fig. 3.4, we now understand that the wireless IMU replicates the expected theoretical angular velocity components to within 6% on average for all 16 trials. This good quantitative agreement confirms that any experimental errors introduced in the measured block inertia (i.e. *m*, I_1, I_2, I_3), in the IMU measurements (e.g., gyro bias, noise, calibration errors, and misalignment between sense axes and the block's principal axes), and in the assumption of torque-free motion (i.e. negligible aerodynamic moments) are reasonably small.

3.3.2. Angular Velocity Reconstructed from a Single Tri-axial Accelerometer

The data reported above was obtained using the complete IMU including the angular rate gyros. While the angular rate gyros yield highly accurate measurements of angular velocity, they are relatively expensive compared to the embedded tri-axial accelerometer. The addition of angular rate gyros obviously creates a larger volume design. Moreover, commercial MEMS rate gyros have limited range (e.g., typical ranges today are 6000 deg/s and less). Thus, the restrictions incurred by rate gyro cost, size and measurement range may preclude their use in high-volume commercial applications such as instrumented basketballs, soccer balls, baseballs, golf balls, footballs, softballs, and the like. This realization naturally leads to the question of whether it is possible to arrive at the same accurate measurements of angular velocity without the use of angular rate gyros for free-flight dynamics. We present below an answer to this question beginning with the measurement theory and then proceeding to the experimental evidence.

In reference to Fig. 3.2, the acceleration of point P (the center of the tri-axial accelerometer) on the rigid body, can be written in terms of the acceleration of the mass center *C* through

$$\vec{a}_p = \vec{a}_c + \dot{\vec{\omega}} \times \vec{r}_{p/c} + \vec{\omega} \times \left(\vec{\omega} \times \vec{r}_{p/c} \right) \tag{3.8}$$

where $\vec{a}_c$ denotes the acceleration of the mass center, $\vec{r}_{p/c}$ is again the position of *P* relative to *C*, and $\vec{\omega}$ and $\dot{\vec{\omega}}$ are, respectively, the angular velocity and angular acceleration of the rigid body. The acceleration measured by the MEMS accelerometer is the vector sum of the acceleration of point *P* minus the acceleration due to gravity [32] as given by

$$\vec{a}_s = \vec{a}_p + g\hat{K} \tag{3.9}$$

where *g* denotes gravity and $\hat{K}$ is a unit vector directed upwards. For the case of a rigid body in free-flight, the acceleration of the mass center is simply

$$\vec{a}_c = -g\hat{K} \tag{3.10}$$

assuming negligible aerodynamic drag. Substitution of eqs. (3.9) and (3.10) into eq. (3.8) yields

$$\vec{a}_s = \dot{\vec{\omega}} \times \vec{r}_{p/c} + \vec{\omega} \times \left(\vec{\omega} \times \vec{r}_{p/c} \right) \tag{3.11}$$

where it is obvious that the accelerometer output depends on the rotational dynamics of the rigid body as governed by the torque-free form of Euler's equations. Solving eq. (3.1) for $\dot{\vec{\omega}}$ and substituting this result into eq. (3.11) yields

$$\vec{a}_s = \left[-I_c^{-1} \left(\vec{\omega} \times I_c \vec{\omega} \right) \right] \times \vec{r}_{p/c} + \vec{\omega} \times \left(\vec{\omega} \times \vec{r}_{p/c} \right) \tag{3.12}$$

which explicitly demonstrates that the output of the accelerometer alone can be used to deduce the angular velocity. Introducing the components $\vec{a}_s = \begin{bmatrix} a_{s1} & a_{s2} & a_{s3} \end{bmatrix}^T$ and $\vec{r}_{p/c} = \begin{bmatrix} r_1 & r_2 & r_3 \end{bmatrix}^T$ into eq. (3.12) yields the component equivalent

$$\begin{bmatrix} a_{s1} \\ a_{s2} \\ a_{s3} \end{bmatrix} = \begin{bmatrix} -\left(\omega_2^2 + \omega_3^2\right) & \left(1 - I_c\right)\omega_1\omega_2 & \left(1 + I_b\right)\omega_1\omega_3 \\ \left(1 + I_c\right)\omega_1\omega_2 & -\left(\omega_1^2 + \omega_3^2\right) & \left(1 - I_a\right)\omega_3\omega_2 \\ \left(1 - I_b\right)\omega_1\omega_3 & \left(1 + I_a\right)\omega_3\omega_2 & -\left(\omega_1^2 + \omega_2^2\right) \end{bmatrix} \begin{bmatrix} r_1 \\ r_2 \\ r_3 \end{bmatrix} \tag{3.13a}$$

or

$$\vec{a}_s = \underline{B}\left(\vec{\omega}\right)\vec{r}_{p/c} \tag{3.13b}$$

in which $I_a = \left(I_2 - I_3\right)/I_1$, $I_b = \left(I_3 - I_1\right)/I_2$, and $I_c = \left(I_1 - I_2\right)/I_3$. Equation (3.13) provides three quadratic equations for solution of the three unknown angular velocity components from the measured acceleration components of point *P*.

Moreover, the solution for $\vec{\omega}$ must satisfy the two constants of the motion given by eqs. (3.2) and (3.3). These additional equations, though not independent of the above result that embeds Euler's equations, are advantageous in the computation of $\vec{\omega}$. In particular, eq. (3.13) with eqs. (3.2) and (3.3) yield an over-determined set of five equations in the three unknowns ($\omega_1, \omega_2, \omega_3$) enabling a robust least squares solution, provided the values of the constants of the motion are known *a priori*.

To compute these constants, we first seek the initial conditions for the angular velocity and the two constants of the motion as represented by the set ($\omega_1(0), \omega_2(0), \omega_3(0), 2T_0, H_0^2$). To this end, we numerically solve eq. (3.13) with eqs. (3.2) and (3.3) as a set of five equations in these five unknowns using the measured values of ($a_{s1}(0), a_{s2}(0), a_{s3}(0)$) at the start of the free-flight phase. This set of nonlinear equations admits multiple solutions which is a well documented issue; see, for example [32,86,89,95,96]. The problem, illustrated by eq. (3.11), is that the expression for $\vec{a}_s$ is quadratic in $\vec{\omega}$ which renders the sign of the angular velocity vector (though not the direction) ambiguous. The sign can be readily determined by simple observation during the experiment.

For any other time *t* during the free-flight phase, we compute the least-squares solution for $\vec{\omega}(t)$ from the five equations (3.13) with (3.2) and (3.3). For each sample i, we seek the solution for $\vec{\omega}$ that minimizes the cost function

$$J_i = \left(\frac{\left\| \vec{a}_{s,i} - \underline{B}(\vec{\omega}) \vec{r}_{p/c} \right\|}{\sum_{i=1}^{N} \left\| \vec{a}_{s,i} \right\| / N} \right)^2 + \left(\frac{2T_0 - 2T_i}{2T_0} \right)^2 + \left(\frac{H_0^2 - \left\| \vec{H}_i \right\|^2}{H_0^2} \right)^2 \tag{3.14}$$

where $\vec{a}_{s,i}$ is the sampled accelerometer output, and N is the total number of samples. The solution is found numerically using the *lsqnonlin* function in MATLAB™ and angular velocity components from the last time step as an initial guess. The *lsqnonlin* function employs a trust-region method for numerical, unconstrained, nonlinear, minimization problems [97].

The components of angular velocity, as reconstructed from a single tri-axial accelerometer, reliably predict those measured by the angular rate gyros. Evidence for this claim is presented in Fig. 3.6 which directly compares the reconstructed versus

measured angular velocity. Results are presented for three example trials where rotation is initiated nearly about the major (Fig. 3.6a), the intermediate (Fig. 3.6b), and the minor (Fig. 3.6c) axes. Both the angular velocity components as well as the magnitude of the angular velocity vector are illustrated. Inspection of these results reveals excellent agreement thereby demonstrating that a single, tri-axial accelerometer can be employed to accurately reconstruct the angular velocity during free-flight. The accuracy is summarized quantitatively in Table 3.3 which reports the average relative rms error[3] for the 16 trials previously considered. The errors, which remain less than 2% for all three angular velocity components, provide convincing evidence in support of our claim.

[3] The error measure is again given by (3.7) where the angular velocity measured by the angular rate gyros is now used as the "truth" data.

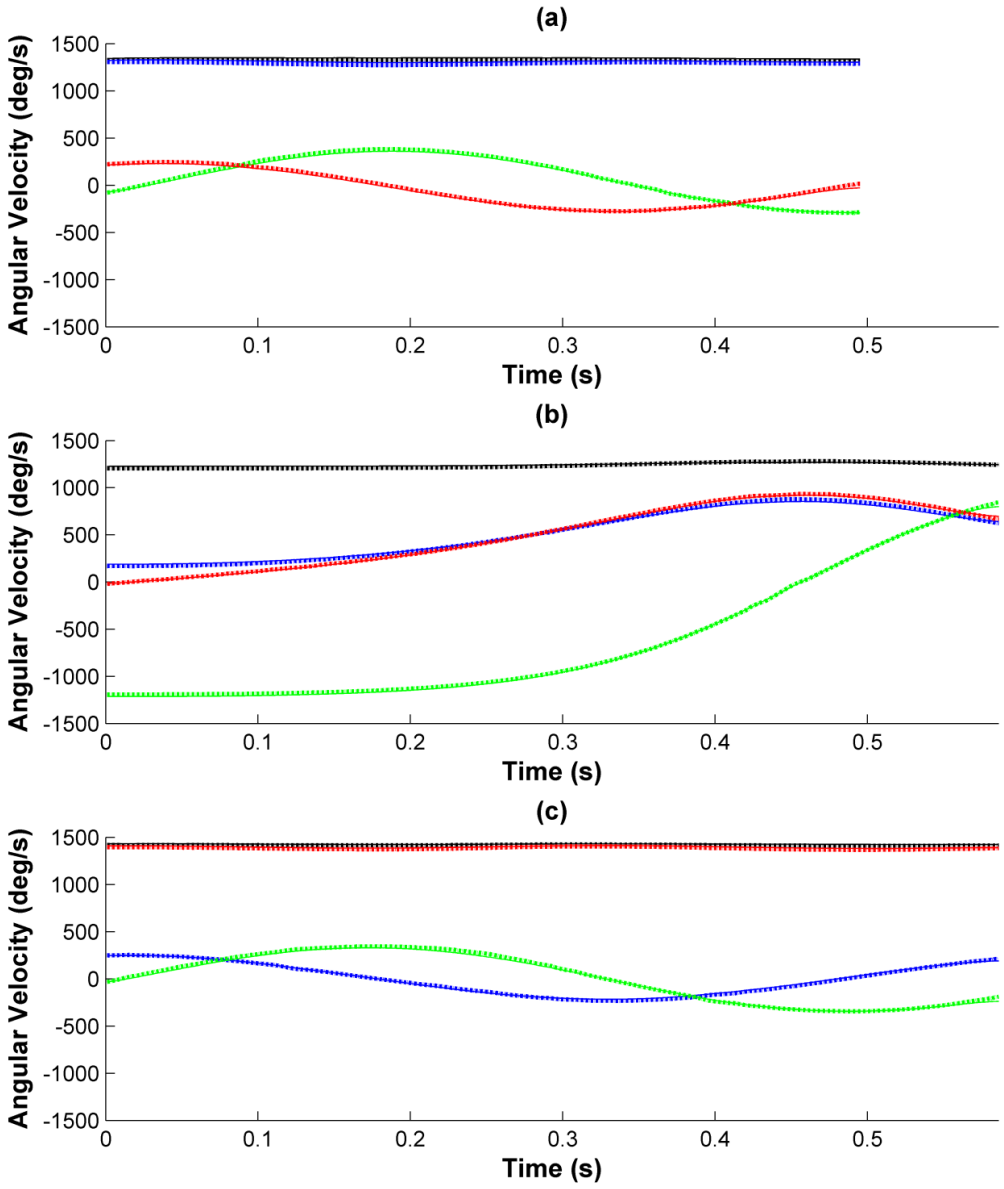

Figure 3.6: Measured (solid) and reconstructed (dashed) angular velocity magnitude (black) and components for rotations initiated nearly about the major (a), intermediate (b), and minor (c) axes. The blue, green, and red curves correspond to components about the major (ω_1), intermediate (ω_2), and minor axes (ω_3), respectively.

j	1	2	3
$\varepsilon_{rms,j}(\%)$	1.2	1.2	1.3

Table 3.3: Relative root-mean-square error for angular velocity components reconstructed using a single, tri-axial accelerometer as compared to those measured directly from the angular rate gyros.

3.4. Summary and Conclusions

The novel, miniature wireless MEMS IMU presented herein provides a non-invasive and highly portable means to measure the dynamics of a rigid body. The IMU incorporates three-axis sensing of acceleration and three-axis sensing of angular velocity with a microcontroller and an RF transceiver for wireless data transmission to a host computer. The small sensor footprint (0.019 X 0.024 m) and mass (0.005 kg including battery) enables its use in rather broad applications including, for example, human motion analysis, sports training systems, and education/learning of rigid body dynamics. Specific to this paper, we demonstrate how this novel sensor can be used in laboratory or classroom settings to accurately measure the dynamics of a rigid body in free-flight.

The experiments consider an example rigid body that is spun up by hand and then released into free-flight. The resulting rotational dynamics measured by the angular rate gyros are carefully benchmarked against theoretical results from Euler's equations. This comparison reveals that differences between measurement and theory remain less than 6%. Moreover, experimentally constructed polhodes elegantly illustrate the expected stable precession for rotations initiated close to the major or minor principal axes and the unstable precession for rotations initiated close to the intermediate axis.

Finally, we present a single, tri-axial accelerometer as an alternative to using a full IMU for deducing the angular velocity of a rigid body during free-flight. This simpler alternative, which addresses restrictions incurred by rate gyro cost, size and measurement range, may enable high-volume commercial applications such as instrumented basketballs, soccer balls, baseballs, golf balls, footballs, softballs, and the like. A measurement theory is presented for reconstructing the angular velocity of the body during free-flight from acceleration signals which is then validated experimentally. The experimental results confirm that the angular velocity can be reconstructed with small

errors (less than 2%) when benchmarked against direct measurements using angular rate gyros.

Chapter 4: The Velocity of a Running Athlete

4.1. Introduction

This chapter extends the method for predicting ball velocity presented in Chapter 2 to predicting athlete speed non-invasively on the field of play. The presented technique complements a growing interest in employing miniaturized inertial sensors and GPS technology to monitor athlete performance [34–37]. Recent products exploit these technologies to track performance metrics (e.g. speed, acceleration, load, etc.) on the field of play [34,39,41]. Two such designs incorporate sensor modules in clothing, holding the modules tightly against the athlete's torso and away from the extremities (hands and feet) used for play. These designs specifically target outdoor sports, like soccer, rugby, and Australian and American football, where a fusion of IMU and GPS data is used to estimate athlete speed [38,41]. However, the lack of GPS signals in indoor arenas renders these sensor fusion methods useless for sports such as basketball [42].

An alternative to sensor-fusion techniques is to estimate running speed based solely on data from inertial sensors, namely accelerometers and angular rate gyros. One approach employs acceleration data alone [43–46]. For example, [43] and [46] develop a linear model to identify athlete speed from the stride frequency detected with a torso mounted accelerometer. However, doing so requires a subject specific calibration that relates stride frequency to speed. Alternatively, the studies [44] and [45] utilize neural networks to establish the relationship between running speed and torso acceleration. However, neural networks require training, and the network presented in [44] also requires subject height and weight as input while that in [45] requires a heel mounted accelerometer.

A second method for determining running speed employs direct integration of measured acceleration [47,48]. For example, a method for determining running speed based on integration of the acceleration measurements from a shank-mounted IMU is presented in [47]. The resulting velocity estimate is subject to what is referred to as drift error [61,75] caused by integrating small, time varying errors in the acceleration and angular velocity data. In [47,48] this drift is estimated by assuming the shank behaves like a one degree-of-freedom inverted pendulum pivoting about the ankle joint during the stance phase. Assuming that the location of the IMU relative to the ankle is known, this allows for an independent estimate of velocity and therefore a correction for drift. However, this method requires accurate knowledge of the IMU's location relative to the center of rotation of the ankle and it further assumes planar shank motion.

This study improves upon the methods above by yielding estimates of athlete speed from a single torso-mounted IMU without subject-specific calibration or additional positional data (GPS). Doing so enables accurate and non-invasive speed predictions on the field of play, whether outdoors or indoors. The speed estimates from this new method are compared to those determined from video based motion capture (MOCAP). We open with a description of the experiment.

4.2. Methods

This study presents IMU- and MOCAP-based speed predictions for 40 trials of a single subject. The data set is composed of 10 trials each of straight-line walking, jogging, and running and 10 trials of running a predefined zig-zag course. For each trial, the subject begins at rest, completes a specified course, stands still momentarily, repeats the course, and finishes the trial at rest. For the straight-line walking ("Walk"), jogging ("Jog"), and running ("Run") trials, the course is defined as a straight path between two cones, 5 m apart (Fig. 4.1A). For the zig-zag running trials ("Zig-zag"), the course is defined by a zig-zag path connecting 6 cones within the 5m by 5m MOCAP capture volume (Fig. 4.1B). Example paths for each type of trial are illustrated in Fig. 4.1 as revealed by the position of a torso-mounted marker; refer to Fig. 4.2A.

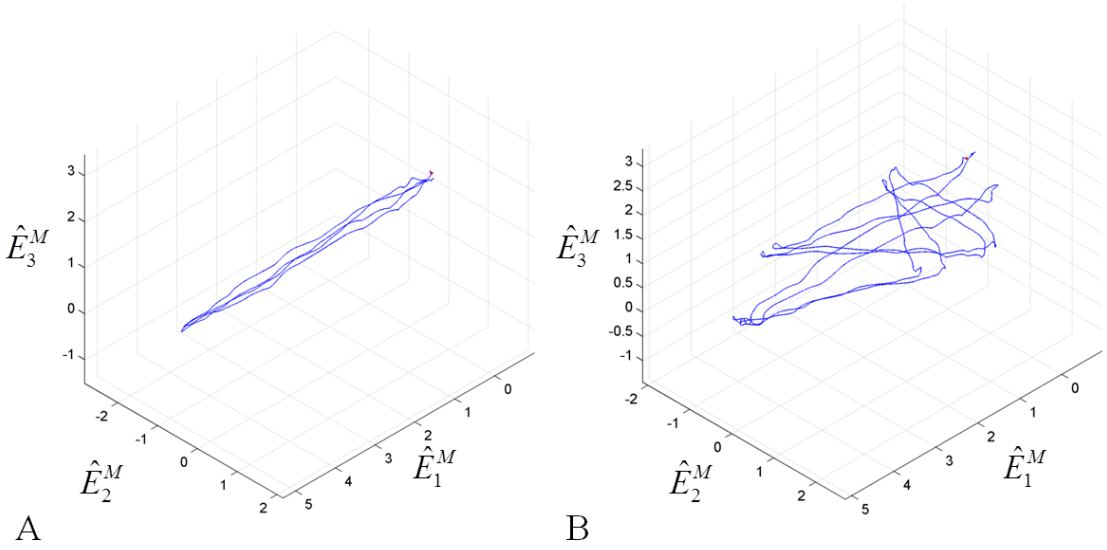

Figure 4.1: MOCAP marker trajectory during a straight-line running trial (A) and a zig-zag running trial (B).

The inertial measurement unit (IMU) selected for this study is a YEI 3-space sensor (Yost Engineering, Portsmouth, Ohio), shown in Fig. 4.2A, that provides three-axis sensing of angular velocity and linear acceleration. The device measures angular rates up to 2000 deg/s, with 16-bit resolution, and a 0.03 deg/sec/√Hz noise floor and accelerations up to 12 g, with 14-bit resolution, and a 650 μg/√Hz noise floor. Data is written to flash memory on the device and subsequently downloaded to a computer via USB upon completion of all 40 trials. The accelerometer and rate gyro data are sampled at approximately 700 Hz. This IMU provides highly accurate orientation data and, as a requirement, employs well-calibrated scale factors for each axis of the rate gyro. The dc offset values for each rate gyro axis are identified at the start of each trial when the IMU is at rest. Doing so reduces the adverse effects of temperature changes on gyro output. The accelerometer is calibrated following the procedure detailed in [98] which provides both scale factor and offset values for each of the three sense axes. This combination of calibration techniques ensures that the IMU provides accurate measurements of acceleration and angular velocity resolved along the three sense axes designated by the orthonormal triad ($\hat{e}_1$, $\hat{e}_2$, $\hat{e}_3$) shown in Fig. 4.2A. In keeping with [45,47], the sampled IMU data is low-pass filtered with a cut-off frequency of 15 Hz prior to use. The filtered

components of (calibrated) acceleration for an example “Run” trial are shown in Fig. 4.2B.

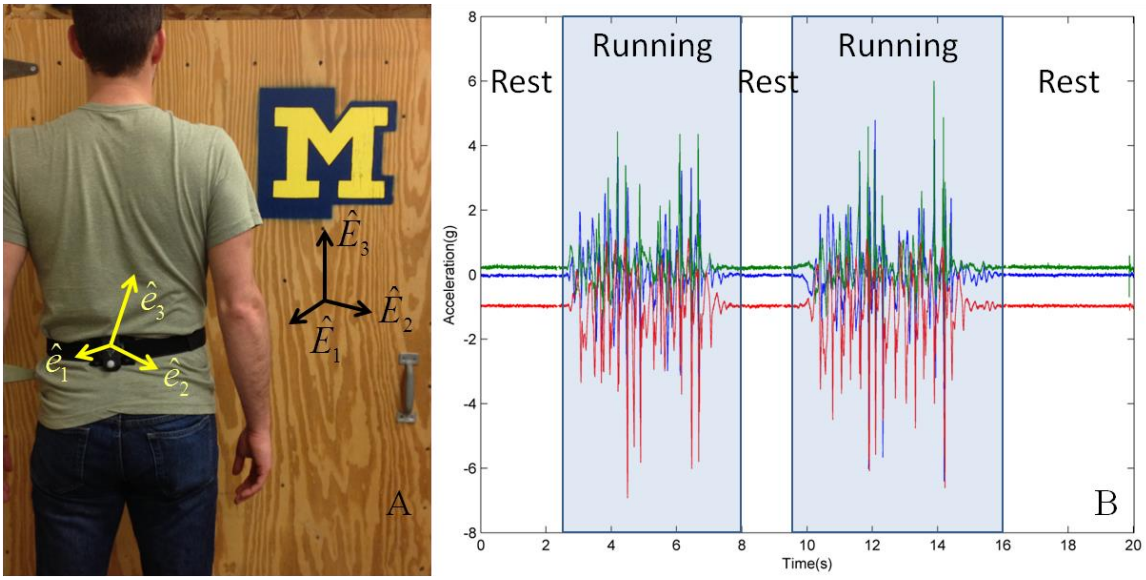

Figure 4.2: (A) The IMU (YEI 3-space) is held against the lumbar portion of the subject’s spine by a tension strap. A maker mounted to the IMU casing is simultaneously employed for MOCAP measurements. (B) The filtered components of acceleration measured by the IMU over two periods of motion during an example “Run” trial. Components: $\hat{e}_1$=blue, $\hat{e}_2$=green, and $\hat{e}_3$=red.

As illustrated in Fig. 4.2A, the IMU is held in place using an elastic strap which wraps around the lower abdomen of the athlete, indexing the device against the lumbar portion of the spine. The acceleration components, shown in Fig. 4.2B, illustrate two sequential motion periods (highlighted in blue) during each of which the athlete ran from the first cone to the second cone and back. The short resting time intervals before, between and after the two motion periods are readily observable. The resting time intervals are defined by any time when the vector magnitude of the IMU measured acceleration and angular velocity depart from their values when the IMU is stationary by more than prescribed thresholds. The thresholds are further defined by the noise magnitude in the magnitude of the acceleration and angular velocity while the subject remains at rest at the start of the trial (e.g. 3.4 deg/s, 0.08 g for the example trial of Fig. 4.2B).

Note that the IMU acceleration output, $\vec{a}_m$, includes both the physical acceleration at the center of the accelerometer, $\vec{a}$, plus the acceleration due to gravity, $\vec{g}$ (i.e. 9.81 m/s^2). Thus, $\vec{a}$ is recovered from

$$\vec{a} = \vec{a}_m - \vec{g} \tag{4.1}$$

which further requires the orientation of the IMU-fixed frame ($\hat{e}_1, \hat{e}_2, \hat{e}_3$) relative to an inertial frame defined by the orthonormal triad ($\hat{E}_1, \hat{E}_2, \hat{E}_3$, Fig. 4.2A), where $\hat{E}_1$ and $\hat{E}_2$ define the horizontal plane, and $\hat{E}_3$ is aligned with gravity.

The orientation of ($\hat{e}_1, \hat{e}_2, \hat{e}_3$) relative to ($\hat{E}_1, \hat{E}_2, \hat{E}_3$) is determined in two steps. The first step establishes the initial orientation of ($\hat{e}_1, \hat{e}_2, \hat{e}_3$) relative to ($\hat{E}_1, \hat{E}_2, \hat{E}_3$) while the athlete is at rest prior to a motion period. During this (albeit short) rest interval, the accelerometer measures solely the acceleration due to gravity thus establishing the initial direction of $\hat{E}_3$ in the IMU-fixed frame. Next, one unit vector in the horizontal plane $\hat{E}_2$, follows from $\hat{E}_2 = \hat{E}_3 \times \hat{e}_1 \big/ \left\| \hat{E}_3 \times \hat{e}_1 \right\|$. Finally, $\hat{E}_1 = \hat{E}_2 \times \hat{E}_3$ yields a second unit vector in the horizontal plane. These three computations establish the initial direction cosine matrix that defines the orientation of the IMU-fixed frame ($\hat{e}_1, \hat{e}_2, \hat{e}_3$) relative to an inertial frame ($\hat{E}_1, \hat{E}_2, \hat{E}_3$) which remains fixed during the subsequent motion period. The components of the direction cosine matrix R also establish the initial values of the Euler parameters ($\varepsilon_1, \varepsilon_2, \varepsilon_3, \varepsilon_4$) per

$$R(t) = \begin{bmatrix} \varepsilon_1^2 - \varepsilon_2^2 - \varepsilon_3^2 + \varepsilon_4^2 & 2(\varepsilon_1\varepsilon_2 - e_3 e_4) & 2(\varepsilon_1\varepsilon_3 + \varepsilon_2\varepsilon_4) \\ 2(\varepsilon_1\varepsilon_2 + e_3 e_4) & \varepsilon_2^2 - \varepsilon_1^2 - \varepsilon_3^2 + \varepsilon_4^2 & 2(\varepsilon_2\varepsilon_3 - \varepsilon_1\varepsilon_4) \\ 2(\varepsilon_1\varepsilon_3 - \varepsilon_2\varepsilon_4) & 2(\varepsilon_2\varepsilon_3 + \varepsilon_1\varepsilon_4) & \varepsilon_3^2 - \varepsilon_1^2 - \varepsilon_2^2 + \varepsilon_4^2 \end{bmatrix} \tag{4.2}$$

for subsequent use in the second step [93].

The evolution of the Euler parameters are determined in the second step by employing the initial condition above and then integrating the Euler parameter state equations

$$\begin{bmatrix} \dot{\varepsilon}_1 \\ \dot{\varepsilon}_2 \\ \dot{\varepsilon}_3 \\ \dot{\varepsilon}_4 \end{bmatrix} = \frac{1}{2} \begin{bmatrix} 0 & \omega_3(t) & -\omega_2(t) & \omega_1(t) \\ -\omega_3(t) & 0 & \omega_1(t) & \omega_2(t) \\ \omega_2(t) & -\omega_1(t) & 0 & \omega_3(t) \\ -\omega_1(t) & -\omega_2(t) & -\omega_3(t) & 0 \end{bmatrix} \begin{bmatrix} \varepsilon_1 \\ \varepsilon_2 \\ \varepsilon_3 \\ \varepsilon_4 \end{bmatrix} \tag{4.3}$$

forward in time. Here, $\omega_1(t)$, $\omega_2(t)$, and $\omega_3(t)$ are the three components of the measured angular velocity in the IMU frame. This ordinary differential equation is integrated forward in time using standard numerical integration techniques subject to the Euler parameter normalization constraint $\varepsilon_1^2 + \varepsilon_2^2 + \varepsilon_3^2 + \varepsilon_4^2 = 1$ at each time step. Doing so provides the Euler parameters at any time, hence the direction cosine matrix $R(t)$ at any time via Eq. (4.2).

Returning to Eq. (4.1), one can now deduce the desired acceleration of the torso mounted accelerometer $\vec{a}$ with respect to the inertial frame ($\hat{E}_1$, $\hat{E}_2$, $\hat{E}_3$) per

$$\vec{a} = R(t)\vec{a}_m - g\hat{E}_3 \tag{4.4}$$

Subsequent integration of $\vec{a}$ (e.g., via trapezoidal rule) during each of the motion periods yields the velocity of the torso-mounted IMU subject to the initial condition that the athlete is at rest at the beginning of the motion period.

It is well established that integration of IMU-measured acceleration introduces error in the resulting velocity due to sensor drift [61,75]. This drift error is approximately identified and removed per

$$\vec{v}_c = \vec{v} - \vec{f}(t) \tag{4.5}$$

where $\vec{v}$ is the uncorrected athlete velocity as determined by direct integration of (4.4), $\vec{v}_c$ is the drift-corrected velocity of the athlete, and $\vec{f}(t)$ is a vector-valued function of time approximating the drift error. We identify this function by considering times when the motion of the athlete is known. For example, the athlete is stationary at the starting time (t_s) and ending time (t_e) of any motion period yielding

$$\vec{f}(t_s) = \vec{v}(t_s) \tag{4.6a}$$

$$\vec{f}(t_e) = \vec{v}(t_e) \tag{4.6b}$$

In addition, there may be instants during the motion period ($t_s < t < t_e$) when the measured acceleration and angular velocity return to their stationary values (or within prescribed thresholds of those values), suggesting the athlete's velocity returns to zero (or approximately zero). These zero velocity states are expected during the "burst" walking and running tasks considered herein since the torso velocity returns to zero (or approximately zero) sometime during the short time interval when the athlete reaches a cone, changes direction, and proceeds to the next cone. Let the index q denote the number of such "zero velocity updates" within a motion period. Thus,

$$\vec{f}\left(t_j\right) = \vec{v}\left(t_j\right) \text{ for } j = 1,\ldots,q \tag{4.7}$$

holds approximately where $t_j \in (t_s, t_e)$ denotes the time of the j^{th} zero velocity update. Moreover, the athlete remains at rest for finite (though potentially short) time intervals prior to and following the motion period. The acceleration of the torso must therefore vanish during these finite time intervals. The acceleration, which must remain continuous, further requires that

$$\dot{\vec{f}}\left(t_s\right) = \dot{\vec{v}}\left(t_s\right) \tag{4.8a}$$

$$\dot{\vec{f}}\left(t_e\right) = \dot{\vec{v}}\left(t_e\right) \tag{4.8b}$$

where $\dot{\vec{f}}\left(t\right)$ is the derivative of the drift-error function, and $\dot{\vec{v}}\left(t\right)$ is the uncorrected acceleration.

Case 1: $0 \le q \le 1$

For cases when there is at most one velocity update identified within a motion period, we approximate the drift error by the quadratic function

$$\vec{f}\left(t\right) = \vec{c}_0 + \vec{c}_1 t + \vec{c}_2 t^2 \tag{4.9}$$

which introduces three unknown (vector-valued) coefficients ($\vec{c}_0, \vec{c}_1, \vec{c}_2$). The three unknowns are found by solving Eq. (4.6) and then by minimizing the sum of the squared error in Eqs. (4.7) and (4.8) recognizing that these two latter conditions may only hold approximately. Herein, minimization is accomplished using the method of Lagrange

multipliers (the Lagrangian is detailed in the Appendix, Section 4.5), but any constrained optimization method can also be used.

Case 2: $q > 1$

For cases where there are two or more zero velocity updates identified within a motion period, exactly satisfying the zero velocity conditions would require approximating the drift error as a higher order polynomial. This approach could potentially suffer from oscillations at the boundaries of the motion period known as Runge's phenomenon. To avoid this issue, we minimize the velocity at the zero velocity updates by considering a piecewise-linear approximation to the drift error

$$\vec{f}(t) = \begin{cases} \vec{c}_{1,0} + \vec{c}_{1,1} t & t_s \geq t \geq t_1 \\ \vec{c}_{j,0} + \vec{c}_{j,1} t & t_{j-1} > t \geq t_j \text{ for } j = 2, \ldots, q \\ \vec{c}_{q+1,0} + \vec{c}_{q+1,1} t & t_q > t \geq t_e \end{cases} \tag{4.10}$$

where the $q+1$ linear functions introduce $2(q+1)$ unknown coefficients. The drift-error function is continuous in time (enforcing continuity in velocity) which yields *q* equations, one for each zero velocity update per

$$\vec{c}_{j,0} + \vec{c}_{j,1} t_j = \vec{c}_{j+1,0} + \vec{c}_{j+1,1} t_j \text{ for } j = 1, \ldots, q \tag{4.11}$$

Finally, we require that

$$\vec{c}_{j,1} = \vec{c}_{j+1,1} \text{ for } j = 1, \ldots, q \tag{4.12}$$

be satisfied at least approximately to minimize jerk. The minimization of jerk is a recognized feature of smooth human motion [99]. The $2(q+1)$ unknown coefficients appearing in (4.10) are determined by satisfying Eqs. (4.6) and (4.11) and minimizing the sum of the squared error in Eqs. (4.7), (4.8), and (4.12). The minimization is again achieved using the method of Lagrange multipliers as detailed in the Appendix (Section 4.5).

Following identification of the drift error function $\vec{f}(t)$ (for either Case 1 or Case 2), the corrected estimate of the athlete velocity $\vec{v}_c(t)$ follows from (4.5). The horizontal speed of the athlete follows immediately from the vector sum of the two

horizontal velocity components. This horizontal speed is ultimately compared with independent measurements from MOCAP.

MOCAP data is collected simultaneously with the IMU data. A 16-camera Vicon^{TM} MOCAP system is used to record the three-dimensional position of the reflective marker attached to the IMU shown in Fig. 4.2A. This position data is sampled at 240 Hz and low-pass filtered at 15 Hz prior to numerical differentiation to obtain the velocity of the marker. The marker velocity vector is further decomposed into a component in the vertical ($\hat{E}_3$) direction and the residual that lies in the horizontal ($\hat{E}_1, \hat{E}_2$) plane. This decomposition follows from careful *a priori* calibration of the camera system including calibration of the vertical ($\hat{E}_3$) direction. The magnitude of the horizontal residual yields the MOCAP-measured horizontal speed of the torso for direct comparison with the IMU-estimated horizontal speed above.

4.3. Results and Discussion

The computational algorithm above estimates the speed of an athlete using a single torso-mounted IMU. Doing so provides a non-invasive means to assess athlete performance right on the field of play and without requiring GPS data or *a priori* subject-specific calibration. In this section we present results from this algorithm, critically compare them to results obtained by MOCAP, discuss potential limitations of the algorithm, and further compare and contrast results from alternative algorithms [44,45,47]. We open with an example that highlights the performance of the drift estimation algorithm.

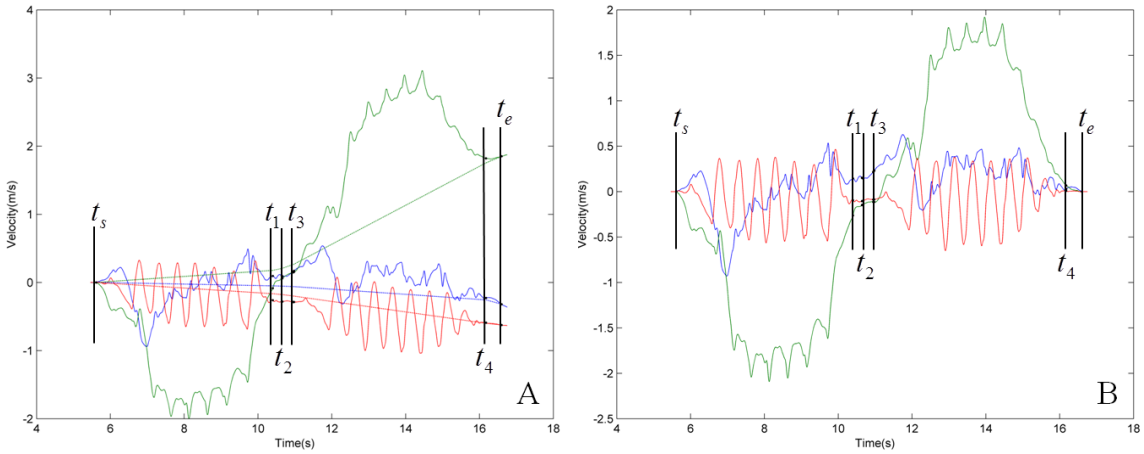

Figure 4.3: (A) Uncorrected velocity components ($\hat{E}_1$=blue, $\hat{E}_2$=green, $\hat{E}_3$=red) determined from IMU data (solid curves) and their respective drift error correction functions (dotted curves) for an example "Walk" trial with four identified velocity updates ($q=4$). (B) Corrected velocity components ($\hat{E}_1$=blue, $\hat{E}_2$=green, $\hat{E}_3$=red) determined from IMU data. The start and end times of the motion period are labeled t_s and t_e, respectively. The four intervening times when the torso velocity is close to zero ($q=4$) are labeled t_1, t_2, t_3 and t_4.

Figure 4.3A illustrates three components of the uncorrected athlete velocity $\vec{v}$ (solid curves: $\hat{E}_1$=blue, $\hat{E}_2$=green, $\hat{E}_3$=red) plotted against time for one motion period during an example "Walk" trial. Also shown are the piecewise-linear drift corrections for each component (dashed curves: $\hat{E}_1$=blue, $\hat{E}_2$=green, $\hat{E}_3$=red) using the drift error estimation algorithm above. Inspection of the uncorrected velocity components reveals appreciable one-sided (drift) errors that increase with time despite the fact that the velocity must return to zero at the end of the motion period (t_e). The drift error estimates drive all velocity components to zero at t_e while minimizing the velocity and jerk at each of four ($q=4$) identified zero velocity update times (see times t_1, t_2, t_3 and t_4). The corrected velocity components are illustrated in Fig. 4.3B. The instantaneous horizontal speed of the athlete is constructed from the corrected horizontal velocity and this is further compared to the horizontal speed measured from MOCAP in Figure 4.4.

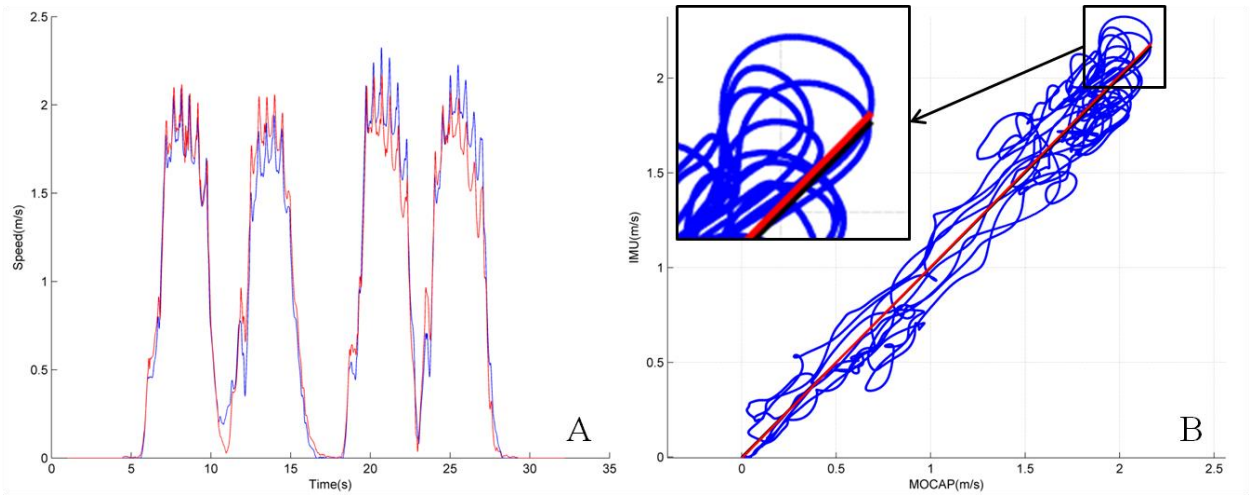

Figure 4.4: (A) IMU (blue) and MOCAP (red) horizontal speed as functions of time during the example walking trial over two motion periods. The correlation plot (B) also includes a best fit line to the data (red) and a line with unit slope (black).

The IMU (blue) and MOCAP (red) speed estimates are plotted against time for the same example "Walk" trial in Fig. 4.4A which includes two motion periods. The qualitative and quantitative agreement between the two estimates remains excellent throughout the trial. Specifically, the root mean square error (RMSE) in the IMU-predicted speed compared to MOCAP is 0.15 m/s. For reference, this RMSE represents a mere 7.1% of the peak walking speed estimated by MOCAP during this trial. The agreement between the two estimates is further revealed in Fig. 4.4b which plots the IMU-predicted speed versus MOCAP-predicted speed for the entire duration of the example "Walk" trial; refer to blue curve. If the agreement were perfect, this data would collapse to the unit line; that is the line having unit slope and zero intercept (black line). The computed best fit line to the data (red line) lies nearly on top of the unit line. As illustrated in Fig. 4.4B, the IMU and MOCAP estimated speeds remain highly correlated ($r = 0.98$) with the best fit line having near unit slope (Slope = 1.01).

Motion Type	RMSE m/s	% RMSE	r	Slope
Walk	0.35 (0.22)	16.7 (10.8)	0.89 (0.11)	0.98 (0.07)
Jog	0.35 (0.16)	10.0 (4.4)	0.96 (0.05)	1.01 (0.06)
Run	0.38 (0.16)	7.6 (3.0)	0.97 (0.02)	0.99 (0.04)
Zig-zag	0.79 (0.44)	17.3 (9.8)	0.85 (0.13)	0.90 (0.09)

Table 4.1: Mean (and standard deviation) of RMS error (RMSE), RMSE relative to peak speed estimated by MOCAP (% RMSE), correlation coefficient (r), and slope of IMU-predicted speed compared to MOCAP for 10 trials of each of the four motion types.

The analysis above illustrated for one "Walk" trial was repeated for 10 trials of each of the four motion types (total of 40 trials). The results are summarized in Table 4.1 which reports for each motion type the mean (and standard deviation) of the RMS error (RMSE), the RMSE as a percentage of peak speed, the correlation (r), and the slope of IMU-predicted speed compared to the MOCAP predicted speed. The results presented in Table 4.1 confirm the overall strong agreement between IMU versus MOCAP estimated speeds. Among the motion types, this agreement is highest for the "Run" and "Jog" trials which have mean (SD) RMSE of 0.38 (0.16) and 0.35 (0.16) m/s, correlation coefficients of 0.97 (0.02) and 0.96 (0.05), and slopes of 0.99 (0.04) and 1.01 (0.06), respectively. The agreement lessens somewhat for the "Walk" trials as evidenced by the slightly lower mean correlation coefficient (0.89), and more so for the "Zig-zag" trials which exhibit the largest RMSE (0.79 m/s), the lowest correlation coefficient (0.85), and slope (0.90) furthest from one.

The level of agreement between IMU and MOCAP estimated speeds reported in Table 4.1 however has little to do with the motion type. Instead, it depends on the integration time ($t_e - t_s$) and it improves as this time decreases. Note that the Run, Jog, Walk, and Zig-zag motions required increasingly larger integration time as revealed by the mean (SD) integration times of 5.8 (0.4), 7.3 (1.0), 10.3 (0.5), and 12.8 (0.8) seconds, respectively.

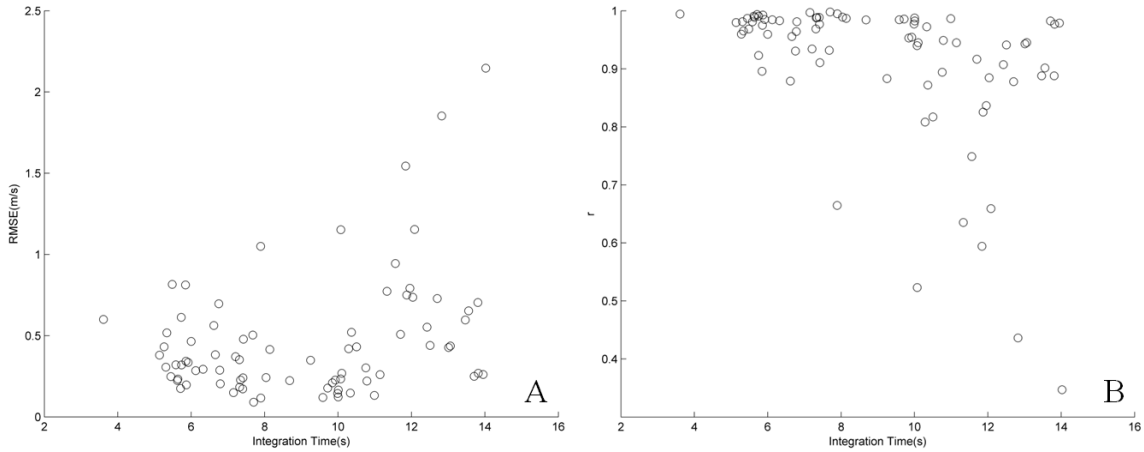

Figure 4.5: (A) RMSE and (B) correlation coefficient (r) between IMU and MOCAP estimated speed versus integration time. RMSE increases and r decreases with integration time.

The results of Fig. 4.5 convincingly demonstrate the degradation in accuracy of the IMU-derived speed estimates with integration time. Specifically, as integration time increases, the RMSE relative to MOCAP increases (Fig. 4.5A), the correlation coefficient decreases (Fig. 4.5B), and the variability in each increases (Fig. 4.5A and B). Fortunately, athlete motion in many sports, especially explosive sports like basketball, is often limited to very short periods of running or sprinting (less than 10s) separated by (often very short) periods of rest [42,100]. Motivated by this fact, we report in Table 4.2 the mean (standard deviation) of the above error metrics for all motion periods with integration times less than 10 s versus motion periods with integration times exceeding 10 s. The mean (SD) RMSE in the estimated speed is 0.35 (0.20) m/s for all motion periods less than 10 s. Likewise, the IMU-derived speeds are well correlated with MOCAP-derived speeds as evidenced by the mean (SD) correlation coefficient of 0.96 (0.05) and slope of 0.99 (0.07). This level of accuracy is quite promising for highly dynamic sports, like basketball, where athletes are quickly alternating between standing and sprinting.

Error Metric	$t_e - t_s \leq 10s$	$t_e - t_s > 10s$
RMSE (m/s)	0.35 (0.20)	0.62 (0.48)
r	0.96 (0.05)	0.85 (0.16)
Slope	0.99 (0.07)	0.89 (0.14)
n	46	34

Table 4.2: Mean (standard deviation) of RMSE correlation coefficient (r), and slope of IMU-estimated speed compared to MOCAP-estimated speed for all 40 trials (80 motion periods total, where n is the number included in each group). Separately considered are motion periods with integration times less than versus greater than 10 seconds.

Finally, we compare the above findings to those of existing algorithms that also estimate athlete speed using shank-, foot-, or torso-mounted IMUs [44,45,47]. These studies report average speed and so we follow suit by comparing the average speeds for each of the motion periods. For all motion periods less than 10s, the mean (SD) error in estimated average speed is 0.03 (0.18) m/s, and the RMSE is 0.18 m/s, or 4.3% relative to average speed reported by MOCAP. These results compare favorably to those presented in [47], where a shank mounted IMU estimates average running speed with mean (SD) error of 0.11 (0.03) m/s and RMSE of 5.9% relative to treadmill speeds similar to those considered herein. They also compare favorably to the results presented in [44,45] where neural-network techniques estimate average speed to within 0.12 m/s RMSE compared to that determined via stop-watch defined time over a known course [45] or to within 0.15 m/s RMSE as compared to treadmill speed [44]. Recall, however that two of these alternative methods [44,45] require *a priori* training of a neural network. Additionally, one of these studies [44] requires subject height and weight as input to the trained neural network, while the other [45] requires a heel mounted accelerometer. Similarly, the method presented in [47] requires both subject specific calibration and a shank-mounted IMU (which remains vulnerable to damage and may also promote athlete injury).

4.4. Conclusions

This work presents a new algorithm for estimating athlete speed using data from a single torso-mounted inertial measurement unit that includes a three-axis accelerometer and a three-axis angular rate gyro. Experiments are conducted for 40 trials and for four

types of motion including straight-line walking, jogging and running and zig-zag running. The accuracy of the speed estimates are benchmarked to those estimated by video based motion capture (MOCAP). The algorithm predicts instantaneous athlete speed that correlates well with MOCAP (mean RMSE = 0.35 m/s, r = 0.96, slope = 0.99) for short duration (less than 10 s) "burst" motions characteristic of explosive sports such as basketball. The method predicts average speed to within an absolute mean error of 0.03 m/s, and a RMSE of 0.18 m/s, or 4.3% relative to average MOCAP speed. These results compare favorably to existing methods which, by contrast, require shank- or foot-mounted IMUs and further require *a priori* subject-specific calibration.

4.5. Appendix

As discussed in the body of this manuscript, the drift-error in velocity is approximated as a vector function $\vec{f}(t)$ which is defined as a quadratic in time [Eq. (4.9)] for cases where $0 \le q \le 1$, and as a piecewise-linear function in time [Eq. (4.10)] for cases where $q > 1$. The unknown, constant coefficients of these functions are defined according to the method of Lagrange multipliers where the Lagrangian for each case is defined as follows.

Case 1: $0 \le q \le 1$

$$L(c,\lambda) = \sum_{j=1}^{q}\left\{\left(\frac{v(t_j)-c_0-c_1t_j-c_2t_j^2}{dv}\right)^2\right\} + \left(\frac{\dot{v}(t_s)-c_1-2c_2t_s}{d\dot{v}}\right)^2 + \left(\frac{\dot{v}(t_e)-c_1-2c_2t_e}{d\dot{v}}\right)^2 + \lambda_0\left(\frac{v(t_s)-c_0-c_1t_s-c_2t_s^2}{dv}\right) + \lambda_1\left(\frac{v(t_e)-c_0-c_1t_e-c_2t_e^2}{dv}\right) \tag{4.13}$$

Case 2: $q>1$

$$L(c,\lambda) = \sum_{j=1}^{q}\left\{\left(\frac{v(t_j)-c_{j,0}-c_{j,1}t_j}{dv}\right)^2 + \left(\frac{c_{j,1}-c_{j+1,1}}{d\dot{v}}\right)^2 + \lambda_j\left(\frac{c_{j,0}+c_{j,1}t_j-c_{j+1,0}-c_{j+1,1}t_j}{dv}\right)\right\} + \left(\frac{\dot{v}(t_s)-c_{1,1}}{d\dot{v}}\right)^2 + \left(\frac{\dot{v}(t_e)-c_{q+1,1}}{d\dot{v}}\right)^2 + \lambda_0\left(\frac{v(t_s)-c_{1,0}-c_{1,1}t_s}{dv}\right) + \lambda_{q+1}\left(\frac{v(t_e)-c_{q+1,0}-c_{q+1,1}t_e}{dv}\right) \tag{4.14}$$

where dv is a normalizing factor for the speed terms of the Lagrangian, defined as the absolute velocity error due to drift over the whole motion period, or more explicitly,

$$dv = \left\| v(t_e) - v(t_s) \right\| \tag{4.15}$$

The normalizing factor for the acceleration terms of the Lagrangian, $d\dot{v}$, is defined as the absolute mean acceleration of the velocity drift error during the motion period, or

$$d\dot{v} = \left\| \frac{v(t_e) - v(t_s)}{t_e - t_s} \right\| \tag{4.16}$$

These non-dimensional Lagrangian functions (4.13-4.14) are written in scalar form here, and can be applied equally for each of the three components of uncorrected athlete velocity. In this case, the method of Lagrange multipliers provides a determined set of linear equations in terms of the unknown coefficients (c) and Lagrange multipliers (λ) by setting the partial derivative of the Lagrangian with respect to each unknown equal to zero.

Chapter 5: Joint Reactions Deduced from IMU Data

5.1. Introduction

The studies presented in Chapters 2-4 detail novel IMU-based techniques to support applications in sports training. In this Chapter we depart from this theme and instead advance the use of IMU arrays to estimate joint reactions in multibody systems. This application is motivated by the fact that the annual number of total hip and knee replacement surgeries are predicted to increase by over 170% (to 572,000) and 670% (to 3.48 million) respectively by the year 2030 [49]. This alarming increase in joint replacements requires the development of non-invasive, clinically viable methods to identify pathological lower extremity motion before joint injuries occur. One of these potential methods, inverse dynamic modeling, begins by approximating the human body as a multibody system of rigid segments connected by joints. Knowledge of the segmental kinematics, namely the angular velocity and angular acceleration of each segment and the linear acceleration of the segment's mass center, enables a solution for the reaction kinetics (i.e. forces and moments) acting at the joints provided segmental inertial properties (e.g. mass center location, mass, inertia tensor) are known [13].

The current standard for quantifying segmental kinematics is video-based motion capture (MOCAP). MOCAP is an expensive technology that employs an array of high-speed cameras calibrated to provide three-dimensional positions of a set of reflective markers attached to a subject. Markers are typically attached to a subject's skin via adhesive tape in specific locations to define bony anatomical landmarks [11]. This method is often constrained to a dedicated motion-capture laboratory and requires an operator skilled in the placement of the reflective markers as well as the collection and analysis of the resulting marker position data.

As mentioned previously, inverse dynamic modeling requires knowledge of the angular velocity and angular acceleration of each body segment in addition to the segment's mass center acceleration. Computation of these quantities from marker position data requires a differencing operation to compute segment angles and then successive numerical differentiations to compute angular velocity and angular acceleration. Two successive differentiations are also required to compute segmental mass center acceleration. It is well established that these numerical differentiations significantly amplify small errors in the initial position data (due to measurement error, marker occlusion, skin motion, etc.), resulting in potentially large errors in the very kinematic quantities required for inverse dynamics [3,14].

The above limitations (accuracy, cost, and laboratory infrastructure) prevent widespread adoption of MOCAP as a clinically viable tool for estimating joint reactions. However, these shortcomings may be addressed by advancing an alternative technology, namely miniaturized inertial measurement units (IMUs). Miniature IMUs, which incorporate MEMS accelerometers and angular rate gyros, measure the angular velocity and linear acceleration of any rigid body to which they are attached. When deployed as a body worn sensor array, miniature IMUs directly provide the angular velocity and linear acceleration of body segments needed for inverse dynamics and require just a single derivative operation to yield the requisite angular acceleration. Thus, miniature IMU arrays have the potential to yield far more accurate kinematic data for the inverse dynamic estimates of joint reactions than (position-based) MOCAP. In addition, miniature IMU arrays are a highly portable technology that can be deployed in the clinic, workplace, or field of play and for a very small fraction of the cost of MOCAP.

Several recent studies explore the use of IMUs for inverse dynamic modeling and in (non-laboratory) environments previously inaccessible using MOCAP [101–104]. One study employs IMUs as part of the inverse dynamic analysis of the human knee joint for patients with knee osteoarthritis [101]. Estimates of the knee adduction moment during ambulatory gait are obtained using kinematic data from a shank-mounted IMU with ground reactions measured from a wearable, instrumented shoe. Moreover, this study benchmarks the adduction moment estimated using the portable technology (IMU plus instrumented shoe) with that estimated using a laboratory-based optoelectronic marker

system and a floor-mounted force plate. While it is important to benchmark the accuracy of the joint reactions estimated using data from inertial sensors, the study [101] employs a gold standard (optoelectronic cameras) which inherits the inaccuracies of MOCAP in measuring the requisite segmental kinematics.

The objective of this paper is to use a precise gold standard to explore the accuracy of joint reactions estimated using miniature IMU arrays. To this end, we conduct a careful benchmarking study where the reaction forces and moments acting at the joints of a well characterized mechanical system are directly measured from embedded six degree-of-freedom force and torque sensors. The mechanical system, an instrumented double-pendulum introduced in the companion paper [105], incorporates a two-node array of miniature wireless IMU's that provide the kinematic data for inverse dynamic estimates of the joint reactions. We open with a brief description of the double pendulum from [105] and the additional instrumentation needed for this study.

5.2. Methods

We return to the instrumented double pendulum introduced in the companion paper [105] that provides benchmark measurements of both kinematic and kinetic data. Recall that the benchmark kinematic data is provided by two high resolution (0.07 deg.) rotary optical encoders that measure the rotations across both joints. The benchmark kinetic data is provided by two high resolution load cells embedded in the two links immediately adjacent to each joint (red cylinders, Fig. 5.1A). In addition, the double pendulum is instrumented with two (6 dof) IMUs, one per link (blue rectangles, Fig. 5.1A). The instrumentation is illustrated in the schematic of Fig. 5.1 and also visible in the photograph of Fig. 1 of [105]. A description of the load cells is provided below and descriptions of the IMUs and encoders are provided in the companion paper [105]. Analysis of the data from these instruments requires definition of the frames of reference illustrated in Fig. 5.1 B-D.

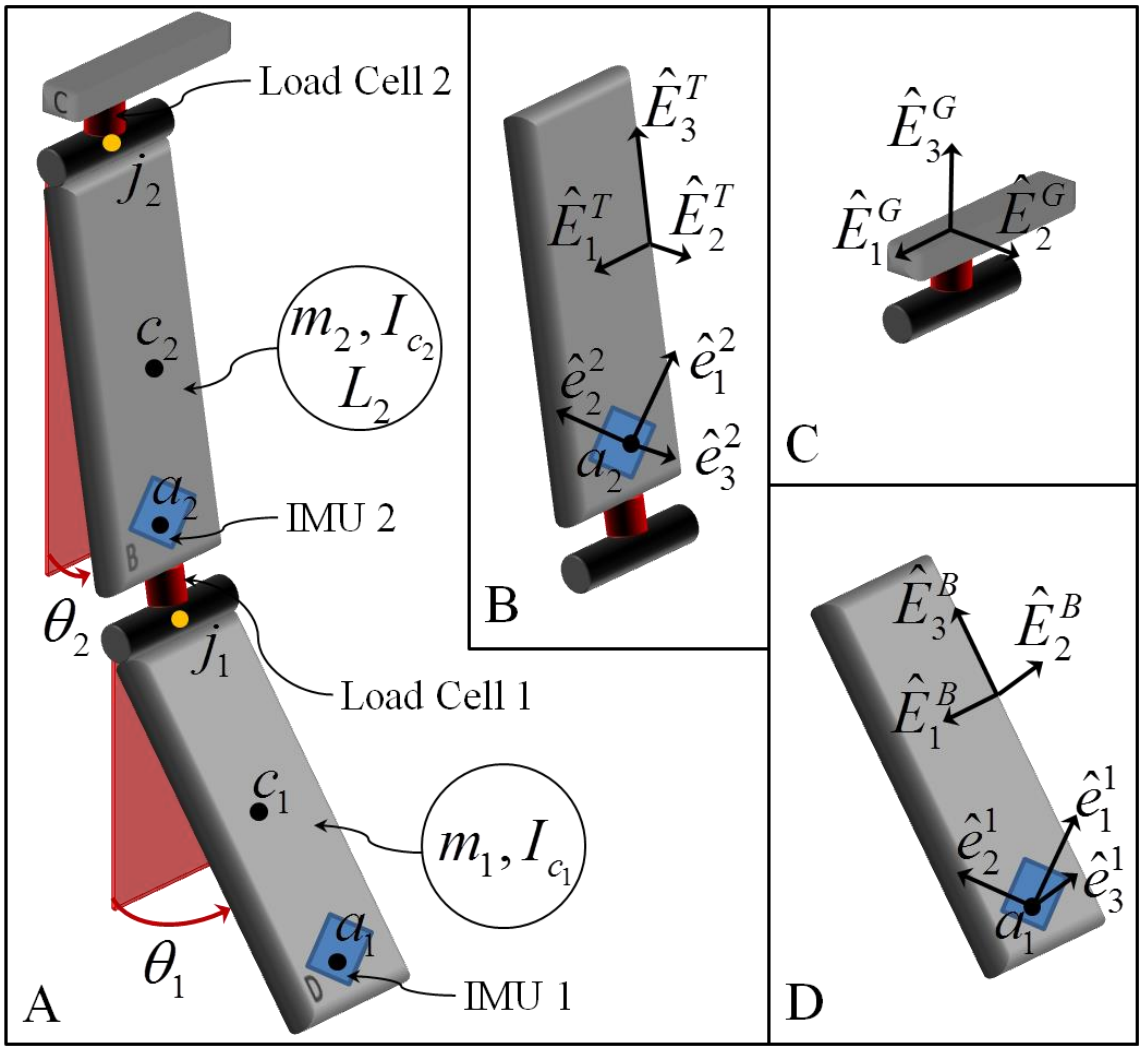

Figure 5.1: Schematic of the instrumented double pendulum with definitions of reference frames defined. Refer also to photograph shown in Fig. 1 of [105].

We define three reference frames to describe the dynamics of the double pendulum: frame B is fixed to the bottom link and is composed of the orthogonal unit vectors ($\hat{E}_1^B$, $\hat{E}_2^B$, $\hat{E}_3^B$, Fig. 5.1D); frame T is fixed to the top link and is composed of the orthogonal unit vectors ($\hat{E}_1^T$, $\hat{E}_2^T$, $\hat{E}_3^T$, Fig. 5.1B); and frame G is an inertial frame composed of the unit vectors ($\hat{E}_1^G$, $\hat{E}_2^G$, $\hat{E}_3^G$, Fig. 5.1C). The reference frames are defined such that $\hat{E}_1^T$, $\hat{E}_1^B$, and $\hat{E}_1^G$ are parallel to the rotation axes of the links, $\hat{E}_3^B$ and $\hat{E}_3^T$ are aligned with the long axis of their respective links, and $\hat{E}_3^G$ is aligned with gravity. The link-fixed reference frames (B and T), are assumed to be aligned with the principal axes

of the links. We must also consider two additional reference frames defined by the sense axes of the two attached IMUs. The bottom link IMU reports measurements along ($\hat{e}_1^1,\ \hat{e}_2^1,\ \hat{e}_3^1$, Fig. 1D), while the top link IMU reports measurements along ($\hat{e}_1^2,\ \hat{e}_2^2,\ \hat{e}_3^2$, Fig. 5.1B).

The two load cells noted in Fig. 5.1A are Nano17^{TM} force/torque sensors which provide three-axis measurement of both force and moment. They resolve forces up to 70 N along the length of the pendulum links and 50 N in the two transverse directions, and all with a resolution of 0.0125 N. They resolve moments up to 500 N-mm about all three axes with a resolution of 0.0625 N-mm. The load cell mounted to the top link at j_1 measures reactions at this joint and with components resolved in frame T. The load cell mounted to the support at j_2 measures reactions at this joint and with components resolved in frame G. The reaction forces ($\vec{F}_1,\ \vec{F}_2$) and moments ($\vec{M}_1,\ \vec{M}_2$) measured by each load cell are shown in the free body diagrams of the bottom and top links in Fig. 5.2A and B, respectively.

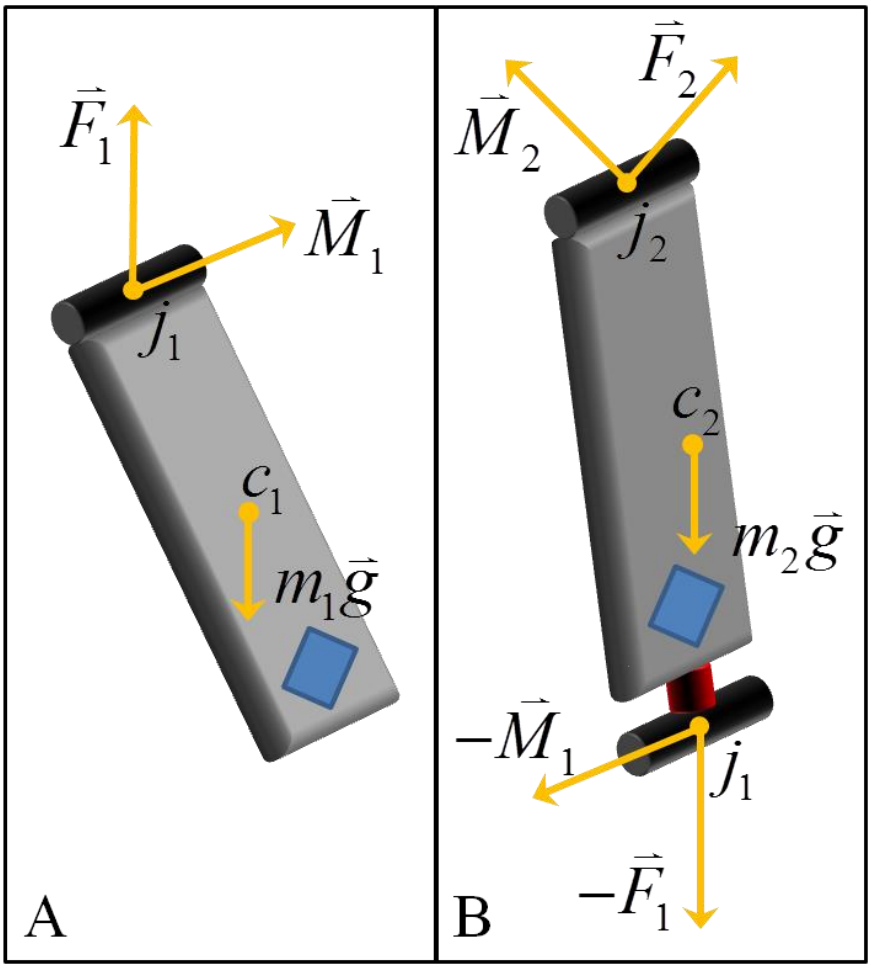

Figure 5.2: Free body diagrams for the bottom (A) and top (B) link of the double pendulum.

Starting from the free body diagrams in Fig. 5.2, systematic use of the Newton-Euler equations for each body yields expressions for the reactions. Specifically, Newton's second law for both links yields the reaction forces

$$\vec{F}_1 = m_1\left(\vec{a}_{c1} - \vec{g}\right) \tag{5.1}$$

$$\vec{F}_2 = \vec{F}_1 + m_2\left(\vec{a}_{c2} - \vec{g}\right) \tag{5.2}$$

where m_1 and m_2 is the mass of the bottom and top link, respectively, $\vec{a}_{c1}$ and $\vec{a}_{c2}$ is the acceleration of the mass center of the bottom and top link, respectively, and $\vec{g}$ denotes gravity. Similarly, Euler's second law for both links yields the reaction moments

$$\vec{M}_1 = I_{c1}\dot{\vec{\omega}}_1 + \vec{\omega}_1 \times I_{c1}\vec{\omega}_1 - \left(\vec{r}_{c1/j1} \times \vec{F}_1\right) \tag{5.3}$$

$$\vec{M}_2 = I_{c2}\dot{\vec{\omega}}_2 + \vec{\omega}_2 \times I_{c2}\vec{\omega}_2 - \left(\vec{r}_{c2/j2} \times \vec{F}_2\right) + \vec{M}_1 + \left(\vec{r}_{c2/j1} \times \vec{F}_1\right) \tag{5.4}$$

where I_{c1} and I_{c2} is the inertia tensor (principal axes through centroid) for the bottom and top links, respectively, $\vec{r}_{c1/j1}$ is a position vector locating the (bottom link) mass center c_1 relative to j_1, $\vec{r}_{c2/j1}$ and $\vec{r}_{c2/j2}$ are position vectors locating the (top link) mass center c_2 relative to j_1 and j_2, respectively, and $\vec{\omega}_1$, $\dot{\vec{\omega}}_1$, $\vec{\omega}_2$, and $\dot{\vec{\omega}}_2$ denote the angular velocity and angular acceleration of the bottom and top link, respectively.

Solving (5.1)-(5.4) in sequence yields solutions for the joint reactions assuming knowledge (measurement) of all kinematical quantities, the link geometry and inertia properties. Table 1 reports the dimensions, mass, and principal moments of inertia for each link.

Parameter	Bottom	Top
Length (m)	0.305	0.356
Width (m)	0.051	0.051
Height (m)	0.019	0.019
Mass (kg)	0.834	0.908
I_1 (kg-m^2)	0.007	0.007
I_2 (kg-m^2)	0.007	0.010
I_3 (kg-m^2)	<0.001	<0.001

Table 5.1: Summary of dimensions, mass and principal moments of inertia for each link.

The kinematical quantities are measured or estimated from IMU data for the freely decaying pendular motion described in [105]. The IMU provides direct measurement of link angular velocity ($\vec{\omega}_1$, $\vec{\omega}_2$) and thus link angular acceleration ($\dot{\vec{\omega}}_1$, $\dot{\vec{\omega}}_2$) following numerical differentiation. The IMU also measures the acceleration at the center of the accelerometer polluted by gravity [4]. Conveniently, gravitational pollution in the measured acceleration is canceled in (5.1) and (5.2). However, solution of (5.2) and

[4] The MEMS accelerometers measure acceleration down to zero Hertz and therefore measure gravity in addition to the superimposed acceleration due to movement.

(5.4), and direct comparison of the calculated reactions to load cell measurements requires knowledge of the orientation of each link relative to frame G.

The orientation of each link is found from the orientation of the attached IMU and in two steps. The first step establishes the initial orientation of the IMU sense axes when the pendulum is in equilibrium. The second step determines the change in orientation upon integrating the link angular velocity during the subsequent oscillations. During the first step, the pendulum hangs at rest. The accelerometers measure solely the acceleration due to gravity thus establishing the initial direction of $\hat{E}_3^G$ in each IMU frame of reference. Next, the pendulum is displaced from equilibrium, released and oscillates freely with decaying amplitude. The angular velocity measured by the angular rate gyros establishes the orientation of the axis of rotation $\hat{E}_1^G$ which remains approximately fixed relative to the IMU frames. The average direction of the angular velocity is used to deduce the direction of $\hat{E}_1^G$ with respect to both IMU frames. Finally, the initial orientation of $\hat{E}_2^G$ resolved in the IMU frames follows from $\hat{E}_2^G = \hat{E}_3^G \times \hat{E}_1^G$. The initial direction cosine matrices that define the orientation of the IMU frames, ($\hat{e}_1^1,\ \hat{e}_2^1,\ \hat{e}_3^1$) and ($\hat{e}_1^2,\ \hat{e}_2^2,\ \hat{e}_3^2$), relative to frame G ($\hat{E}_1^G,\ \hat{E}_2^G,\ \hat{E}_3^G$) follow immediately from the components of $\hat{E}_1^G,\ \hat{E}_2^G$ and $\hat{E}_3^G$ established by this procedure. The components of each direction cosine matrix also establishes the initial values of the Euler parameters per

$$R = \begin{bmatrix} \varepsilon_1^{\,2} - \varepsilon_2^{\,2} - \varepsilon_3^{\,2} + \varepsilon_4^{\,2} & 2\left(\varepsilon_1\varepsilon_2 - e_3 e_4\right) & 2\left(\varepsilon_1\varepsilon_3 + \varepsilon_2\varepsilon_4\right) \\ 2\left(\varepsilon_1\varepsilon_2 + e_3 e_4\right) & \varepsilon_2^{\,2} - \varepsilon_1^{\,2} - \varepsilon_3^{\,2} + \varepsilon_4^{\,2} & 2\left(\varepsilon_2\varepsilon_3 - \varepsilon_1\varepsilon_4\right) \\ 2\left(\varepsilon_1\varepsilon_3 - \varepsilon_2\varepsilon_4\right) & 2\left(\varepsilon_2\varepsilon_3 + \varepsilon_1\varepsilon_4\right) & \varepsilon_3^{\,2} - \varepsilon_1^{\,2} - \varepsilon_2^{\,2} + \varepsilon_4^{\,2} \end{bmatrix} \tag{5.5}$$

for subsequent use in the second step.

During the second step, the evolution of the Euler parameters from the initial condition above is governed by the differential equation

$$\begin{bmatrix} \dot{\varepsilon}_1 \\ \dot{\varepsilon}_2 \\ \dot{\varepsilon}_3 \\ \dot{\varepsilon}_4 \end{bmatrix} = \frac{1}{2} \begin{bmatrix} 0 & \omega_3(t) & -\omega_2(t) & \omega_1(t) \\ -\omega_3(t) & 0 & \omega_1(t) & \omega_2(t) \\ \omega_2(t) & -\omega_1(t) & 0 & \omega_3(t) \\ -\omega_1(t) & -\omega_2(t) & -\omega_3(t) & 0 \end{bmatrix} \begin{bmatrix} \varepsilon_1 \\ \varepsilon_2 \\ \varepsilon_3 \\ \varepsilon_4 \end{bmatrix} \tag{5.6}$$

where ω_1, ω_2, and ω_3 are the three components of the measured angular velocity. This ordinary differential equation is integrated forward in time using standard numerical integration techniques subject to the Euler parameter normalization constraint $\varepsilon_1^2+\varepsilon_2^2+\varepsilon_3^2+\varepsilon_4^2=1$ at each time step. Doing so provides the Euler parameters as functions of time during the subsequent oscillations of the pendulum and therefore the orientation of the upper and lower links.

Small errors in rate gyro calibration and sensitivity to temperature subject the Euler parameters to an accumulation of error over time known as drift [61,75]. One can correct for drift by fusing accelerometer and rate gyro derived estimates of orientation via a Kalman or complementary filter [61,75]. In this study, we instead exploit the constraint that the pendulum oscillates about its equilibrium position to correct for drift. In particular, the Euler parameters must also oscillate about their initial (equilibrium) values.

The direction cosine matrix $R_1(t)$ defines a rotation, at every instant in time, from the bottom link IMU measurement frame to the G frame according to

$$v\big|_G = R_1(t)\, v\big|_{\hat{e}_1^1,\hat{e}_2^1,\hat{e}_3^1} \tag{5.7}$$

where $v\big|_G$ is a generic vector resolved in the G frame and $v\big|_{\hat{e}_1^1,\hat{e}_2^1,\hat{e}_3^1}$ is the same generic vector resolved in the bottom link IMU measurement frame. A similar rotation, $R_2(t)$, can be developed for the top link. It is important to note that $R_1(0)$ and $R_2(0)$ provide the fixed rotation from the bottom link IMU measurement frame to frame B and from the top link IMU measurement frame to frame T respectively.

Having defined the orientations of each IMU relative to gravity, we then use IMU derived data to define the mass center acceleration of each link, polluted by gravity, according to

$$\vec{a}_{c1} = \vec{a}_{m1} + \dot{\vec{\omega}}_1 \times \vec{r}_{c1/a1} + \vec{\omega}_1 \times \left(\vec{\omega}_1 \times \vec{r}_{c1/a1}\right) \tag{5.8a}$$

$$\vec{a}_{c2} = \vec{a}_{m2} + \dot{\vec{\omega}}_2 \times \vec{r}_{c2/a2} + \vec{\omega}_2 \times \left(\vec{\omega}_2 \times \vec{r}_{c2/a2}\right) \tag{5.8b}$$

where $\vec{a}_{m1}$ and $\vec{a}_{m2}$ is the acceleration measured by the bottom and top link accelerometers, respectively, and $\vec{r}_{c1/a1}$ and $\vec{r}_{c2/a2}$ are position vectors locating the mass

center of the bottom and top links relative to their respective accelerometers. These position vectors are unknown and, in principal, difficult to determine. However, each of the unknown position vectors can be written as the sum of two more accessible vectors. Considering the position vector associated with the bottom link for example,

$$\vec{r}_{c1/a1} = \vec{r}_{j1/a1} + \vec{r}_{c1/j1} \tag{5.9}$$

where $\vec{r}_{j1/a1}$ is the position of j_1 relative to the accelerometer, and $\vec{r}_{c1/j1}$ is the position of the link mass center relative to the joint. In human subject-based studies $\vec{r}_{c1/j1}$ is assumed from anthropometric data (or an alternative approach [106]) and $\vec{r}_{j1/a1}$ is estimated based on methods like those presented in [107]. In this study a coordinate measuring machine (MicroScribe G2x, positional accuracy/resolution of 0.23/0.13 mm) is used to measure $\vec{r}_{j1/a1}$, and $\vec{r}_{c1/j1}$ is initially defined such that the mass center is coincident with the geometric center of the link.

The definition of link mass center location provides the final piece of information needed to solve (5.1)-(5.4) in sequence for the reaction forces and moments acting at each joint of the pendulum. To compare these reaction estimates to the load cell-measured values, we first need to resolve the two quantities in the same frames of reference. The equations detailing the specific use of IMU measured acceleration and angular velocity for estimating the reaction forces and moments resolved in frames of reference consistent with the load cell data are presented in their entirety in the Appendix (Section 5.5).

5.3. Results and Discussion

The experiment and methods described above and in the companion paper [105] provide a means for benchmarking the accuracy of inertial measurements for estimating reactions acting at the joints of a multibody system. This section aims to provide intermediate results which build to a careful benchmark of this technology for inverse dynamic modeling of a double pendulum. We open with an example of the IMU data collected during one of the trials considered in our analysis. From there we demonstrate the accuracy of the calculated link orientation as compared to optical encoder-measured link angles. Having established this accuracy, we then present calculated reactions at j_1

and j_2 assuming collocated link geometric and mass centers. We go on to demonstrate that small changes in mass center location can improve the accuracy of the predicted joint reactions considerably. We open now with the IMU-measured acceleration and angular velocity for one of the trials considered.

5.3.1. IMU Data and Link Orientation

As described in [105], IMU data is sampled during the freely decaying oscillation of the double pendulum. Figure 5.3 illustrates an example of this IMU data for the bottom link during one of the ten trials considered. Three components of acceleration (Fig. 5.3A) and angular velocity (Fig. 5.3B) are plotted as functions of time, where the blue, green, and red curves correspond to data resolved along the $\hat{e}_1^1$, $\hat{e}_2^1$, and $\hat{e}_3^1$ sense axes, respectively.

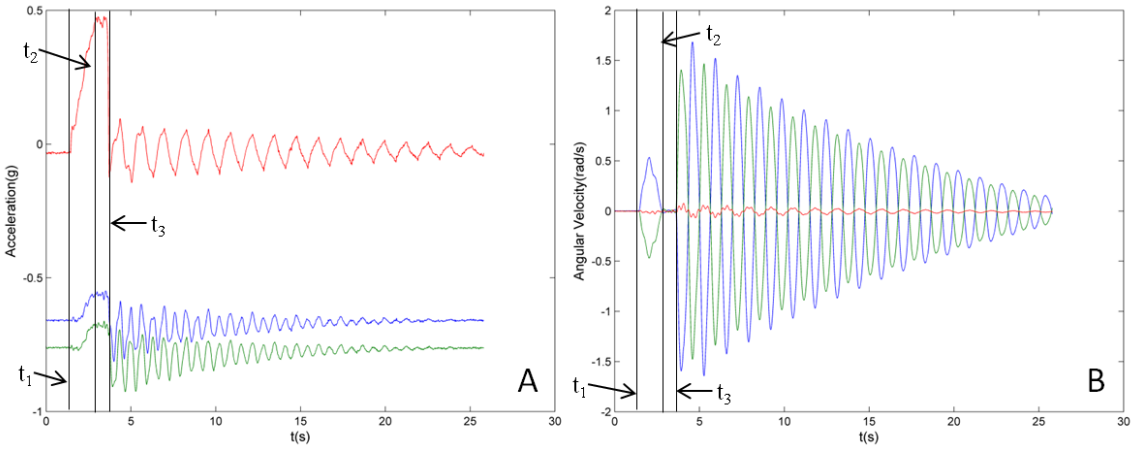

Figure 5.3: IMU acceleration (A) and angular velocity (B) history for an example trial sampled from the bottom link IMU. The pendulum begins at rest in its stable equilibrium position ($t < t_1$), is perturbed from this position by hand ($t_1 < t < t_2$) and then released ($t = t_3$).

The behavior of the pendulum during this trial is immediately discernible in Fig. 5.3. Specifically, the pendulum remains at rest in its stable equilibrium position ($t < t_1$), is perturbed from this position by hand and held stationary ($t_2 < t < t_3$), and released ($t = t_3$) and allowed to oscillate freely about equilibrium ($t > t_3$). Note that the accelerometer

measures the acceleration due to gravity at the start of the trial while the pendulum is at rest. As described above, we exploit this fact to determine the initial orientation of the IMU frames prior to subsequent integration of (5.6). This integration provides the (drift-polluted) estimate of the orientation of each link throughout the remainder of the trial. Figure 5.4 illustrates the uncorrected (drift-polluted) estimates of the four Euler parameters for the bottom link (gray curves) as well as their drift corrected values (colored curves) from the start of the example trial until 10 seconds after t_3.

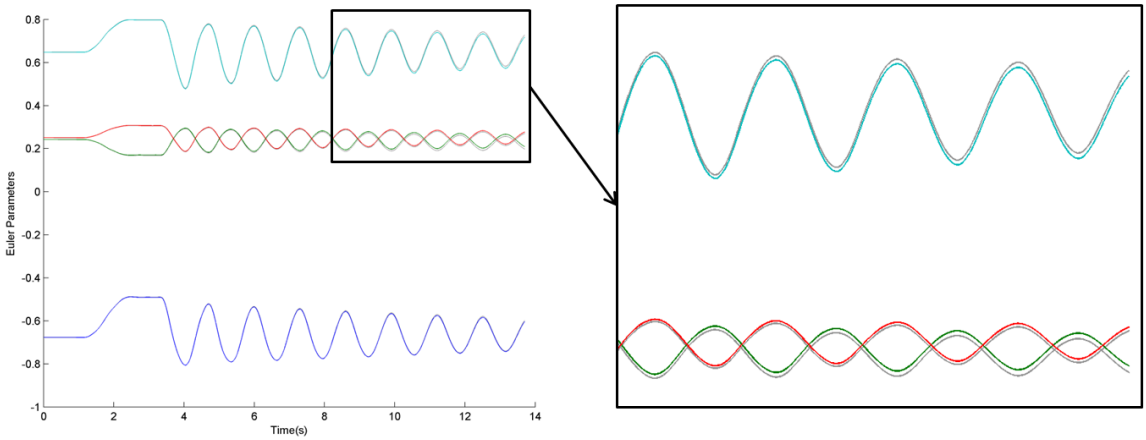

Figure 5.4: Drift polluted (gray) and corrected (colored) Euler parameters defining the orientation of the bottom link up until 10 seconds after t_3 during the example trial.

While the difference between the corrected and drift polluted Euler parameters during the first 10 seconds of oscillation is quite modest, the drift correction ensures that each Euler parameter oscillates about its initial value as required by the constrained motion of the pendulum. We confirm the accuracy of the corrected Euler parameters by using them to construct the angle formed by the major axis of each link ($\hat{E}_3^B$ and $\hat{E}_3^T$) and gravity ($\hat{E}_3^G$). As described in [105], these angles are also measured by the optical encoders which provide the truth data for comparison with the estimates based on IMU data. The mean and standard deviation of the root mean squared error (RMSE) and the correlation coefficient (r) between the encoder-measured and IMU-calculated angles for all ten trials are reported in Table 5.2. A similar analysis, assuming planar motion, is presented in [105]. The results confirm that link orientation based on integrating IMU

data remains an excellent estimate of the true orientation as directly measured by the encoders (RMSE $\leq$ 1.6 deg. and r $\geq$ 0.998).

	Bottom		Top	
Parameter	RMSE (deg)	r	RMSE (deg)	r
Mean (SD)	1.54 (0.24)	1.00 (<0.001)	0.87 (0.22)	1.00 (<0.001)

Table 5.2: Mean and standard deviation of root mean square error (RMSE) and correlation coefficient (r) between IMU-calculated link angles and encoder-measured link angles for all ten trials.

5.3.2. IMU-Derived Estimates of Joint Reactions

Having established the accuracy of the IMU-derived orientation estimates, we turn to the focus of this paper which is to evaluate the accuracy of IMU-derived estimates of joint reactions. We open with a presentation of the calculated reactions at j_2 which result from link mass center locations that are collocated with the geometric center of each link. For an example trial, the three components of load cell measured force (Fig. 5.5A) and moment (Fig. 5.5B) at j_2 are shown as dashed curves while the IMU derived force and moment are shown as the solid curves in Figure 5.5. The blue, green, and red curves correspond to reactions resolved along the $\hat{E}_1^G$, $\hat{E}_2^G$, and $\hat{E}_3^G$ directions respectively.

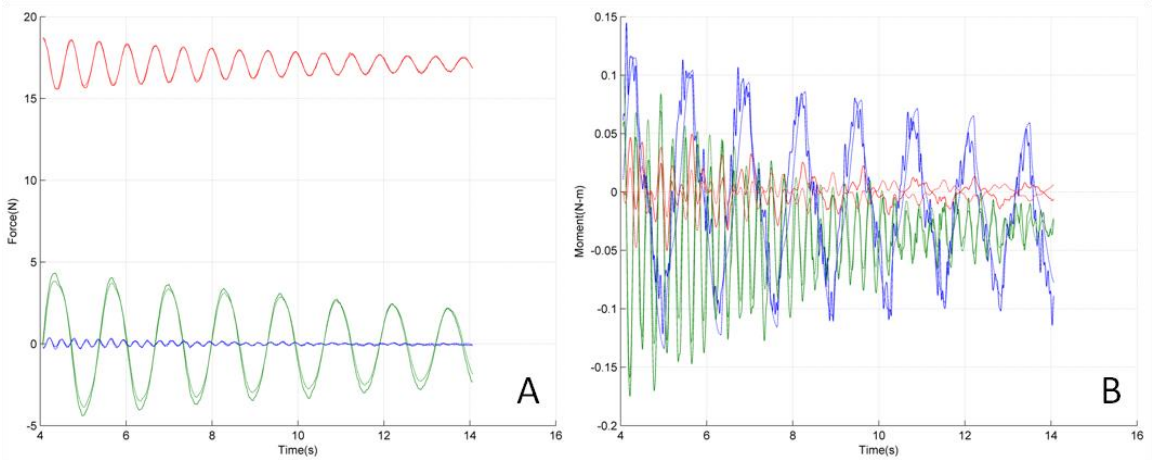

Figure 5.5: Reaction force (A) and moment (B) at j_2 as measured by the load cells (dashed) and estimated using IMU data (solid). The three colors distinguish components resolved in frame G: blue= $\hat{E}_1^G$, green= $\hat{E}_2^G$, and red= $\hat{E}_3^G$.

As noted above, Figure 5.5 provides a comparison between the load cell measured components of the force and moment acting at j_2 and those predicted from inverse dynamic modeling. The agreement in the three components of force is outstanding and it is difficult to discern the difference between the solid (IMU) and dashed (load cell) curves. For this trial, the $\hat{E}_2^G$ component (green curve) of the predicted reaction force has the maximum root mean squared error (RMSE) of 3.3% relative to the weight of the top link. By contrast, there are clearly discernible differences between the IMU predicted moment components and those measured by the load cell. The difference is particularly observable for the moment acting about the vertical axis ($\hat{E}_3^G$, red curve in Fig 5.5B, see Time = 10-14s for example) which has an RMSE of 3.0% relative to the restoring moment acting on the top link at the start of the trial. This restoring moment is defined as the moment acting at j_2 due to the top link's weight and orientation at the instant before the pendulum is released from its perturbed position ($t = t_3$). To provide a comparison in agreement between IMU and load cell derived force and moment we normalize the force components by the weight of each link and the moment components by the initial restoring moment due to the weight of each link. After normalization, the non-dimensional force and moment components predicted by the IMU can be plotted against those measured by the load cell to visualize the level of agreement between the measured

and predicted reactions. The resulting plots, after subtracting the mean of each component, are included in Figure 5.6. The blue, green and red curves again distinguish components along the $\hat{E}_1^G$, $\hat{E}_2^G$, and $\hat{E}_3^G$ directions, respectively.

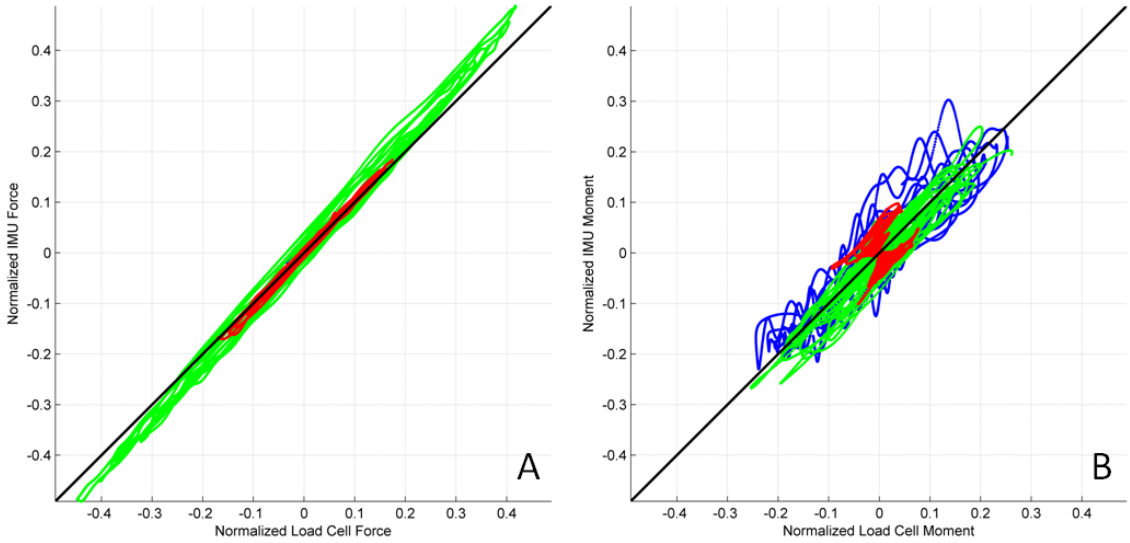

Figure 5.6: Three components of normalized force (A) and moment (B) acting at j_2 as predicted by IMU-enabled inverse dynamic modeling plotted against those measured directly by the load cell. The three colors distinguish components resolved in frame G: blue= $\hat{E}_1^G$, green= $\hat{E}_2^G$, and red= $\hat{E}_3^G$.

Figure 5.6A shows the three components of normalized force as determined from IMU data plotted against those measured by the load cell at j_2, while Fig. 5.6B shows the three normalized moment components plotted against each other. In Fig. 5.6A and B, the black line has zero intercept and unit slope. These results reinforce the excellent agreement between reaction force prediction and measurement with a minimum correlation coefficient of 0.90 ($\hat{E}_1^G$ direction). As suggested in Fig. 5.5B, these results also illustrate the limited agreement between the measured and predicted reaction moments, which have a minimum correlation coefficient of 0.21 ($\hat{E}_3^G$ direction) for this trial. To provide a summary for the ten trials considered in this analysis we present the mean (standard deviation) of the correlation coefficient (r) and the RMS error (RMSE,

percentage of normalizing factor) between the IMU estimates of force and moment and those measured by the load cells at j_1 and j_2 in Table 5.3.

Joint	j_1					
	$\vec{F}_1$			$\vec{M}_1$		
Direction	$\hat{E}_1^T$	$\hat{E}_2^T$	$\hat{E}_3^T$	$\hat{E}_1^T$	$\hat{E}_2^T$	$\hat{E}_3^T$
RMSE (%)	0.51 (0.09)	1.92 (0.39)	0.60 (0.16)	1.12 (0.19)	0.81 (0.19)	0.17 (0.02)
r	0.96 (0.03)	0.99 (0.01)	1.00 (<0.01)	0.96 (0.01)	0.98 (0.01)	0.87 (0.07)
Joint	j_2					
	$\vec{F}_2$			$\vec{M}_2$		
Direction	$\hat{E}_1^G$	$\hat{E}_2^G$	$\hat{E}_3^G$	$\hat{E}_1^G$	$\hat{E}_2^G$	$\hat{E}_3^G$
RMSE (%)	0.76 (0.13)	4.61 (0.84)	1.16 (0.37)	6.38 (1.37)	3.61 (0.74)	3.19 (0.14)
r	0.95 (0.03)	1.00 (<0.01)	1.00 (<0.01)	0.88 (0.04)	0.97 (0.02)	0.58 (0.25)

Table 5.3: Mean (standard deviation) of RMS difference (RMSE) and correlation coefficient (r) for IMU-derived force and moment components compared to those measured by the load cells at j_1 and j_2 for the 10 trials of pendulum data considered and collocated link geometric and mass centers.

The results in Table 5.3 demonstrate that IMU-based inverse dynamic modeling is able to predict force components to within 4.7% RMS of their measured values on average as compared to the weight of each pendulum link and have correlation coefficients greater than 0.95 on average. In contrast, IMU-based inverse dynamic modeling is only able to predict moment components to within 6.4% RMS of their measured values on average as compared to the initial restoring moment acting on each link and have correlation coefficients greater than only 0.58. Possible causes for the error in the predicted force and moment include small errors in the assumed physical properties of each link (mass, moment of inertia, etc.), small misalignments between the measured and IMU derived force and moment components, and small errors in the calibration of the IMUs.

5.3.3. Sensitivity of Joint Reactions to Mass Center Location

Another potential cause for the discrepancy between the measured and predicted moment components is the sensitivity of the technique to small errors in mass center position [11,108]. To investigate this possible source of error, the mass center position is altered slightly from its assumed location coincident with the geometric center of each link. To determine the new mass center location, we begin with the analysis presented in [105] which assumes that each mass center lies along the major axis of the link and determines its location along that axis by observing the frequency of oscillation of the pendulum. We extend this estimate by allowing the mass center location to have components along the minor and intermediate principal axes as well. These two transverse components of the center of mass location are estimated by considering the relationship between the measured reaction force at each joint and the kinematics of each link defined in (5.1) and (5.2). We rewrite (5.1) and (5.2) in terms of the absolute link angular velocities and accelerations ($\vec{\omega}_1,\ \vec{\omega}_2,\ \dot{\vec{\omega}}_1,\ \dot{\vec{\omega}}_2$) determined from successive differentiations of the encoder angle measurements, arriving at

$$\vec{F}_1 = m_1\left[\dot{\vec{\omega}}_2 \times \vec{r}_{j1/j2} + \vec{\omega}_2 \times \left(\vec{\omega}_2 \times \vec{r}_{j1/j2}\right) + \dot{\vec{\omega}}_1 \times \vec{r}_{c1/j1} + \vec{\omega}_1 \times \left(\vec{\omega}_1 \times \vec{r}_{c1/j1}\right) - \vec{g}\right] \tag{5.10}$$

$$\vec{F}_2 = \vec{F}_1 + m_2\left[\dot{\vec{\omega}}_2 \times \vec{r}_{c2/j2} + \vec{\omega}_2 \times \left(\vec{\omega}_2 \times \vec{r}_{c2/j2}\right) - \vec{g}\right] \tag{5.11}$$

where $\vec{F}_1$ and $\vec{F}_2$ are the reaction forces measured by the load cells, and $\vec{r}_{j1/j2}$ is the location of j_1 relative to j_2 as measured using the coordinate measuring machine. Equations (5.10) and (5.11) can be written for each data point during free oscillation of the pendulum and the resulting system of equations is solved for the remaining unknown mass center positions, $\vec{r}_{c1/j1}$ and $\vec{r}_{c2/j2}$, using standard least squares. From this analysis, the new mass center locations are $\vec{r}_{c1/j1} = \left[-0.001,\ 0.0027,\ -0.1522\right]$ and $\vec{r}_{c2/j2} = \left[-0.0233,\ -0.0111,\ -0.1891\right]$. This represents a 0.9% and 7.9% change from the geometric center of the bottom and top link, respectively, relative to the length of each link. This small change in mass center location produces a significant change in the reaction moment predicted via inverse dynamic modeling as evidenced by Figure 5.7,

where the predicted and measured force and moment components at j_1 (Fig. 5.7A/B) and j_2 (Fig. 5.7C/D) are plotted against time for the same trial considered above.

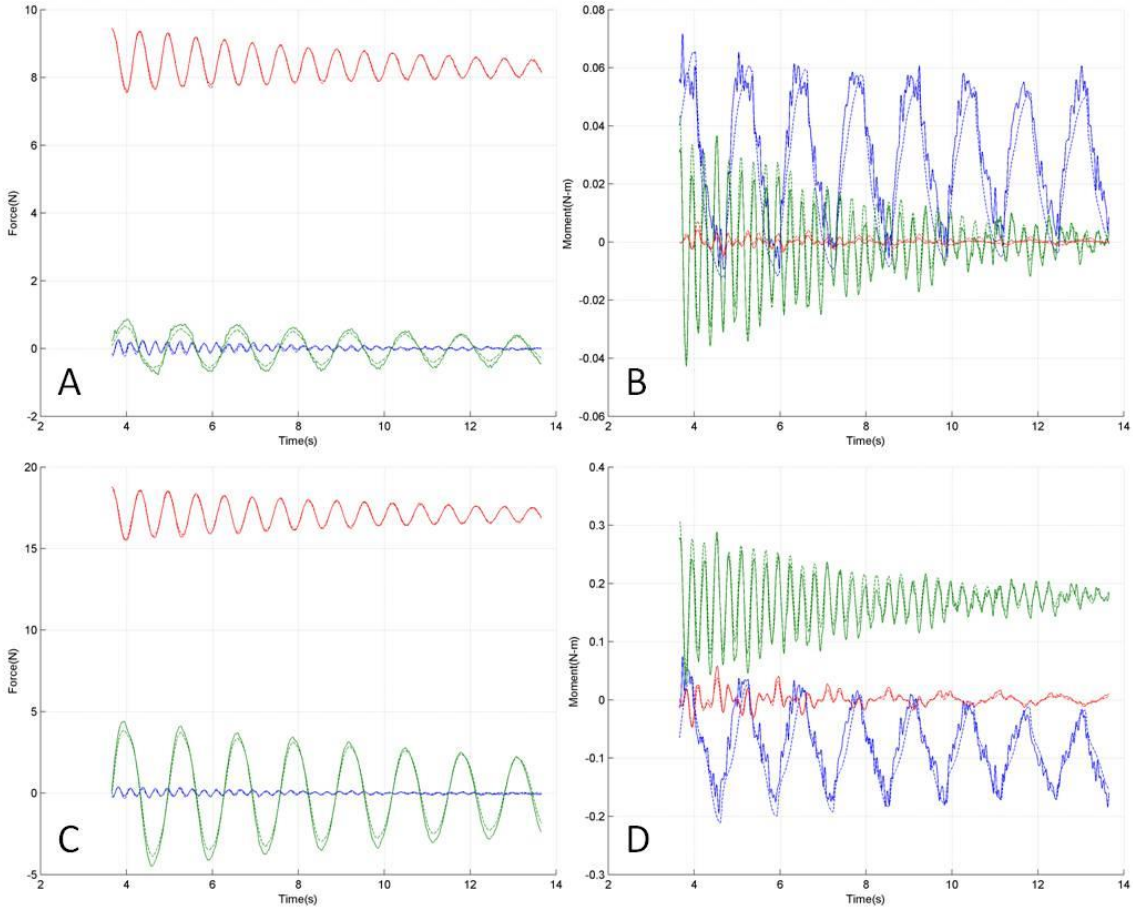

Figure 5.7: Force (A) and moment (B) components at j_1 and force (C) and moment (D) components at j_2 for updated mass center positions. Solid curves correspond to IMU-predicted reactions while dashed curves correspond to load cell measurements.

The three components of load cell measured force (Fig. 5.7A/C) and moment (Fig. 5.7B/D) are shown as dashed curves while the IMU derived force and moment are shown as solid curves. The reactions at j_1 are presented in Fig. 5.7A/B, where the blue, green, and red curves correspond to reactions resolved along the $\hat{E}_1^T$, $\hat{E}_2^T$, and $\hat{E}_3^T$ directions respectively. The reactions at j_2 are presented in Fig. 5.7C/D and can be compared directly to the results presented in Figure 5.5. Qualitatively the agreement between predicted and measured reaction force is similar, and reaction moment is

improved with the new mass center location. The maximum RMSE in the predicted force components at j_2 for this trial decreases to 2.1% ($\hat{E}_2^G$ direction, 3.3% initially) of the weight of the top link. Similarly, the RMS error in the $\hat{E}_3^T$ component of the reaction moment decreases to 1.4% (red curve, 3.0% initially). To explore the updated results further, we again present normalized predicted force and moment components plotted against their measured values, subtracting the mean from each component, in Figure 5.8.

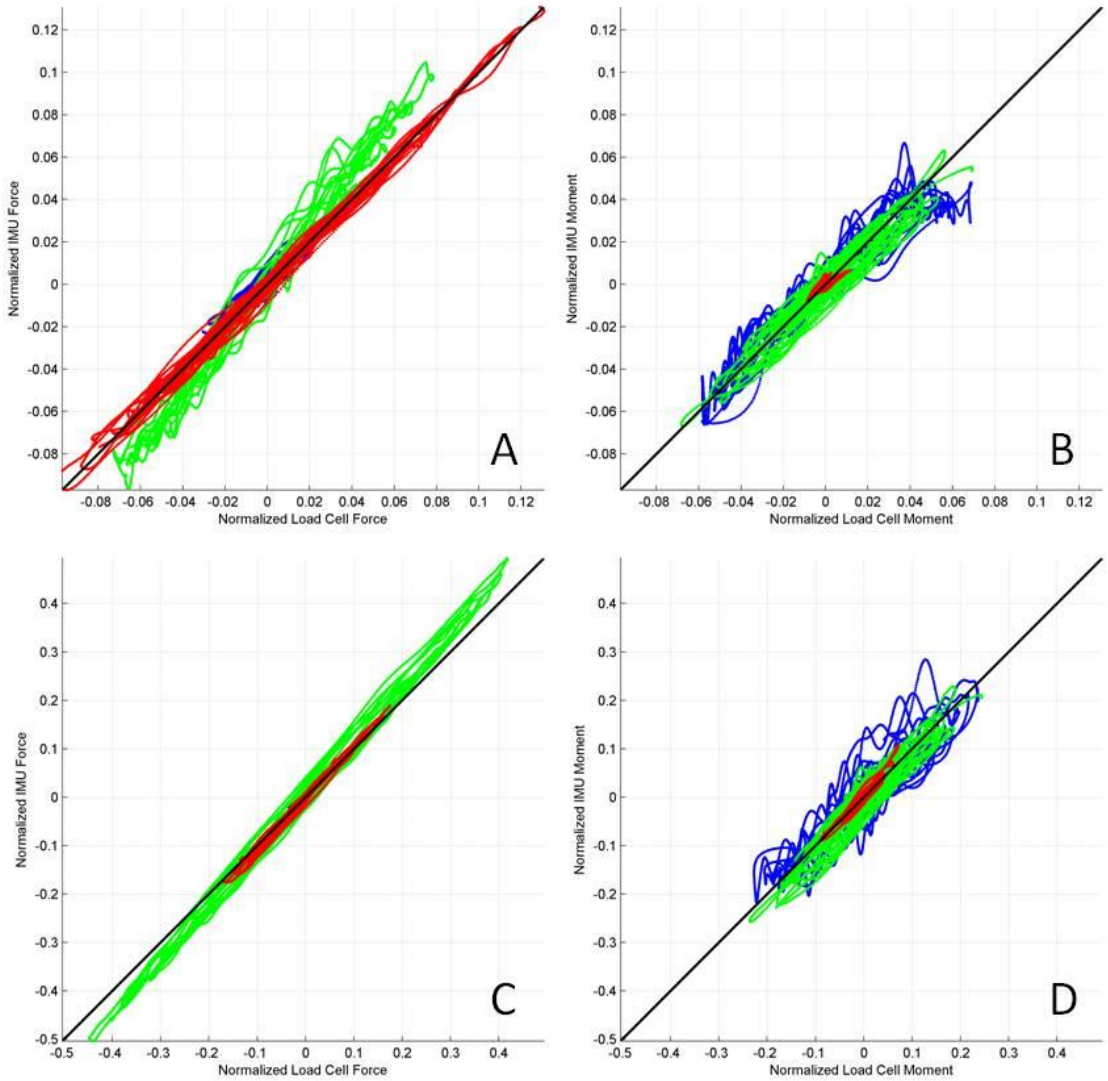

Figure 5.8: Force (A) and moment (B) at j_1 and force (C) and moment (D) at j_2 for updated mass center positions.

As presented in Fig. 5.6, the three components of normalized predicted force (Fig. 5.8A/C) and moment (Fig. 5.8B/D) are plotted against those measured by the load cell at j_1 (Fig. 5.8A/B) and j_2 (Fig. 5.8C/D). Direct comparison of the measured and predicted reaction moments at j_2 for the two mass center locations considered (i.e. comparison of Fig. 5.8C/D to Fig. 5.6A/B) reveals a qualitative improvement in agreement between moment components during this trial. Specifically, the minimum correlation between the predicted and measured components of reaction moment at j_2 increases to 0.75 (0.22 initially). In contrast, the minimum correlation between the predicted and measured reaction force components at j_2 stays nearly constant at 0.88 (0.90 initially) with the altered mass center location. To investigate the effect of mass center location on the entire dataset, the mean (SD) RMS error and correlation coefficient for the 10 trials considered are reported in Table 5.4.

Joint	j_1					
	$\vec{F}_1$			$\vec{M}_1$		
Direction	$\hat{E}_1^T$	$\hat{E}_2^T$	$\hat{E}_3^T$	$\hat{E}_1^T$	$\hat{E}_2^T$	$\hat{E}_3^T$
RMSE (%)	0.51 (0.09)	1.92 (0.40)	0.61 (0.19)	1.18 (0.21)	0.81 (0.19)	0.19 (0.03)
r	0.96 (0.03)	0.99 (0.01)	1.00 (<0.01)	0.95 (0.02)	0.98 (0.01)	0.84 (0.07)
Joint	j_2					
	$\vec{F}_2$			$\vec{M}_2$		
Direction	$\hat{E}_1^G$	$\hat{E}_2^G$	$\hat{E}_3^G$	$\hat{E}_1^G$	$\hat{E}_2^G$	$\hat{E}_3^G$
RMSE (%)	0.77 (0.14)	4.99 (0.85)	1.23 (0.37)	5.83 (1.22)	3.25 (0.69)	0.99 (0.21)
r	0.95 (0.023)	1.00 (<0.01)	1.00 (<0.01)	0.88 (0.04)	0.98 (0.02)	0.97 (0.01)

Table 5.4: Mean (standard deviation) of RMS difference (RMSE) and correlation coefficient (r) for IMU-derived force and moment components compared to those measured by the load cells at j_1 and j_2 for the 10 trials of pendulum data considered and updated mass center location.

As reported in Table 5.4, the updated mass center locations enable IMU-based inverse dynamic modeling to predict force components to within 5.0% RMS of their measured values as compared to the weight of each pendulum link and which have correlation coefficients greater than 0.95 on average. Moreover, the moment components

are predicted to within 5.8% RMS of their measured values (6.4% initially) as compared to the restoring moment acting on each link and have correlation coefficients greater than 0.84 (0.58 initially). This represents a substantial improvement in the average agreement between IMU-predicted reactions at each joint and their actual measured values for a minor change (less than 8% of the length of the link) in mass center location.

These results demonstrate the significant effect that small changes in mass center location can have on the accuracy of IMU-enabled inverse dynamic modeling-predicted reaction moments. This finding supports previous analyses based on human motion and MOCAP-enabled inverse dynamic modeling [11,14,108,109], where the effect of mass center location on predicted reaction moment was also demonstrated. In this experiment, we demonstrate this sensitivity as compared to a precise gold standard for an experiment constrained such that each segment is guaranteed to be rigid and rotating about a fixed axis. In human motion studies, these constraints no longer exist. Often, mass center location is estimated from anthropometric data, which can be inaccurate [110], and human body segments are more flexible than rigid resulting in a variable mass center location and center/axis of rotation during motion [111,112]. As a result, we believe that the agreement between load cell-measured and inverse dynamic modeling-predicted reaction moments presented here is a limiting case demonstrating the best possible accuracy achievable using this technique. In practice, we believe that one would experience larger errors.

5.4. Conclusion

In this work we provide results from an experiment benchmarking the use of inertial measurement units to provide the kinematic data necessary for predicting reaction forces and moments acting at the joints of a double pendulum. These predicted reactions are compared to reactions directly measured by highly precise miniature force and torque sensors. We demonstrate that for 10 trials, IMU-enabled inverse dynamic modeling is able to predict three components of reaction force to within 5.0% RMS of their measured values relative to the weight of each link of the pendulum with correlation coefficients greater than 0.95 on average. Similarly, IMU-enabled inverse dynamic modeling is able

to predict three components of reaction moment to within 5.9% RMS of their measured values relative to the restoring moment due to the weight of each link of the pendulum with correlation coefficients greater than 0.84 on average. We also highlight the sensitivity of the predicted moments to errors in mass center location demonstrating that a 0.9% and 7.9% change in the estimated location of the mass center for the bottom and top links respectively (relative to the length of each link) cause the maximum average RMS error in moment to rise to 6.4% and the minimum average correlation coefficient to drop to 0.58.

5.5. Appendix

In this appendix we present the equations used to calculate the reaction force and moment acting at each joint of the double pendulum from IMU data for comparison to load cell measurements. The reactions at j_1, resolved in frame T, are defined as

$$\vec{F}_1\big|_T = m_1 R_2^T R_1 \left[\vec{a}_{m1} + \dot{\vec{\omega}}_1 \times R_1^T(0)\vec{r}_{c1/a1} + \vec{\omega}_1 \times \left(\vec{\omega}_1 \times R_1^T(0)\vec{r}_{c1/a1} \right) \right] \tag{5.12}$$

$$\vec{M}_1\big|_T = R_2^T R_1 R_1^T(0) \left[I_{c1}\left(R_1(0)\dot{\vec{\omega}}_1 \right) + \left(R_1(0)\vec{\omega}_1 \right) \times I_{c1}\left(R_1(0)\vec{\omega}_1 \right) - \vec{r}_{c1/j1} \times \left(R_1^T R_2 \vec{F}_1\big|_T \right) \right] \tag{5.13}$$

where $\bullet|_T$ refers to a vector resolved in frame T, $R_1(0)$ is the fixed rotation from the bottom link IMU measurement frame to frame B, and the other variables are as defined in the body of the chapter. The reaction force and moment at j_2, resolved in frame G, are defined as

$$\vec{F}_2\big|_G = R_2 \left[R_2^T(0)\vec{F}_1\big|_T + m_2 \left(\vec{a}_{m2} + \dot{\vec{\omega}}_2 \times R_2^T(0)\vec{r}_{c2/a2} + \vec{\omega}_2 \times \left(\vec{\omega}_2 \times R_2^T(0)\vec{r}_{c2/a2} \right) \right) \right] \tag{5.14}$$

$$\vec{M}_2\big|_G = R_2 \left[I_{c2}\left(R_2(0)\dot{\vec{\omega}}_2 \right) + \left(R_2(0)\vec{\omega}_2 \right) \times I_{c2}\left(R_2(0)\vec{\omega}_2 \right) - \vec{r}_{c2/j2} \times \vec{F}_2\big|_T + \vec{M}_1\big|_T + \vec{r}_{c2/j1} \times \vec{F}_1\big|_T \right] \tag{5.15}$$

where $\bullet|_G$ refers to a vector resolved in frame G, $R_2(0)$ is the fixed rotation from the top link IMU measurement frame to frame T, and the other variables are as defined in the body of the chapter. The reaction force and moment defined in (5.12)-(5.15) are compared directly to the measured force and moment at each joint in the Results and Discussion section included above.

Chapter 6: Accurate Estimation of Joint Centers

6.1. Introduction

As noted in Chapter 5, the annual number of total hip and knee replacement surgeries are predicted to increase by over 170% (to 572,000) and 670% (to 3.48 million) respectively by the year 2030 [49]. An important contributor to the success of these surgeries is the accurate identification of the center-of-rotation (CoR) of the hip joint [50–53,113]. In total hip arthroplasty, expensive surgical navigation technologies or invasive manual techniques guide the location and orientation of the prosthesis [53]. For total knee arthroplasty, surgical navigation technologies provide an estimate of the location of the hip joint CoR to guide the placement and orientation of the implant [52]. Small errors in hip joint location may induce large errors in the orientation and location of joint prostheses which negatively impact both short- and long-term surgical success [51–53].

The alarming increase in joint replacements further motivates the need for non-invasive methods to identify pathological lower extremity motion before joint injuries occur. These methods also commonly require accurate location of the hip joint CoR for accurate estimation of segmental kinematics and kinetics [114–117]. For example, application of the inverse dynamic modeling technique presented in Chapter 5 to the hip, requires kinematic, inertial and geometric data for the femur and pelvis, including the location of the hip joint CoR, prior to estimating hip reactions [13]. The kinematic variables (segmental angular velocity, angular acceleration and centroidal acceleration) are typically measured using video-based motion capture, inertia properties are estimated from anthropometric data, and the position of segmental mass center relative to the CoR of the hip joint center is estimated using video-based methods.

Methods for determining joint CoR employ either anatomical or functional techniques. Anatomical techniques, common in joint replacement procedures, rely on imaging and computer-assisted surgical tools or palpation to define the location of bony landmarks from which the position of the joint CoR can be estimated [50–53]. Anatomical techniques can be expensive (requiring imaging and/or surgery), invasive, and error prone. Functional techniques, commonly employed in human biomechanics research, rely on motion capture to track the 3-D position of the body segments on either side of the joint during some prescribed motion. The relative motion of the segments provides the data needed to estimate the joint CoR [54–59].

Video-based functional techniques successfully identify the location of the CoR of a spherical joint to within 2.2 mm [57,58]. However, the required motion capture equipment and data processing requirements tend to be expensive and time consuming, thereby constraining use largely to research laboratory settings. Data lost by marker occlusion further undermines accuracy. Segment-mounted inertial measurement units (IMUs), which directly measure angular velocity and linear acceleration, may pose an attractive alternative to video-based motion capture for determining joint CoR. The advantages of IMUs derive from their low cost, portability (potential use outside the laboratory and in clinical settings), and high data fidelity.

For instance, the OrthAlign^{TM} knee align system uses a femur-mounted IMU to estimate the location of the CoR of the hip joint for total knee arthroplasty. This system computes CoR position using algorithms similar to those presented in [54–58] which rely on IMU-derived femur velocity and position estimates [60]. These estimates, obtained by successive integrations of the IMU-measured acceleration, are subject to error due to sensor drift [61].

To improve upon the IMU approach, we propose a new algorithm for estimating the CoR of a spherical joint that avoids any need for (error-prone) velocity and position estimates. This method utilizes solely the acceleration and angular velocity data directly measured by the IMU. The objective of this paper is to introduce this new algorithm and to demonstrate its accuracy via experimental benchmarking. We open by describing the experimental methods.

6.2. Methods

This study employs a highly miniaturized wireless IMU illustrated in Figure 6.1 which represents the latest in a series of designs developed for sports training and biomechanics studies; refer, for example, to [66,67,71,118].

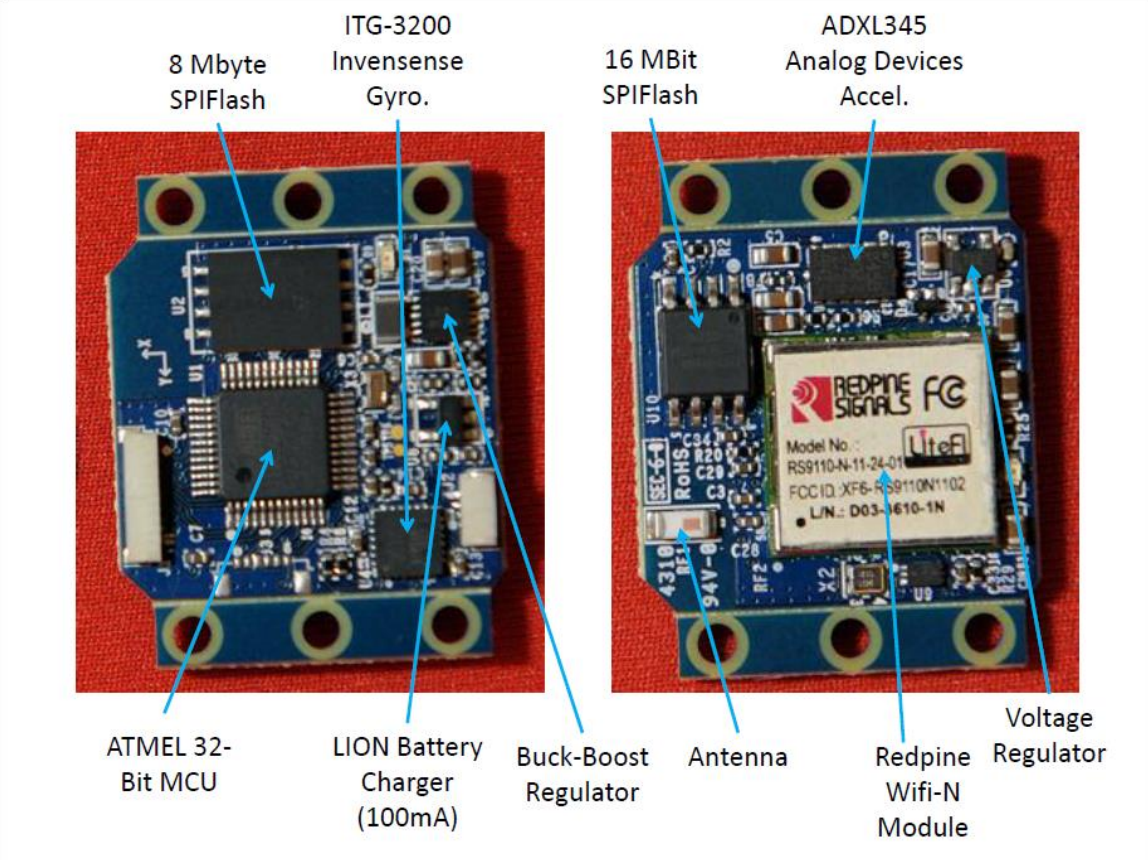

Figure 6.1: Two faces of the miniaturized, wireless IMU used in this study. Major components are labeled.

The IMU is equipped with a low-power Wi-Fi module which enables wireless data transmission over a standard Wi-Fi network broadcast by a Windows 7 computer. The design includes two sensing components. One is a digital tri-axial angular rate gyro, which performs internal 16-bit A/D conversion, with a measurement range of 2,000 deg/s, noise magnitude of 0.38 deg/s-rms for each axis (at 100 Hz output), and maximum sampling frequency of 512 Hz. The other is a digital tri-axial accelerometer, which

performs internal 13-bit A/D conversion, with a measurement range of 16 g, noise magnitude of 0.004 g-rms for each axis (at 100 Hz output), and maximum sampling frequency of 800 Hz. Data is logged in 8 Mbytes of onboard flash memory during each trial and is then transmitted and downloaded to the host computer upon trial completion. Before use, the IMU is calibrated according to the procedure detailed in [68]. The calibration, which consists of rotations about each of three orthogonal axes, determines 24 calibration parameters (including scale factors, cross-axis sensitivity scale factors, and biases) for the IMU. This process ensures that the acceleration and angular rate measurements are accurately resolved along a common orthogonal triad of unit vectors that define the sensor frame of reference (see below). Additionally, bias values for the angular rate gyro are updated at the start of every trial to ensure that any alterations due to environmental variations are determined.

The IMU above is attached to the experimental apparatus illustrated in Fig. 6.2 which serves as a mechanical approximation of a human hip joint (spherical joint). The joint is formed by a ball bearing (38 mm dia.) that seats in shallow spherical cavities machined into the proximal (black) and distal (white) halves of the joint; refer to Fig. 6.2A. A pair of tensioned o-rings provides joint pre-loading. The proximal (black) half is fastened to a table support while the distal half (white) forms a long appendage that may be freely manipulated; refer to Fig. 6.2B. The IMU (located at yellow frame of reference) is embedded in a calibration jig (black) at the end of this assembly. The calibration jig serves as a convenient means to attach the IMU with arbitrarily selected yet measurable position and orientation relative to the center of the bearing (i.e., the joint CoR). The reader could imagine the illustrated spherical joint as a coarse approximation of the human hip joint, where the proximal (black) and distal (white and ball bearing) sides of the joint correspond to the acetabular cup and femoral stem/head, respectively.

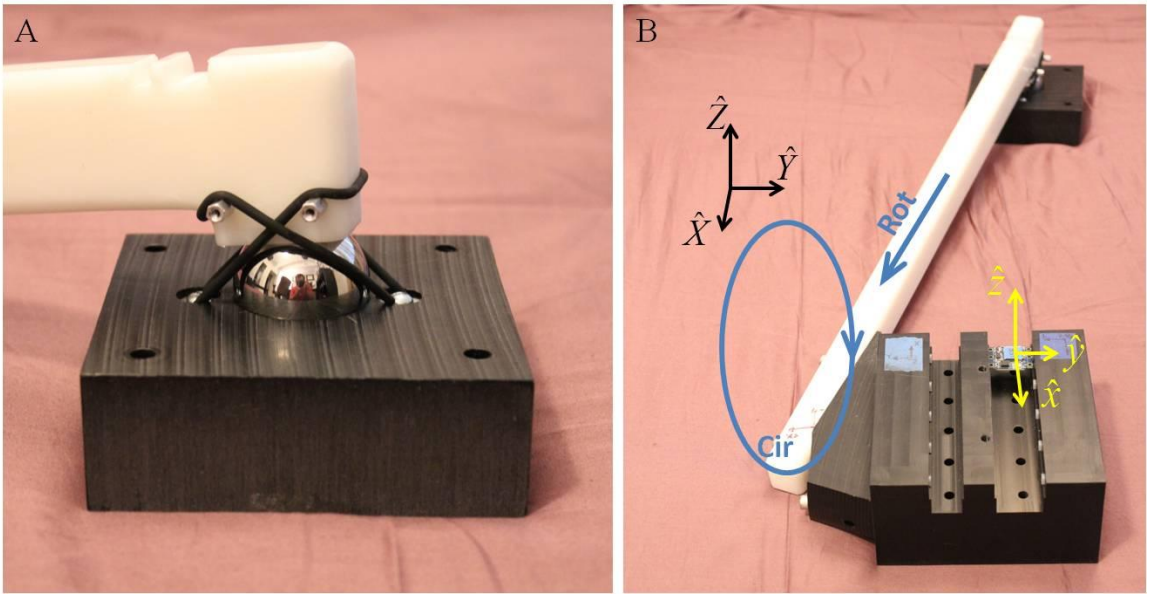

Figure 6.2: A mechanical approximation of a human "hip joint" (A) composed of a ball bearing (38 mm dia.) seated between two shallow spherical cavities. One cavity is machined in the proximal side of the joint (black) and the other is machined into the distal side (white). Stretched o-rings provide joint pre-loading. The extension of the distal side (B) supports a machined calibration jig (black) with the embedded wireless IMU.

The experimental procedure requires recording IMU-transmitted acceleration and angular velocity data while manipulating the "femur" as follows. Starting from rest, the femur is subject to two motions: a circumduction (Cir) motion and a rotation (Rot) motion with a pause in between; refer to Fig. 6.2B During circumduction, the end of the femur follows the illustrated (near circular) orbit which, in human subjects, would induce (near equal) extension-flexion and ab-adduction. During rotation, the femur is rotated about its long axis, which would induce (near pure) internal-external rotation in human subjects.

Following this motion sequence, the IMU acceleration and angular velocity data is transmitted to a host computer for subsequent data analysis. The analysis begins by removing the (constant) 1 g acceleration due to gravity that is detected by the accelerometer in addition to the superimposed acceleration due to motion. To this end, we introduce two frames of reference: an "IMU-fixed" frame denoted by the orthogonal triad of unit vectors ($\hat{x}, \hat{y}, \hat{z}$), and an inertial, "lab-fixed" frame denoted by the orthogonal triad of unit vectors ($\hat{X}, \hat{Y}, \hat{Z}$); refer to Fig. 6.2B. The acceleration and angular velocity

are measured in the IMU-fixed reference frame, while gravity is naturally defined in the lab-fixed frame by $-g\,\hat{Z}$. The acceleration imparted at the location of the accelerometer ($\vec{a}_a$) is recovered from the acceleration measured by the accelerometer ($\vec{a}_m$) per

$$\vec{a}_a = \vec{a}_m - g\hat{Z} \tag{6.1}$$

which further requires knowledge of the components of $\vec{a}_m$ in the lab-fixed frame. These components are deduced by first computing the direction cosine matrix that defines the orientation of the IMU-frame relative to the lab-fixed frame. The transformation (direction cosine matrix) that relates these two frames (Λ) and the differential equation that governs its evolution over time are

$$\vec{v}\,|_{\hat{X},\hat{Y},\hat{Z}} = \Lambda \vec{v}\,|_{\hat{x},\hat{y},\hat{z}} \tag{6.2}$$

$$\frac{d\Lambda}{dt} = \Lambda \hat{\bar{\omega}} \tag{6.3}$$

where Λ follows the standard definition of a direction cosine matrix (DCM) [73], $\vec{v}\,|_{\hat{x},\hat{y},\hat{z}}$ denotes the components of a vector $\vec{v}$ resolved in the IMU-fixed frame, and $\vec{v}\,|_{\hat{X},\hat{Y},\hat{Z}}$ denotes the components of the same vector resolved in the lab-fixed frame. The DCM is a function of the femoral angular velocity, and is computed upon integrating (6.3) following an adaptation of the algorithm in [74]. The adapted algorithm employs a numerical approximation to (6.3) in which $d\Lambda/dt$ denotes the time derivative of the DCM and $\hat{\bar{\omega}}$ denotes the IMU-fixed angular velocity vector in skew-symmetric form. The midpoint approximation to the solution of (6.3) yields the DCM at time step *n+1* in terms of its value at time step *n* per

$$\Lambda_{n+1} = \Lambda_n \left[\mathrm{I} + \tfrac{1}{2}\Delta\hat{\bar{\theta}}_{n+\frac{1}{2}} \right] \left[\mathrm{I} - \tfrac{1}{2}\Delta\hat{\bar{\theta}}_{n+\frac{1}{2}} \right]^{-1} \tag{6.4}$$

In Equation (6.4), $\Delta\hat{\bar{\theta}}_{n+\frac{1}{2}}$ denotes the midpoint approximation of the change in orientation from time step *n* to *n+1* in skew-symmetric form defined by

$$\Delta\hat{\bar{\theta}}_{n+\frac{1}{2}} = \tfrac{1}{2}\Delta t \left(\hat{\bar{\omega}}_{n+1} + \hat{\bar{\omega}}_n \right) \tag{6.5}$$

where $\hat{\bar{\omega}}_{n+1}$ and $\hat{\bar{\omega}}_n$ are the (measured) IMU-fixed angular velocities at time steps *n+1* and *n* respectively in skew-symmetric form, and Δt is the time interval between time

steps *n* and *n+1*. Note that the IMU provides the IMU-fixed angular velocity needed to solve for $\Lambda(t)$, via Equations (6.4)-(6.5) provided an initial value, $\Lambda(0)$, is also known. This initial value is determined by holding the femur still at the start of a trial and then employing the accelerometer as an inclinometer following the procedure detailed in [67]. Following these steps ultimately allows one to compute $\vec{a}_a$ from Equation (6.1) and to also resolve $\vec{a}_a$ in the IMU-fixed frame of reference for use in the following acceleration analysis.

Assuming a rigid femur, the acceleration of the femur-mounted accelerometer $\vec{a}_a$ is related to that of the center of the spherical joint $\vec{a}_c$ through

$$\vec{a}_a = \vec{a}_c + \frac{d\vec{\omega}}{dt} \times \vec{r}_{a/c} + \vec{\omega} \times (\vec{\omega} \times \vec{r}_{a/c}) \tag{6.6}$$

where $\vec{\omega}$ is the measured femoral angular velocity, $d\vec{\omega}/dt$ is the computed femoral angular acceleration (via numerical differentiation of $\vec{\omega}$), and $\vec{r}_{a/c}$ is the desired but unknown position of the accelerometer relative to the center of the spherical joint. If one assumes that the spherical joint forms the pivot of a spherical pendulum, then $\vec{a}_c = 0$ and eq. (6.6) is linear in the remaining unknown $\vec{r}_{a/c}$. Moreover, if one writes eq. (6.6) for each of n samples of IMU data, then a solution for $\vec{r}_{a/c}$ can be found using standard least squares.

To demonstrate the accuracy of the proposed algorithm for determining $\vec{r}_{a/c}$, we present results from benchmarking CoR estimates from 28 trials using IMU data with CoR estimates from 14 trials using a digital coordinate measuring machine (CMM - MicroScribe G2X). This CMM, which has positional accuracy of 0.23 mm and resolution of 0.13 mm, is used to digitize the location of the center of the accelerometer and 40 points on the surface of the ball bearing (serving as the analog for the femoral head). Points on the calibration jig shown in Fig. 6.2B are also digitized to define the orientation (direction cosine matrix) of the IMU-fixed reference frame relative to the measurement frame of the CMM. This collection of 3-D positions recorded by the CMM are used as input to a surface fitting algorithm that calculates the surface of the bearing and, from this, the true position of the center of the spherical joint relative to the center

of the accelerometer (and relative to the IMU-fixed reference frame) $\vec{r}_{c/a}$. The results from this careful benchmarking experiment are described next.

6.3. Results & Discussion

6.3.1. Ideal Joint Behavior

The experiment and methods above consider an ideal spherical joint defined by an IMU rigidly attached to a rigid femur. This establishes an important limiting case for assessing the accuracy of the new IMU-based method for determining joint CoR. Moreover, this also establishes a direct comparison to a benchmarking study for video-based methods [58] which employs a similar mechanical joint.

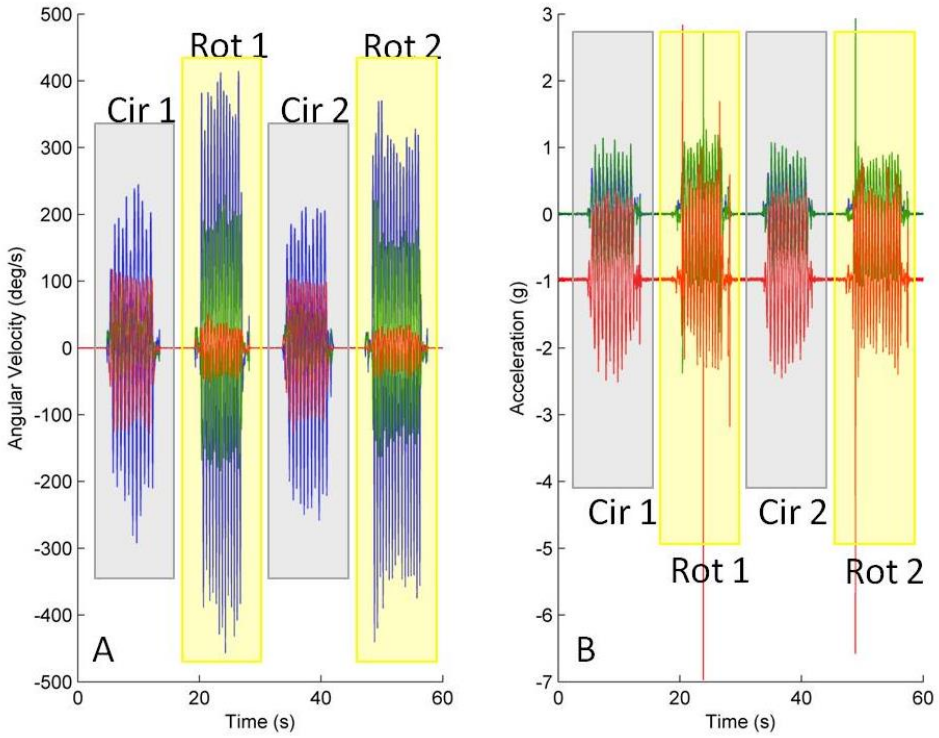

Figure 6.3: Three components of angular velocity (A) and three components of acceleration (B) data for an example 60-second trial. Trial consists of two phases of circumduction motion ("Cir" annotation, gray box) followed by two phases of rotation motion ("Rot" annotation, yellow box). Components of angular velocity and acceleration resolved along the IMU-fixed frame are distinguished by the following colors: x axis = blue, y axis = green, z axis = red

Figure 6.3 illustrates the IMU data from a representative 60-second trial composed of twice-repeated circumduction and rotation phases. The calibrated angular velocity and acceleration appear in Fig. 6.3A and B, respectively. The circumduction motions are highlighted by gray boxes and annotated with "Cir" while the rotation motions are highlighted by yellow boxes and annotated with "Rot". Between these motions, the femur is momentarily at rest; observe phases where the angular velocity remains zero and the acceleration remains -1 g. This data is subsequently used to predict the location of the joint CoR following the methods above.

Method	*x* (mm)	*y* (mm)	*z* (mm)	Vector sum of x, y, z (mm)
CMM	-342.5 (0.4)	288.9 (0.4)	27.9 (0.2)	449.0 (0.3)
IMU	-340.5 (4.4)	290.9 (2.9)	29.1 (1.4)	448.8 (4.8)
Avg. Error (CMM-IMU)	-2.1	-2.0	-1.2	3.1

Table 6.1: Summary of benchmarking experiment, mean (standard deviation) of each component of the joint center position $\vec{r}_{c/a}$ (in mm) for 14 trials of CMM data and 28 trials of IMU data. Third row reports difference in the averages (in mm). Fourth column reports vector sum of the components (in mm).

Table 6.1 summarizes the results from the benchmarking experiment. Reported is the average (standard deviation) for each of the three components of the position vector $\vec{r}_{c/a}$ (the center of the spherical joint relative to the center of the accelerometer in the IMU-fixed reference frame) as independently derived from measurements from the coordinate measuring machine and the IMU. Also reported is the difference between the average components which further yields an overall error of 3.1 mm (vector sum) for the IMU-derived position relative to the CMM-derived position. This overall positional error is comparable to the results of [58] where four video capture methods yield average positional errors between 1 to 6 mm. That study employs a similar mechanical spherical joint with rigid marker attachments.

6.3.2. Simulated Soft-Tissue Effects

In this experiment, the IMU mounts rigidly to a mock femur; whereas in clinical settings, the IMU would mount to soft-tissue which introduces relative movement. During walking, for example, the motion of the soft-tissue relative to the femur induces a mean acceleration on the order of 10 m/s^2 at a frequency of approximately 20 Hz [119].

To explore these soft-tissue effects, we follow an approach similar to [57] where measured position data from the femoral side of a mechanical hip joint is polluted with random displacements within a specified range. Herein, we pollute the IMU-measured acceleration $(\vec{a}_a)$ with random acceleration to model soft tissue motion. In particular, we add to the measured acceleration $(\vec{a}_a)$ a sinusoidal acceleration

$$\vec{a}_s(t) = A\sin(2\pi f \cdot t)\vec{d} \tag{6.7}$$

having random amplitude A, random direction $\vec{d}$, and frequency f. Both A and $\vec{d}$ are assumed constant over one period ($1/f$) before being assigned updated random values. The selected acceleration range $0 \le A \le 11\,\text{m/s}^2$ and the frequency *f=22* Hz replicate those of a skin-mounted accelerometer relative to the femur during walking [119]. Note that the "Rot" and "Cir" motions for this method are smooth and devoid of impact events. By contrast, the random soft tissue acceleration during walking (6.7) is induced by impacts due to heel-strikes. Nevertheless, we test our method using (6.7) as an overestimate of the random accelerations expected in clinical setting due to smooth "Rot" and Cir" motions. The polluted acceleration ($\vec{a}_a + \vec{a}_s$) is used in the method above to re-compute the CoR location using standard least squares as reported in Table 6.2. Figure 6.4 illustrates the magnitude of polluted acceleration during the circumduction and rotation motions (red) which is significantly different than the original smooth acceleration (blue) for the sample trial previously shown including gravity in Fig. 6.3B (11 m/s^2 is over 75% of the maximum acceleration experienced by the accelerometer during this trial).

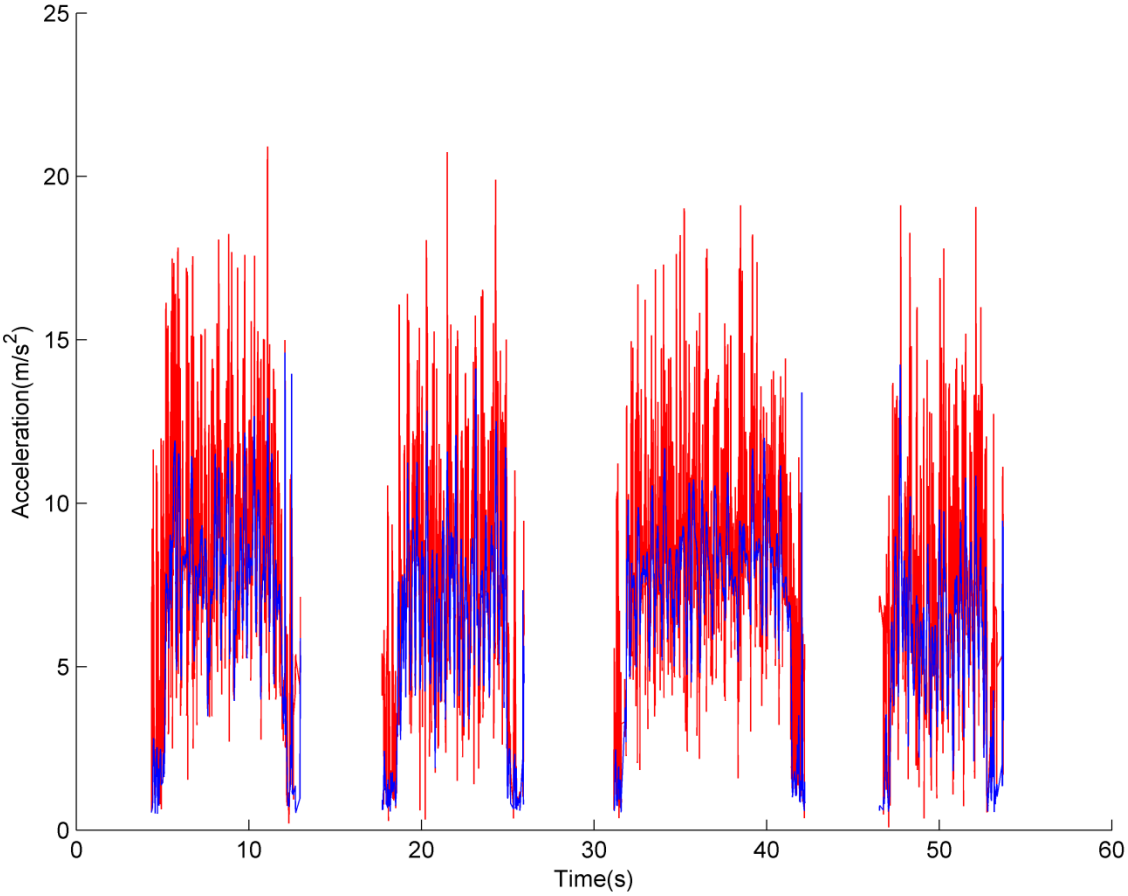

Figure 6.4: The magnitude of the measured acceleration (blue) from Fig. 6.3B once gravity is removed and the magnitude after adding the simulated noise due to soft-tissue motion (red).

Method	*x* (mm)	*y* (mm)	*z* (mm)	Vector Sum of x, y, z (mm)
CMM	-342.5 (0.4)	288.9 (0.4)	27.9 (0.2)	449.0 (0.3)
IMU+P	-340.5 (4.6)	291.2 (3.0)	29.2 (1.4)	448.4 (4.4)
Average Error (CMM-IMU+P)	-2.0	-2.2	-1.3	3.2

Table 6.2: Summary of benchmarking experiment, mean (standard deviation) of each component of the joint center position for 14 trials of CMM data and 28 trials of IMU data in mm. Least-squares estimate employing the fully polluted set of data is denoted method "IMU+P."

Following the format of Table 6.1, Table 6.2 reports the computed average (standard deviation) of the three components of the position vector $\vec{r}_{c/a}$ using the polluted IMU data (Method IMU+P). Note that the position of the CoR determined by the benchmark CMM data differs from that predicted by the fully-polluted IMU data by 3.2 mm. This error represents only a minor 5% increase in the error (3.1 mm) for the ideal rigid joint case. To examine the change in predicted CoR position further, we present in Fig. 6.5 correlation and Bland-Altman plots for the three components of the position vector $\vec{r}_{c/a}$.

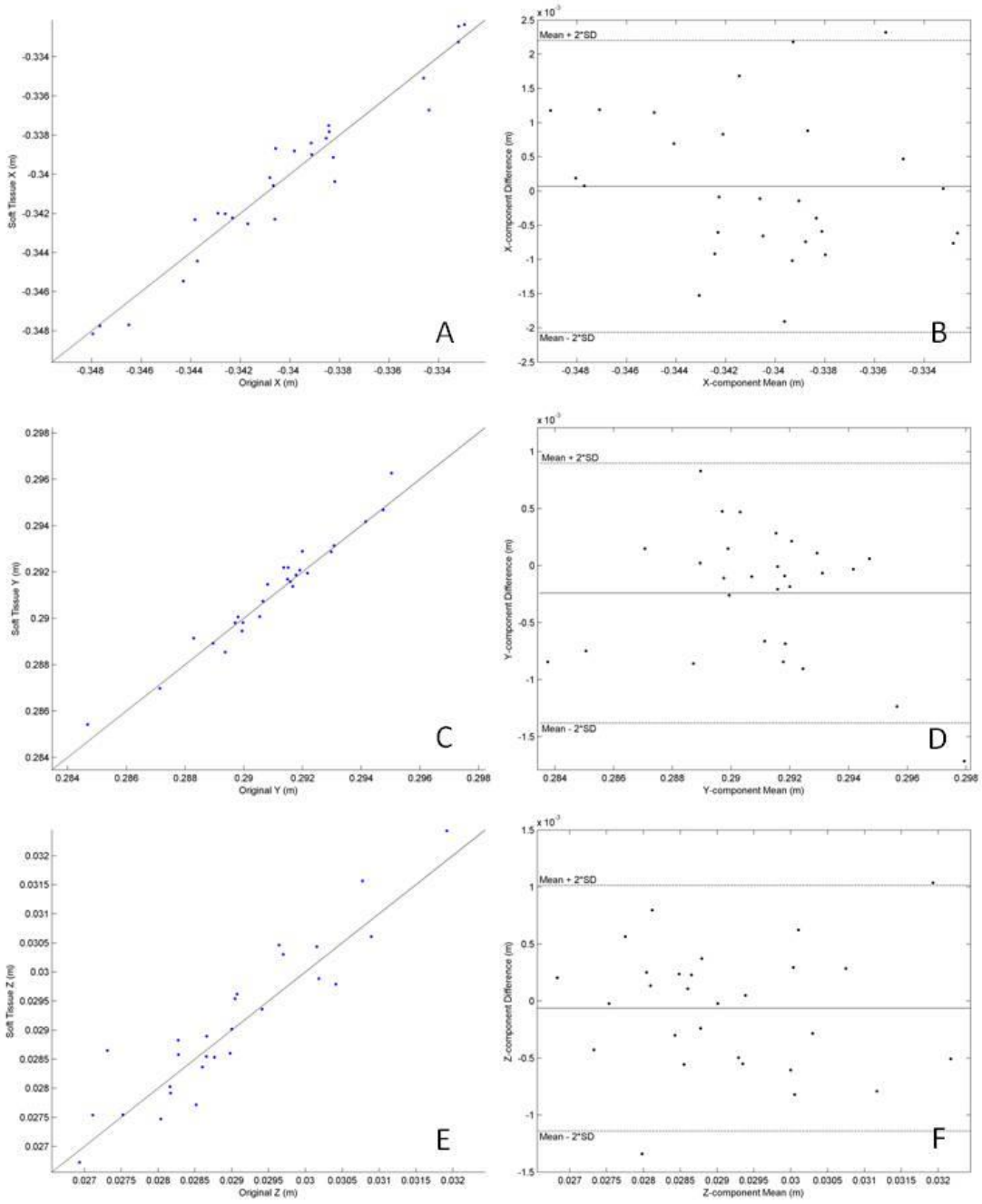

Figure 6.5: The effect of soft-tissue acceleration on the predicted components of the position vector $\vec{r}_{c/a}$. Correlations (A, C, E) plot components predicted from randomly polluted data versus original values for each trial and relative to a line having unit slope. Bland-Altman plots (B, D, F) further illustrate difference in results.

Figure 6.5 illustrates the change in the predicted components of $\vec{r}_{c/a}$ due to the introduction of soft-tissue acceleration. The three components, as predicted from the

polluted acceleration data, are plotted against their original values in Figs. 6.5 A, C, and E, where the superimposed line has unit slope and zero intercept. The Bland-Altman plots for each component in Figs. 6.5 B, D, and F reveal very modest effects of soft-tissue acceleration on the predicted location of the CoR. In particular, the mean (standard deviation) of the difference in the x, y, and z components of $\vec{r}_{c/a}$ due to the polluted acceleration are 0.1 (1.1), -0.2 (0.6), and -0.1 (0.5) mm, respectively suggesting that both the magnitude and direction of this vector are essentially unchanged. The small effect of the random acceleration perturbations can likely be ascribed to the cancellation of the random errors in the least squares solution which considers more than 20,000 samples. By contrast, when random positional noise due to soft-tissue motion was added to data from the video-based method presented in [57], the mean error in hip center location increased by 60% (from 2.2 mm to 3.5 mm) but remained overall quite similar to the values reported here.

Thus, even under exaggerated but simulated soft-tissue effects, the IMU-derived CoR estimates remain accurate relative to those obtained by video-based methods. In particular, the IMU-derived joint CoR remains within a 3mm sphere surrounding the true position measured independently from a precision coordinate measuring machine. Importantly, the IMU-method addresses major shortcomings of video-based methods including their high cost, restricted use to motion capture laboratories, long set-up time (attaching and calibrating reflective markers), and long data reduction time. By contrast, the IMU-method requires a single (and inexpensive) segment-mounted IMU, enables use in clinical, field or laboratory settings, and requires only short duration (30-60 second) testing with rapid reporting of results (5 seconds). These advantages combine to yield a promising non-invasive and accurate tool for estimating joint CoR. These same advantages may further promote advances in total hip and knee arthroplasty as well as new biomechanical tools for the early assessment and prevention of joint injuries.

Chapter 7: Contributions, Conclusions and Future Directions

7.1. Contributions and Conclusions

The use of MEMS inertial sensors (IMUs) in biomechanical and sports training applications has become popular in recent years. This new technology enables direct measurement of each of the three rotational and translational degrees of freedom of a rigid body by providing three-axis sensing of angular velocity and linear acceleration. This wealth of kinematic data, when combined with the low cost and small size of many IMU designs, will fuel the translation of laboratory-based research methods into the clinic and onto the field of play. This dissertation presents five such studies which pioneer the use of IMUs in novel applications in sports training and biomechanics. The major contributions following from each study are summarized below.

The first study, presented in Chapter 2, focuses on an application from sports training, where a miniaturized, ball-embedded IMU is used to quantify the kinematics of baseball and softball pitching. Experimental results demonstrate that the developed computational algorithms deduce the magnitude and direction of the ball's velocity at release to within 4.6% of measurements made using standard MOCAP. In addition, the IMU directly measures the angular velocity of the ball needed to distinguish and analyze different pitch types.

The application to pitcher training is hindered by the limited measurement range of most angular rate gyros. A potential answer to this limitation is presented in Chapter 3, where a method is developed that employs a single, tri-axial accelerometer to reconstruct the angular velocity of a rigid body during free-flight. The measurement theory is presented and validated experimentally. Results confirm that the angular velocity can be reconstructed with exceedingly small errors (less than 2%) when

benchmarked against direct measurements using angular rate gyros. The rotational stability of objects in free flight is also explored experimentally.

The third study (Chapter 4) extends the computational algorithms presented in Chapter 2, contributing a new method for deducing athlete speed non-invasively, on the field of play, using data from a torso-mounted IMU. The method predicts instantaneous athlete speed that correlates well with MOCAP [mean (SD) RMSE = 0.35 m/s (0.20), r = 0.96 (0.05), slope = 0.99 (0.07)] for periods of motion characteristic of explosive sports (e.g. basketball). The method is able to predict the average speed to within an absolute mean (SD) error of 0.03 (0.18) m/s, and RMS error of 0.18 m/s, or 4.3% relative to the average speed by MOCAP. These results compare favorably to existing methods which utilize shank- or foot-mounted IMUs and require subject-specific calibrations. However, the advantage of using a torso-mounted IMU is significant for athlete training and performance since it removes the sensor instrumentation from the lower or upper extremities used for play.

The fourth study departs from applications specific to sports training by exploring the use of an array of IMUs to estimate joint reactions (forces and moments) in multibody systems via inverse dynamic modeling. In particular, this study reports a benchmark experiment on a double-pendulum that reveals the accuracy of IMU-informed estimates of joint reactions compared to those measured by high precision miniature (6-dof) load cells. Results demonstrate that IMU-informed estimates of the three-dimensional reaction forces remain within 5.0% RMS of the load cell measurements and with correlation coefficients greater than 0.95 on average. Similarly, the IMU-informed estimates of the three-dimensional reaction moments remain within 5.9% RMS of the load cell measurements and with correlation coefficients greater than 0.88 on average. The sensitivity of these estimates to mass center location is also discussed.

An important step in the IMU-informed inverse dynamic modeling presented in Chapter 5 is determining the location of the body-fixed IMUs relative to the joints of the multibody system. The final study includes the development and validation of an algorithm for deducing the location of the center of rotation (CoR) of a spherical joint relative to a body-fixed IMU. Results demonstrate that this new method resolves the position of the CoR to within a 3 mm sphere of the true CoR determined by a precision

coordinate measuring machine. Such accuracy may render this method attractive for broad use in field, laboratory and clinical settings requiring non-invasive and rapid estimates of joint CoR.

7.2. Limitations and Future Directions

As summarized above, this dissertation contributes novel methods for advancing the use of IMUs for applications in sports training and human biomechanics. Doing so enables the analysis of human motion outside of the motion capture laboratory. However, since the studies herein all focus on benchmarking the accuracy of new algorithms, a limitation is that all data was necessarily collected in a laboratory environment. Therefore, an obvious future direction for this work is the successful translation of the new algorithms to studies outside the laboratory and in the clinic or on the field of play. Specific limitations and possible future directions for each study are reported below.

The major limitations of the baseball and softball pitching study presented in Chapter 2 are two-fold. First, only two pitchers, one baseball and one softball, are considered in the analysis. While this was sufficient to develop the algorithm for computing ball linear and angular velocity, a study with a large group of subjects and with considerable input from pitching coaches is recommended to fully map out the potential of this technology for pitcher training, skill assessment, injury prevention and rehabilitation. Second, as mentioned in Chapters 2 and 3, there was a technological limitation in the IMU hardware. Both baseballs and softballs are pitched with angular rates that far exceed the measurement range of the angular rate gyros used in the study. To avoid this limitation, we instructed pitchers to throw sub-maximal versions of their pitches. However, the algorithms presented will still succeed for maximal pitching motions provided at least one of two changes are made: (1) revise the IMU hardware to Z recently developed high range rate gyros (i.e., Analog Devices ™ now offers single axis gyros with a range of 20,000 deg/s), or (2) implement an extension to the algorithm in Chapter 3 for reconstructing angular velocity from accelerometer data by also modeling the aerodynamic forces acting on the ball.

The primary limitation of the study investigating athlete speed (Chapter 4) is that only a single subject was considered for the benchmarking experiment. The measurements were also constrained to a 25 m^2 area which limited the speed and duration of the motions considered. While the data collected demonstrate the potential accuracy of the speed estimation algorithm, further benchmarking using data recorded during actual competition and in larger capture volumes would reinforce confidence in the algorithm. Following this second benchmarking experiment, the algorithm could readily support athlete training, assessment, and rehabilitation in environments previously impossible due to limitations imposed by GPS and MOCAP.

The IMU-based estimates of joint reactions in Chapter 5 were ultimately limited by the pendulum hardware and the measurement range of the miniaturized load cells. The instrumentation added to the pendulum made it challenging to identify the mass center which became the limiting factor affecting the accuracy of estimated reactions. The generated reaction forces and torques were also an order of magnitude smaller than those characteristic of human motion due to the range limitations imposed by the load cells. Despite these limitations, the results from this benchmarking study yielded excellent agreement between the IMU-estimated and the load cell-measured reactions. One potential future study could replicate this benchmarking experiment for MOCAP-enabled inverse dynamic estimated reactions providing a direct comparison between the accuracy of IMU and MOCAP enabled inverse dynamics. Following this second benchmark, this study supports the promising and broad use of IMU technology for estimating joint reactions in human motion applications.

Finally, the algorithm for deducing the center of rotation of spherical joints (Chapter 6) is limited by the use of a mechanical model to the human hip joint. This is a logical starting point since the center of rotation of the mechanical model is well characterized through measurements from a coordinate measuring machine. The effects of soft tissue motion however are only approximated through simulated random soft tissue acceleration superimposed on the measured acceleration. As the next step, we recommend a follow-up study on human hip joints that incorporates the challenges of soft tissue motion and, possibly, joint translation/laxity. In particular, we recommend a second benchmarking study where the CoR of cadaveric hips are accurately established

through imaging and compared to the IMU-predicted locations with IMU's affixed to soft tissue and also directly to bone. Doing so will isolate the influence of soft tissue motion and ultimately define the accuracy of the algorithm. Additionally, the algorithm developed for spherical joints should be extended to identify the axis of rotation for hinge joints. Downstream of these studies, this algorithm may find broad use in both clinical and laboratory settings for any application requiring quick, non-invasive and accurate identification of joint CoR.

References

[1] Feltner M., and Dapena J., 1986, "Dynamics of the shoulder and elbow joints of the throwing arm during a baseball pitch," International Journal of Sport Biomechanics, **2**(4), pp. 235–259.

[2] Loosli A. R., Requa R. K., Garrick J. G., and Hanley E., 1992, "Injuries to pitchers in women's collegiate fast-pitch softball," The American Journal of Sports Medicine, **20**(1), pp. 35 –37.

[3] Davy D. T., and Audu M. L., 1987, "A dynamic optimization technique for predicting muscle forces in the swing phase of gait," Journal of Biomechanics, **20**(2), pp. 187–201.

[4] Jonsson H., and Kärrholm J., 1994, "Three-dimensional knee joint movements during a step-up: Evaluation after anterior cruciate ligament rupture," Journal of Orthopaedic Research, **12**(6), pp. 769–779.

[5] Aminian K., and Najafi B., 2004, "Capturing human motion using body-fixed sensors: outdoor measurement and clinical applications," Computer Animation and Virtual Worlds, **15**(2), pp. 79–94.

[6] Simon S. R., 2004, "Quantification of human motion: gait analysis—benefits and limitations to its application to clinical problems," Journal of Biomechanics, **37**(12), pp. 1869–1880.

[7] Whitely R., 2007, "Baseball throwing mechanics as they relate to pathology and performance – A review," Journal of Sports Science and Medicine, (6), pp. 1–20.

[8] Manal K., McClay I., Stanhope S., Richards J., and Galinat B., 2000, "Comparison of surface mounted markers and attachment methods in estimating tibial rotations during walking: an in vivo study," Gait & Posture, **11**(1), pp. 38–45.

[9] Fleisig G., Escamilla R., Andrews J., Matsuo T., Satterwhite Y., and Barrentine S., 1996, "Kinematic and kinetic comparison between baseball pitching and football passing," J. Appl. Biomech., **12**(2), pp. 207–224.

[10] Barrentine S. W., Fleisig G. S., Whiteside J. A., Escamilla R. F., and Andrews J. R., 1998, "Biomechanics of windmill softball pitching with implications about injury mechanisms at the shoulder and elbow," J Orthop Sports Phys Ther, **28**(6), pp. 405–415.

[11] Langenderfer J. E., Laz P. J., Petrella A. J., and Rullkoetter P. J., 2008, "An efficient probabilistic methodology for incorporating uncertainty in body segment parameters and anatomical landmarks in joint loadings estimated from inverse dynamics," J Biomech Eng, **130**(1), p. 014502.

[12] Mündermann L., Corazza S., and Andriacchi T. P., 2006, "The evolution of methods for the capture of human movement leading to markerless motion capture for biomechanical applications," Journal of NeuroEngineering and Rehabilitation, **3**(1), p. 6.

[13] Winter D. A., 1990, Biomechanics and motor control of human movement, Wiley, New York.

[14] Riemer R., Hsiao-Wecksler E. T., and Zhang X., 2008, "Uncertainties in inverse dynamics solutions: A comprehensive analysis and an application to gait," Gait & Posture, **27**(4), pp. 578–588.

[15] Santos J. M., Gold G. E., Besier T. F., Hargreaves B. A., Draper C. E., Beaupre G. S., Delp S. L., and Pauly J. M., 2005, "Full-Flexion Patellofemoral Joint Kinematics with Real-Time MRI at 0.5T," Proc. Intl. Soc. Mag. Reson. Med., **13**, p. 1951.
[16] Thomas P., 1996, "A marker-free method for tracking human lower limb segments based on model matching," International Journal of Bio-Medical Computing, **41**(2), pp. 87–97.
[17] Corazza S., Mündermann L., Chaudhari A. M., Demattio T., Cobelli C., and Andriacchi T. P., 2006, "A Markerless Motion Capture System to Study Musculoskeletal Biomechanics: Visual Hull and Simulated Annealing Approach," Annals of Biomedical Engineering, **34**, pp. 1019–1029.
[18] Sheets A. L., Abrams G. D., Corazza S., Safran M. R., and Andriacchi T. P., 2011, "Kinematics Differences Between the Flat, Kick, and Slice Serves Measured Using a Markerless Motion Capture Method," Ann Biomed Eng, **39**(12), pp. 3011–3020.
[19] Jovanov E., Milenkovic A., Otto C., and Groen P. C. de, 2005, "A wireless body area network of intelligent motion sensors for computer assisted physical rehabilitation," Journal of NeuroEngineering and Rehabilitation, **2**(1), p. 6.
[20] Wong W. Y., Wong M. S., and Lo K. H., 2007, "Clinical Applications of Sensors for Human Posture and Movement Analysis: A Review," Prosthet Orthot Int, **31**(1), pp. 62–75.
[21] Alaways L., and Hubbard M., 2001, "Experimental determination of baseball spin and lift," J. Sports Sci., **19**(5), pp. 349–358.
[22] Alaways L., Mish S., and Hubbard M., 2001, "Identification of release conditions and aerodynamic forces in pitched-baseball trajectories," J. Appl. Biomech., **17**(1), pp. 63–76.
[23] Bahill A. T., and Baldwin D. G., 2007, "Describing baseball pitch movement with right-hand rules," Computers in Biology and Medicine, **37**(7), pp. 1001–1008.
[24] Theobalt C., Albrecht I., Haber J., Magnor M., and Seidel H.-P., 2004, "Pitching a baseball: tracking high-speed motion with multi-exposure images," ACM Trans. Graph., **23**(3), pp. 540–547.
[25] Fleisig G., Barrentine S., Zheng N., Escamilla R., and Andrews J., 1999, "Kinematic and kinetic comparison of baseball pitching among various levels of development," J. Biomech., **32**(12), pp. 1371–1375.
[26] Fleisig G. S., and Escamilla R. F., 1996, "Biomechanics of the elbow in the throwing athlete," Operative Techniques in Sports Medicine, **4**(2), pp. 62–68.
[27] Lapinski M., Berkson E., Gill T., Reinold M., and Paradiso J. A., 2009, "A Distributed Wearable, Wireless Sensor System for Evaluating Professional Baseball Pitchers and Batters," 2009 International Symposium on Wearable Computers, Proceedings, IEEE Computer Soc, Los Alamitos, pp. 131–138.
[28] Koda H., Sagawa K., Kuroshima K., Tsukamoto T., Urita K., and Ishibashi Y., 2010, "3D Measurement of Forearm and Upper Arm during Throwing Motion using Body Mounted Sensor," J. Adv. Mech. Des. Syst. Manuf., **4**(1), pp. 167–178.
[29] Routh E. J., 1882, A treatise on the dynamics of a system of rigid bodies. With numerous examples., Macmillan, London.
[30] Gray A., 1918, A treatise on gyrostatics and rotational motion. Theory and applications., Macmillan and co., limited, London.

[31] Goldstein H., 1980, Classical mechanics, Addison-Wesley Pub. Co., Reading, Mass.
[32] Chen J.-H., Lee S.-C., and Debra D. B., 1994, "Gyroscope free strapdown inertial measurement unit by six linear accelerometers," Journal of Guidance Control Dynamics, **17**, pp. 286–290.
[33] Hanson R., and Pachter M., 2005, "Optimal Gyro-Free IMU Geometry," 2005 AIAA Guidance, Navigation, and Control Conference and Exhibit, San Francisco, CA, pp. 1–8.
[34] Kranz M., Möller A., Hammerla N., Diewald S., Plötz T., Olivier P., and Roalter L., "The mobile fitness coach: Towards individualized skill assessment using personalized mobile devices," Pervasive and Mobile Computing.
[35] Coutts A. J., and Duffield R., 2010, "Validity and reliability of GPS devices for measuring movement demands of team sports," Journal of Science and Medicine in Sport, **13**(1), pp. 133–135.
[36] Varley M. C., Fairweather I. H., and Aughey R. J., 2012, "Validity and reliability of GPS for measuring instantaneous velocity during acceleration, deceleration, and constant motion," J Sports Sci, **30**(2), pp. 121–127.
[37] Waegli A., and Skaloud J., 2009, "Optimization of two GPS/MEMS-IMU integration strategies with application to sports," GPS Solutions, **13**(4), pp. 315–326.
[38] "adidas miCoach: The Interactive Personal Coaching and Training System" [Online]. Available: http://www.adidas.com/us/micoach/. [Accessed: 30-Jan-2013].
[39] Hausswirth C., Le Meur Y., Couturier A., Bernard T., and Brisswalter J., 2009, "Accuracy and Repeatability of the Polar ® RS800sd to Evaluate Stride Rate and Running Speed," International Journal of Sports Medicine, **30**(05), pp. 354–359.
[40] "Product « Catapult Sports" [Online]. Available: http://catapultsports.com/us/product/. [Accessed: 28-Feb-2013].
[41] Aughey R. J., and Falloon C., 2010, "Real-time versus post-game GPS data in team sports," Journal of Science and Medicine in Sport, **13**(3), pp. 348–349.
[42] Montgomery P. G., Pyne D. B., and Minahan C. L., 2010, "The physical and physiological demands of basketball training and competition," Int J Sports Physiol Perform, **5**(1), pp. 75–86.
[43] Neville J., Wixted A., Rowlands D., and James D., 2010, "Accelerometers: An underutilized resource in sports monitoring," 2010 Sixth International Conference on Intelligent Sensors, Sensor Networks and Information Processing (ISSNIP), pp. 287 –290.
[44] Song Y., Shin S., Kim S., Lee D., and Lee K. H., 2007, "Speed estimation from a tri-axial accelerometer using neural networks," Conf Proc IEEE Eng Med Biol Soc, **2007**, pp. 3224–3227.
[45] Herren R., Sparti A., Aminian K., and Schutz Y., 1999, "The prediction of speed and incline in outdoor running in humans using accelerometry," Med Sci Sports Exerc, **31**(7), pp. 1053–1059.
[46] Wixted A. J., Thiel D. V., Hahn A. G., Gore C. J., Pyne D. B., and James D. A., 2007, "Measurement of Energy Expenditure in Elite Athletes Using MEMS-Based Triaxial Accelerometers," IEEE Sensors Journal, **7**(4), pp. 481 –488.

[47] Yang S., Mohr C., and Li Q., 2011, "Ambulatory running speed estimation using an inertial sensor," Gait & Posture, **34**(4), pp. 462–466.
[48] Yuan Q., and Chen I.-M., 2011, "Simultaneous Localization and Capture with velocity information," 2011 IEEE/RSJ International Conference on Intelligent Robots and Systems (IROS), pp. 2935 –2940.
[49] Kurtz S., Ong K., Lau E., Mowat F., and Halpern M., 2007, "Projections of primary and revision hip and knee arthroplasty in the United States from 2005 to 2030," JBJS, **89**(4), pp. 780–785.
[50] Kinzl L., Gebhard F., and Keppler P., 2004, "Total knee arthroplasty--navigation as the standard," Chirurg, **75**(10), pp. 976–981.
[51] Wixson R. L., and MacDonald M. A., 2005, "Total hip arthroplasty through a minimal posterior approach using imageless computer-assisted hip navigation," The Journal of Arthroplasty, **20, Supplement 3**, pp. 51–56.
[52] Hoste D., and Victor J., 2004, "Image-based computer-assisted total knee arthroplasty leads to lower variability in coronal alignment," Clinical orthopaedics and related research, **428**(428), pp. 131–139.
[53] DiGioia III A. M., Plakseychuk A. Y., Levison T. J., and Jaramaz B., 2003, "Mini-incision technique for total hip arthroplasty with navigation," The Journal of Arthroplasty, **18**(2), pp. 123–128.
[54] Halvorsen K., Lesser M., and Lundberg A., 1999, "A new method for estimating the axis of rotation and the center of rotation," Journal of Biomechanics, **32**(11), pp. 1221–1227.
[55] Gamage S. S. H. U., and Lasenby J., 2002, "New least squares solutions for estimating the average centre of rotation and the axis of rotation," Journal of Biomechanics, **35**(1), pp. 87–93.
[56] Schwartz M. H., and Rozumalski A., 2005, "A new method for estimating joint parameters from motion data," Journal of Biomechanics, **38**(1), pp. 107–116.
[57] Siston R. A., and Delp S. L., 2006, "Evaluation of a new algorithm to determine the hip joint center," Journal of Biomechanics, **39**(1), pp. 125–130.
[58] MacWilliams B. A., 2008, "A comparison of four functional methods to determine centers and axes of rotations," Gait & Posture, **28**(4), pp. 673–679.
[59] Ehrig R. M., Heller M. O., Kratzenstein S., Duda G. N., Trepczynski A., and Taylor W. R., 2011, "The SCoRE residual: A quality index to assess the accuracy of joint estimations," Journal of Biomechanics, **44**(7), pp. 1400–1404.
[60] Van der Walt N., 2012, "Systems and methods for joint replacement."
[61] Savage P., 2000, Strapdown analytics, Strapdown Associates, Maple Plain, MN.
[62] Nathan A. M., 2008, "The effect of spin on the flight of a baseball," Am. J. Phys., **76**(2), pp. 119–124.
[63] Theobalt C., Albrecht I., Haber J., Magnor M., and Seidel H.-P., 2004, "Pitching a baseball: tracking high-speed motion with multi-exposure images," ACM SIGGRAPH 2004 Papers, ACM, New York, NY, USA, pp. 540–547.
[64] Werner S. L., Jones D. G., Guido J. A., and Brunet M. E., 2006, "Kinematics and Kinetics of Elite Windmill Softball Pitching," The American Journal of Sports Medicine, **34**(4), pp. 597 –603.

[65] Werner S. L., Guido J. A., McNeice R. P., Richardson J. L., Delude N. A., and Stewart G. W., 2005, "Biomechanics of Youth Windmill Softball Pitching," The American Journal of Sports Medicine, **33**(4), pp. 552 –560.
[66] King K., Perkins N. C., Churchill H., McGinnis R., Doss R., and Hickland R., 2010, "Bowling ball dynamics revealed by miniature wireless MEMS inertial measurement unit," Sports Engineering, **13**(2), pp. 95–104.
[67] King K., Hough J., McGinnis R., and Perkins N., 2012, "A new technology for resolving the dynamics of a swinging bat," Sports Engineering, **15**(1), pp. 41–52.
[68] King K. W., 2008, "The design and application of wireless MEMS inertial measurement units for the measurement and analysis of golf swings," PhD, University of Michigan.
[69] King K., Yoon S. W., Perkins N. C., and Najafi K., 2008, "Wireless MEMS inertial sensor system for golf swing dynamics," Sensors and Actuators A: Physical, **141**(2), pp. 619–630.
[70] McGinnis R. S., Perkins N. C., and King K., 2012, "Pitcher training aided by instrumented baseball," Procedia Engineering, Lowell, MA, pp. 580–585.
[71] McGinnis R. S., Perkins N. C., and King K., 2012, "Reconstructing free-flight angular velocity from miniaturized wireless accelerometer," J. Appl. Mech., **1**(1), p. 274.
[72] Tom Verducci, 2011, "How a Danish tech company is revolutionizing pitching data," SI.com.
[73] Greenwood D. T., 1965, Principles of dynamics, Prentice-Hall, Englewood Cliffs, N.J.
[74] Simo J. C., Tarnow N., and Doblare M., 1995, "Non-linear dynamics of three-dimensional rods: Exact energy and momentum conserving algorithms," International Journal for Numerical Methods in Engineering, **38**(9), pp. 1431–1473.
[75] Titterton D. H., and Weston J. L., 2004, Strapdown inertial navigation technology, Institution of Electrical Engineers, Stevenage, UK.
[76] Wie B., 1998, Space vehicle dynamics and control, American Institute of Aeronautics and Astronautics, Reston, VA.
[77] Mettler B. F., 2010, "Extracting micro air vehicles aerodynamic forces and coefficients in free flight using visual motion tracking techniques," Exp. Fluids, **49**(3), pp. 557–569.
[78] Aghili F., and Parsa K., 2009, "Motion and Parameter Estimation of Space Objects Using Laser-Vision Data," J. Guid. Control Dyn., **32**(2), pp. 538–550.
[79] Lichter M., and Dubowsky S., 2004, "State, shape, and parameter estimation of space objects from range images," 2004 Ieee International Conference on Robotics and Automation, Vols 1- 5, Proceedings, Ieee, New York, pp. 2974–2979.
[80] Hillenbrand U., and Lampariello R., 2005, "Motion and Parameter Estimation of a Free-Floating Space Object from Range Data for Motion Prediction."
[81] Kim S.-G., Crassidis J. L., Cheng Y., Fosbury A. M., and Junkins J. L., 2007, "Kalman filtering for relative spacecraft attitude and position estimation," J. Guid. Control Dyn., **30**(1), pp. 133–143.
[82] Thienel J. K., and Sanner R. M., 2007, "Hubble Space Telescope angular velocity estimation during the robotic servicing mission," J. Guid. Control Dyn., **30**(1), pp. 29–34.

[83] Bhat K., Seitz S., Popovic J., and Khosla P., 2002, "Computing the physical parameters of rigid-body motion from video," Computer Vison - Eccv 2002, Pt 1, A. Heyden, G. Sparr, M. Nielsen, and P. Johansen, eds., Springer-Verlag Berlin, Berlin, pp. 551–565.
[84] Masutani Y., Iwatsu T., and Miyazaki F., 1994, "Motion estimation of unknown rigid body under no external forces and moments," 1994 IEEE International Conference on Robotics and Automation, pp. 1066–1072.
[85] Lorenz R., 2005, "Flight and attitude dynamics measurements of an instrumented Frisbee," Meas. Sci. Technol., **16**(3), pp. 738–748.
[86] Zappa B., Legnani G., Van den Bogert A. J., and Adamini R., 2001, "On the Number and Placement of Accelerometers for Angular Velocity and Acceleration Determination," J. Dyn. Sys., Meas., Control, **123**(3), pp. 552–554.
[87] Cardou P., and Angeles J., 2008, "Angular velocity estimation from the angular acceleration matrix Philippe Cardou and Jorge Angeles," J. Appl. Mech.-Trans. ASME, **75**(2).
[88] Mital N. K., and King A. I., 1979, "Computation of Rigid-Body Rotation in Three-Dimensional Space From Body-Fixed Linear Acceleration Measurements," J. Appl. Mech., **46**(4), pp. 925–930.
[89] Genin J., Hong J., and Xu W., 1997, "Accelerometer Placement for Angular Velocity Determination," J. Dyn. Sys., Meas., Control, **119**(3), pp. 474–477.
[90] King K. W., and Perkins N. C., 2008, "Putting Stroke Analysis Using MEMS Inertial Sensor Systems," Phoenix, AZ, pp. 270–278.
[91] King K. W., Yoon S. W., Perkins N. C., and Najafi K., "The Dynamics of the Golf Swing as Measured by Strapdown Inertial Sensors," Proceedings 5th International Conference on the Engineering of Sport, Davis, CA, pp. 276–282.
[92] Perkins N. C., 2006, "Electronic measurement of the motion of a moving body of sports equipment."
[93] Kane T. R., Likins P. W., and Levinson D. A., 1983, Spacecraft dynamics, McGraw-Hill Book Co., New York.
[94] Van Zon R., and Schofield J., 2007, "Numerical implementation of the exact dynamics of free rigid bodies," Journal of Computational Physics, **225**(1), pp. 145–164.
[95] Williams T., Pahadia A., Petovello M., and Lachapelle G., 2009, "Using an Accelerometer Configuration to Improve the Performance of a MEMS IMU: Feasibility Study with a Pedestrian Navigation Application," Savannah, GA.
[96] Ciblak N., 2007, "Determining the Angular Motion of a Rigid Body Using Linear Accelerometers Without Integration," 3rd International Conference on Recent Advances in Space Technologies, 2007. RAST '07, IEEE, pp. 585–590.
[97] Moré J. J., and Sorensen D. C., 1983, "Computing a Trust Region Step," SIAM Journal on Scientific and Statistical Computing, **4**, p. 553.
[98] Grip N., and Sabourova N., 2011, "Simple non-iterative calibration for triaxial accelerometers," Measurement Science and Technology, **22**(12), p. 125103.
[99] Pham Q.-C., Hicheur H., Arechavaleta G., Laumond J.-P., and Berthoz A., 2007, "The formation of trajectories during goal-oriented locomotion in humans. II. A maximum smoothness model," European Journal of Neuroscience, **26**(8), pp. 2391–2403.

[100] Ben Abdelkrim N., El Fazaa S., and El Ati J., 2007, "Time-motion analysis and physiological data of elite under-19-year-old basketball players during competition," Br J Sports Med, **41**(2), pp. 69–75; discussion 75.
[101] Van den Noort J. C., Van der Esch M., Steultjens M. P. M., Dekker J., Schepers H. M., Veltink P. H., and Harlaar J., 2012, "The knee adduction moment measured with an instrumented force shoe in patients with knee osteoarthritis," Journal of Biomechanics, **45**(2), pp. 281–288.
[102] Krüger A., McAlpine P., Borrani F., and Edelmann-Nusser J., 2012, "Determination of three-dimensional joint loading within the lower extremities in snowboarding," Proc Inst Mech Eng H, **226**(2), pp. 170–175.
[103] Rouhani H., Favre J., Crevoisier X., and Aminian K., 2011, "Ambulatory measurement of ankle kinetics for clinical applications," J Biomech, **44**(15), pp. 2712–2718.
[104] Faber G. S., Kingma I., and Van Dieën J. H., 2010, "Bottom-up estimation of joint moments during manual lifting using orientation sensors instead of position sensors," J Biomech, **43**(7), pp. 1432–1436.
[105] Hough J., McGinnis R. S., and Perkins N. C., "Benchmark of IMU derived kinetic energy via double pendulum," Journal of Applied Mechanics, **Submitted**.
[106] Dillon M. P., Barker T. M., and Pettet G., 2008, "Effect of inaccuracies in anthropometric data and linked-segment inverse dynamic modeling on kinetics of gait in persons with partial foot amputation," Journal of Rehabilitation Research and Development, **45**(9), pp. 1303–16.
[107] McGinnis R. S., and Perkins N. C., "Inertial Sensor Based Method for Identifying Ball Joint Center of Rotation," Journal of Biomechanics, **Submitted**.
[108] Reinbolt J. A., Haftka R. T., Chmielewski T. L., and Fregly B. J., 2007, "Are patient-specific joint and inertial parameters necessary for accurate inverse dynamics analyses of gait?," IEEE Trans Biomed Eng, **54**(5), pp. 782–793.
[109] Holden J. P., and Stanhope S. J., 1998, "The effect of variation in knee center location estimates on net knee joint moments," Gait & Posture, **7**(1), pp. 1–6.
[110] Rao G., Amarantini D., Berton E., and Favier D., 2006, "Influence of body segments' parameters estimation models on inverse dynamics solutions during gait," Journal of Biomechanics, **39**(8), pp. 1531–1536.
[111] Cole G., Nigg B., Van den Bogert A., and Gerritsen K., 1996, "Lower extremity joint loading during impact in running," Clinical Biomechanics, **11**(4), pp. 181–193.
[112] Pain M. T. G., and Challis J. H., 2006, "The influence of soft tissue movement on ground reaction forces, joint torques and joint reaction forces in drop landings," Journal of Biomechanics, **39**(1), pp. 119–124.
[113] Wixson R. L., 2008, "Computer-assisted total hip navigation," Instr Course Lect, **57**, pp. 707–720.
[114] Stagni R., Leardini A., Cappozzo A., Grazia Benedetti M., and Cappello A., 2000, "Effects of hip joint centre mislocation on gait analysis results," Journal of Biomechanics, **33**(11), pp. 1479–1487.
[115] Wu G., Siegler S., Allard P., Kirtley C., Leardini A., Rosenbaum D., Whittle M., D'Lima D. D., Cristofolini L., Witte H., Schmid O., and Stokes I., 2002, "ISB recommendation on definitions of joint coordinate system of various joints for the

reporting of human joint motion—part I: ankle, hip, and spine," Journal of Biomechanics, **35**(4), pp. 543–548.

[116] McLean S. G., Huang X., and Van den Bogert A. J., 2005, "Association between lower extremity posture at contact and peak knee valgus moment during sidestepping: Implications for ACL injury," Clinical Biomechanics, **20**(8), pp. 863–870.

[117] Sangeux M., Peters A., and Baker R., 2011, "Hip joint centre localization: Evaluation on normal subjects in the context of gait analysis," Gait & Posture, **34**(3), pp. 324–328.

[118] McGinnis R. S., and Perkins N. C., 2012, "A highly miniaturized, wireless inertial measurement unit for characterizing the dynamics of pitched baseballs and softballs," Sensors, **12**(9), pp. 11933–11945.

[119] Wakeling J. M., and Nigg B. M., 2001, "Modification of soft tissue vibrations in the leg by muscular activity," J Appl Physiol, **90**(2), pp. 412–420.